ACIT5930

MASTERS'S THESIS

in

Applied Computer and Information Technology (ACIT)

Robotics & Control

Topics in Guidance, Navigation & Control of Underwater Gliders

Ivar Bjørgo Saksvik

Department of Mechanical, Electrical & Chemical Engineering, Faculty of Technology, Art & Design

OSLOMET

Preface

This thesis was written during the spring of 2022 as the final contribution of Master of Science in applied computer and information technology (ACIT) with specialization in robotics and control. It is also a contribution to the MarTERA founded OASYS (Ocean-Air synoptic operations using coordinated autonomous robotic SYStems and micro underwater gliders) project at Oslo Metropolitan University.

Abstract

This thesis is concerned with the topics in modeling, guidance, navigation and control of underwater gliders, related to a special class of autonomous underwater vehicles (AUVs). Gliders main source of locomotion is a buoyancy engine which allows the vehicle to perform repeating upward and downward glides in the water column. To control the attitude and heading, internal moving mass actuators are exploited. A mathematical model of the fixed-wing underwater glider is derived, including rigid-body dynamics, hydrodynamics, and hydrostatic forces. The glider model is implemented in a numerical framework to simulate generic glider motions and to validate guidance, navigation and control systems.

PID feedback control laws are proposed for heading and pitch control of the simulated buoyancy propelled glider. The control laws are further cascaded with a guidance and navigation system in a feedback loop. Navigation is considered a notorious challenge in underwater gliders due to limitations of navigational instruments. In practice, inertial measurement units (IMUs) and depth sensors are commonly used sensors for dead-reckoning (DR) navigation. Considering a limited sensor suite, we investigate how deep learning (DL) models e.g. artificial neural networks can be exploited to aid DR navigation. The proposed networks predict the planar velocities of the vehicle, which are further used to approximate the planar displacement trough time integration.

The second part of the thesis investigate path-following/guidance laws for under-actuated underwater gliders. Line-of-sight (LOS) guidance laws are presented for the straight-line path-following control problem. Various simulations are carried out to evaluate the performance when affected by different ocean current disturbances using the numerical glider model.

In addition to the latter topics, we propose a target tracking scheme of underwater gliders using unmanned surface vehicles (USVs) for the purpose of target localization. A target tracking guidance law is implemented in a topside USV to pursue generic motions of the submerged glider from the surface. The target-tracking scheme was validated in a simulation environment of the two vehicles.

Acknowledgements

I would like to thank my supervisor Alex Alcocer and my co-supervisor Vahid Hassani for all the help and motivation throughout this master project. I would also like to thank Antonio Pascoal for valuable discussions and feedback.

Ivar Bjørgo Saksvik
May 16, 2022

To my father, may you rest easy on the wings of eternity

Contents

List of Tables

List of Figures

Chapter 1

Introduction

1.1 Underwater Gliders

Underwater gliders are a special class of autonomous underwater vehicles (AUVs) driven by buoyancy propulsion. By adjusting it's net buoyancy, the vehicle is able to *glide* up and down in the water column without conventional power-consuming thrusters. Commercial *legacy gliders* such as Slocum and Seaglider are operational for months and are able to travel 1500-2500 km before the onboard batteries need to recharge. The longevity of these vehicles has made them useful tools in physical oceanography, usually equipped with scientific payloads, e.g. CTD (conductivity, temperature, depth) sensors, chlorophyll instruments, and/or dissolved oxygen sensors. The merit of gliders in oceanography has been demonstrated in various expeditions such as long-term hurricane monitoring [4,23,72], Atlantic-ocean crossing [40] and *under-the-ice* surveys [71,75,101]. However, the commercially available gliders are often costly and large in size and weight. The average length and weight are approximately 2 meters and 50 kg, which makes it challenging to deploy and recover gliders without having an assisting surface vessel, resulting in large operational costs. Hence, there is an unmet demand for affordable and smaller underwater gliders.

1.1.1 The OASYS Project

The OASYS (Ocean-Air synoptic operations using coordinated autonomous robotic SYStems and micro underwater gliders) project aims to demonstrate an ocean-air coordinated operation using miniature underwater gliders and unmanned aerial vehicles (UAV). The deployment and recovery of the miniature underwater gliders are autonomously made by the UAVs with the purpose of reducing operational costs and removing human intervention in hazardous environments.

The OASYS glider, illustrated in figure 1.1, is a low-cost miniaturized glider with a net weight of 10 kg. Its cost, including a scientific payload, is approximately 1/10 the price of a commercial glider.

Glider	*Weight*	*Length*	*Diameter*	*Price*
OASYS [92]	10 Kg	1.4 m	0.08 m	7.5K-10K $
Seaglider [31]	50 kg	2 m	0.2 m	100K-200K $
Slocum [41]	50 kg	1.5 m	0.2 m	100K-200K $
Oceanscout [78]	25 kg	1.5 m	0.10 m	$<$ 50K $

Table 1.1: Comparing Underwater Gliders

Figure 1.1: OASYS underwater glider, courtesey of Oslomet

The OASYS glider travels from place to place by performing a series of upward and downward flights. A novel *variable buoyancy system (VBS)* displaces the net volume of the vehicle [28,92] allowing it to sink and rise in the water column. The VBS system consists of an external bladder and an internal oil reservoir, where the oil is pumped

between the two receptacles using a miniaturized pump [28]. It's nominal cruising speed is approximately 0.1-0.3 m/s depending on the pitching angle of the vehicle. Due to the slow speeds, causing low hydrodynamic pressure, internal moving mass actuators are exploited to control the pitch and heading angles of the vehicle, instead of conventional control surfaces such as rudders and dive planes.

The flight characteristics of underwater gliders are twofold: **1)** The most common trajectory is a *wings-levelled* flight where the heading is fixed and the pitch angle is non-zero. Accordingly, the glider performs symmetric upward and downward flights, also referred to as *yo-yo or saw-tooth maneuver*. **2)** To turn the glider, we can roll the glider body by rotating an internal mass. This will result in a *vertical spiral* if the rotating mass is remained offset from it's initial origin. During a vertical spiral the wings are no longer aligned in the vertical plane, similar to how fixed-wing airborne crafts turn. In practice, turning manoeuvres are occasionally made to adjust the heading of the vehicle, typically towards a desired path.

One of the main design considerations of the OASYS glider is *low-cost*. The implementation of navigation and guidance systems must consider a limited sensor suite, where key acoustic navigation instruments such as doppler velocity loggers (DVLs) are absent. This is however, also common in conventional underwater gliders, where DVLs are an optional payload. To avoid large navigation errors, the OASYS glider returns to the surface frequently to receive a *GPS fix*

The navigational payload in the OASYS glider consists of the following sensors:

- 9DOF IMU (Inertial Measurement Unit)
- Pressure/depth sensor
- GPS receiver (surface only)

1.2 Background

In this section we present a context of the main topics investigated in this thesis:

- Mathematical modelling of underwater gliders
- Path-following guidance
- Dead-reckoning (DR) navigation
- Control of underwater gliders
- Target-tracking of underwater gliders using unmanned surface vessels (USVs).

The following sections details a brief literature study of the latter topics.

1.2.1 Glider Dynamics

To simulate the motion of underwater gliders we need to derive a mathematical model of the glider dynamics. The model is represented as a set of differential equations which are typically solved in a numerical integrator to simulate the glider motions. These differential equations are based on the fundamental physics of the vehicle and its surroundings. The following pillars in physics are introduced for a submerged moving object - Classical mechanics (transnational and rotational motions of a rigid-body mass), hydrostatics (buoyancy and gravity forces), hydrodynamics (hydrodynamic forces and moments which acts on the vehicle), kinematics (geometrical motion). Detailed glider models based on the latter topics have been proposed in various literature, see e.g. [41, 60, 106, 113].

The rigid-body dynamics, which describe transnational and rotational motions of the vehicle, are the core of a mathematical glider model. In previous works, the classical mechanics have been derived using *Kirchhoff's equations of motion* [41, 60, 113] that describe the relationship between transnational and rotational motion and externally applied forces and moments. The externally applied forces and moments are results from

control actions, which are divided into two parts. This can be a result of a buoyancy propulsion system or internal moving mass actuators (alternatively external control surfaces such as rudders). A glider's main source of locomotion is the adjustable net buoyancy of the vehicle, allowing it to sink and rise in the water column. Furthermore, due to the hydrodynamic effects acting on the airfoil of the fixed wings, the vertical motion is transformed into a forward motion by the horizontal component of the vertical force, which is often referred to as *lift force* in glider nomenclature.

Applied control moments from the internal moving mass actuators alter the rotational motion of the vehicle. This is used to change the heading (direction) and pitch angle of the glider. From a modelling perspective, the internal moving mass is coupled with the glider body as presented in [41, 60, 106]. The transnational motion of an underwater glider is also highly influenced by *ocean currents*. Due to the absence of aft thrusters, the glider cruising speed can easily be altered by an ocean current in the water column. Hence, it's convenient to model these currents to more realistically reflect the glider dynamics. In many works the ocean current is assumed to be constant, irrotational and fixed with respect to an inertial frame [36, 41, 60].

A moving submerged vehicle will be introduced to *hydrodynamic* forces and moments. As gliders resemble fixed-wing aerial vehicles, the hydrodynamics have been modelled following aerodynamic theory in previous works [41, 60, 113]. In addition to hydrodynamic damping effects, there is hydrodynamic *added mass*. This occurs as the submerged vehicle displaces water while moving forward and is added as a virtual mass/inertia to the rigid-body dynamics in glider models [41, 60].

1.2.2 Path-Following

One of the main topics in this thesis is *path-following* - that is, to converge along a desired path without any time constraints. The path-following control problem is a well-established topic for underactuated marine vehicles (surface vessels, AUVs, underwater gliders), see e.g. [3, 11, 16, 19, 27, 30, 36, 38, 55, 79]. As most marine vehicles have underactuated sway dynamics - the inability to instantly move along the lateral axis, path-following controllers apply well to both surface and underwater vehicles. Guidance laws can be derived for both planar and vertical path following problems as presented in [9, 16, 55]. Vertical path following is however more relevant for thruster based AUVs. In buoyancy propelled underwater gliders, the vertical path is typically fixed by the pitching angle that generates the most optimized steady-state velocity [86, 91, 96, 113]. Hence, planar motion guidance laws, which allow the vehicle to follow paths in the horizontal plane, are the main foci in this thesis. The planar motion guidance law is a cascaded feedback law, which use navigational measurements, either in form of the predicted position or velocities as feedback, to compute the heading reference necessary for converging towards the desired path. A low-level control law is cascaded with the guidance law to assign control signals for the heading autopilot. As gliders spends most of their time in *wings-levelled* flights, we can assume that the path-following problem is parameterized by straight lines between desired waypoints, also referred to as *straight line path-following*.

Underwater gliders are often subject to ocean current disturbances. These disturbances are characterized as constant or slowly varying sea currents which have a magnitude and direction. Such environmental loads introduce drifts which makes it challenging to converge towards a desired path. Commercial *legacy* gliders such as *Slocum* and *Seaglider* introduce an optional current correction mode to compensate for ocean current drift in navigation and guidance systems [27, 31, 105]. Current compensating guidance laws for underwater gliders have been derived as a vectorial sum of the velocity vectors of the glider and the ocean current, see [19, 31, 105, 105].

In recent years, *Line-of-Sight (LOS)* guidance laws have received popularity in various underactuated marine vehicles, including underwater gliders, see e.g. [9, 16, 55, 56, 99, 102]. The LOS guidance law is derived by the *helsman* principle, in which the objective is to converge towards a point ahead of the vehicle, analogous to a helsman steering a boat. In presence of ocean current disturbances, an integral term can be added to the LOS guidance law to correct drifts as suggested in [9, 16, 55].

1.2.3 Navigation

A notorious challenge for gliders is to navigate in the the absence of GNSS systems under water. Traditionally, this is solved by dead-reckoning (DR) to predict the location of the vehicle given an initial position (GPS fix at surface). The principle of DR is to perform time integration of the transnational velocities, which produce the traveled distance in a local frame of reference. The velocities, which are measured in the body fixed frame, are rotated to the inertial frame before performing integration using the euler angles from the onboard IMU . Due to inevitable bias and random walk errors in IMUs and velocity estimation, time integration imposes a position drift which grows over time. To resolve this, gliders frequently surface to get a *GPS fix* to reinitialize the DR algorithm [31, 41, 60, 104].

Due to the low-power design of buoyancy driven gliders, the navigational suite is often limited to an IMU and a depth sensor. Commercial gliders such as Slocum use a set of simple geometric equations to approximate the planar position of the vehicle, where the transnational velocities are computed as vector components of the vertical velocity (rate-change of depth measurements) [104, 105]. Optionally, a doppler velocity logger (DVL) can be integrated in the glider payload to provide more accurate estimates of the relative velocities as presented in [25, 70, 97, 104]. However, DVLs are not always convenient to integrate as these operate based on the acoustic doppler shift principle and must be close to the seabed to get *bottom-lock* measurements. Some DVLs can measure the velocities with respect to water particles (*water-lock*), but this is not

considered a stationary frame of reference due to ocean currents and will impose drift errors depending on the current magnitude. Accordingly, DVLs are most useful when close to the seafloor, for instance in coastal and shallow water operations.

In [100] a *model-based* observer is proposed to aid DR navigation. An extended kalman filter (EKF) was developed based on the dynamic model of the Slocum glider. Such models include hydrodynamic properties of the vehicle, which are more accurate than the geometrical representations mentioned previously. Yet, the glider model containing intricate hydrodynamic coefficients is obtained through expensive towing-tank tests or/and CFD (computational fluid dynamics) simulations. However, the hydrodynamic models of popular commercial and research gliders are usually published in various research works and available for reuse, see [41, 60, 113].

In the recent time *machine/deep learning (ML/DL)* models have been proposed as *model-free* state estimators for DR navigation in marine vehicles. Various articles have suggested state estimators for surface vessels in GNSS denied scenarios and AUVs using recurrent neural networks (RNNs) [88, 114]. Given some ground truth measurements from navigational instruments, the networks are trained based on sequential learning. After the learning process, the networks can be employed as a supplement when DVL/GNSS sensors are denied or unavailable.

1.2.4 Control

Control in underwater gliders is typically referred to controlling the net buoyancy, pitch angle and heading angle. As the on-board variable buoyancy system consumes most of the power, it often has primitive open-loop on/off controllers and is only active in transition between upward and downward dives [31, 86, 100]. Due to the low-speed and symmetric design of underwater gliders, linear feedback controllers are typically implemented for pitch and heading control [43, 61, 76, 98, 112]. Commercial gliders such as Slocum and Seaglider have default decoupled PID (Proportional-Integral-Derivative) feedback controllers for pitch and heading [41, 89]. In research orientated gliders, MIMO (Multiple Input Multiple Output) linear feedback controllers like LQR (Linear Quadratic Regulation) [43, 98] and MPC (Model Predictive Control) [1] have been investigated.

Nonlinear feedback controllers have been introduced in research gliders. Control laws such as sliding-mode control [66, 107, 115] and adaptive back-stepping control [17, 18] have been proposed. However, the use of nonlinear feedback control requires detailed information about the glider dynamics, which is often inconvenient if the geometry of the glider has changed due to payload substitutes or changes in internal distribution of masses.

In recent time machine learning approaches to feedback control has been proposed using data-driven artificial neural networks [51, 52] and reinforcement learning [53, 93]. As glider designs are often iterated in the shape of added features or change of instrument payload, the dynamic properties changes. Hence, using a data-driven approach to feedback control could swiftly adjust to these changes without tuning complex mathematical models. However, these models do require experimental data to train on.

1.2.5 Target-Tracking

The final topic in this thesis is related to target localization using an unmanned surface vehicle (USV) for the purpose of collecting accurate trajectories of an underwater glider to be used in supervised neural network training. On-board navigation systems in underwater gliders are not suited as *ground truth* measurements to train machine/deep learning models. It is more convenient to collect experimental data using an acoustic positioning system as demonstrated in [5, 42]. Since gliders are designed to displace large distances, the acoustic positioning receivers (typically located on the surface) must move along the vehicle to stay within range of the submerged vehicle. In this regard, we want to localize the glider using unmanned surface vessels (USVs) in order to reduce operational costs and potential hazards. Furthermore, a topside vessel aims to track the glider motions. From a control perspective, the topside vessel must try to bound the planar distance to the submerged target. We refer to this control problem as *target-tracking* - to pursue a moving or stationary target whose future motions are not known [11, 36]. Topics in target tracking for unmanned marine vehicles was introduced in [12, 14, 15]. The target tracking guidance laws investigated in the latter works originate from missile guidance systems such as Pure Pursuit (PP), Constant Bearing (CB), and line-of-sight (LOS) guidance laws, designed to intercept moving or stationary targets. Extension of these guidance laws in underactuated marine vessels have been proposed in various literature [11, 12, 14, 15, 77, 95]. The target tracking guidance laws introduced in the latter works are composed of surge velocity and heading/course controllers due to under actuation in marine vessels, which combined achieve the target tracking control objective.

1.3 Thesis objective & Outline

The main objective of this thesis is to investigate topics in navigation, path-following, control and target tracking that can be implemented in the OASYS glider developed at OsloMet. The physical implementation of these systems is out of scope of this thesis as the vehicle is still under development. Hence, the topics investigated must consider the limitations of the OASYS glider, such as cost, size and power consumption. As the vehicle is not ready for ocean testing, a simulator environment is developed to validate the motion control systems investigated in this thesis.

1.3.1 Research Questions

Based on the latter description, this thesis aims to answer the following research questions:

- *How do we develop attitude and heading controllers for the underwater glider, assuming there is no hydrodynamic model available for the vehicle?*
- *Can machine learning models improve dead-reckoning navigation for underwater gliders?*
- *How do underwater gliders efficiently follow straight-line paths, and how well is it's performance considering significant navigational errors?*
- *How can we autonomously gather experimental data from underwater gliders using range-only localization?*

1.3.2 Conference Papers

Three conference papers have been written based on the main results from this master project. The following papers are considered to be a contribution to this thesis:

- [83] *Saksvik, I. B., Alcocer, A., & Hassani, V. (2021). A Deep Learning Approach To Dead-Reckoning Navigation For Autonomous Underwater Vehicles With Limited Sensor Payloads. Presented at Global Oceans 2021: Porto–San-Diego (pp. 1-10). IEEE.*

- [84] *Saksvik, I. B., Alcocer, A., & Hassani, V. (2022). Path-Following for Underwater Gliders With Limited Navigation Payloads. Draft submitted to the 14th IFAC CAMS: Kgs. Lyngby, Denmark*

- [85] *Saksvik, I. B., Alcocer, A., Hassani, V & Pascoal, A. (2022). Tracking Underwater Gliders Using Small Unmanned Surface Vessel (USV). Draft submitted to the 14th IFAC CAMS: Kgs. Lyngby, Denmark*

1.3.3 Thesis Outline

The outline of this master thesis is organized as follows:

- **Chapter 2** presents a mathematical model of the buoyancy driven underwater glider and heading and pitch feedback control systems. The model is derived in 6DOF (degrees of freedom) and details rigid-body dynamics, hydrostatic forces and hydrodynamic forces which acts on the submerged vehicle.

- **Chapter 3** addresses a *model-free* machine/deep learning approach to dead-reckoning navigation for underwater gliders. The proposed observer was validated on experimental data from a hybrid AUV/glider, where a doppler velocity logger (DVL) was used as a ground truth reference. The observer was also validated on the simulated glider dynamics from the mathematical model in chapter 2.

- **Chapter 4** is related to guidance systems and planar motion path following for underwater gliders. The chapter focuses on the principles of *look-a-head* guidance using line-of-sight (LOS) and integral line-of-sight (ILOS) steering laws for straight-line path-following problems. The guidance laws are simulated using the mathematical model presented in chapter 2.

- **Chapter 5** presents a target-tracking scheme of underwater gliders using an unmanned surface vessel (USV). This is a methodology for localizing underwater gliders using acoustic range measurements. The motivation behind this subject was to propose a autonomous platform for gathering experimental glider trajectories which can further be used to develop machine/deep learning models as presented in chapter 4.

- **Chapter 6** discuss the results from the different chapters and provide recommendations for further work

- **Appendix C: Conference paper 1** *Path-Following for Underwater gliders with Limted Navigation Payloads*

- **Appendix D: Conference paper 2** *Target Tracking of Underwater Gliders Using Small Unmanned Surface Vessels (USV's)*

- **Appendix E: Conference paper 3** *A Deep Learning Approach To Dead-Reckoning Navigation For Autonomous Underwater Vehicles With Limited Sensor Payloads*

Chapter 2

Modelling & Control of Underwater Gliders

The aim of this chapter is twofold - firstly, we want to derive a mathematical model of the underwater glider for simulation purposes and secondly, develop feedback control systems for attitude and heading control to be validated in the simulation framework. The mathematical model is mainly derived from Fossen's vectorial marine craft equations which originates from the work in [33–36, 39]. The vectorial marine craft dynamics formulates a general dynamic model for marine vehicles e.g., autonomous underwater vehicles (AUVs) and surface vessels as presented in previous works [3, 20, 29, 32, 33, 37, 37, 63, 79, 81, 81, 116]. A preliminary mathematical model for underwater gliders using the vectorial marine craft model has been made in previous ACIT master projects [49, 50]. Due to lack of hydrodynamic characterization of the OASYS glider, the proposed simulated glider model use the parameters of the Seawing glider presented in [108, 110, 113], which is a scaled version of the OASYS glider with similar shape and control actuators.

The control section presents two decoupled PID controllers for heading and pitch control. As there does not exist a dynamic model for the OASYS glider, we aim to develop

system identification models from experimental datasets for the control plants. Accordingly, nonlinear auto-regressive exogenous (NARX) models were used to identify these plants and further used to autotune the PID controllers in MATLAB.

The mathematical model derived in this chapter consists of five sections in the following order:

- The *rigid-body dynamics* of the glider is addressed in section 2.2. This section details the transnational and rotational motions of the vehicle.
- Section 2.3 details the *kinematic* relationships of the glider, which describe geometric motions.
- The *restoring forces*, also referred to as *hydrostatics* is described in section 2.4. The restoring forces of a submerged underwater object relates to gravitational and buoyant forces.
- In section 2.5 the *hydrodynamics* are detailed. This section is divided into two parts - The first section details hydrodynamic forces and moments, while the second section describes hydrodynamic added mass effects.
- The implementation and open-loop simulations of the *numerical model* in MATLAB/SIMULINK is addressed in section 2.6.

2.1 Preliminaries

We start by defining the reference frames in which the model is formulated. The geometric orientation and position of an underwater glider is derived relative to an inertial frame, while the angular and linear velocities are defined in a body-fixed frame [36].The state variables presented for the marine craft dynamics are defined following SNAME [90] nomenclature as

DOF	Description	Positions	Velocities	Forces
1	Surge	x	u	D
2	Sway	y	v	SF
3	Heave	z	w	L
4	Roll	ϕ	p	K
5	Pitch	θ	q	M
6	Yaw	ψ	r	N

Table 2.1: SNAME nomenclature

The nomenclature in table 2.1 is defined in vectors by

$$\begin{aligned} \boldsymbol{\eta} &= \begin{bmatrix} x & y & z & \phi & \theta & \psi \end{bmatrix}^T \\ \boldsymbol{\nu} &= \begin{bmatrix} u & v & w & p & q & r \end{bmatrix}^T \\ \boldsymbol{\tau}_c &= \begin{bmatrix} D & SF & L & K & M & N \end{bmatrix}^T \end{aligned} \tag{2.1}$$

The vector $\boldsymbol{\eta}$ describes the position and orientation in the the inertial frame $\{n\}$, while $\boldsymbol{\nu}$ and $\boldsymbol{\tau}$ are represented in the body-fixed frame of the vehicle $\{b\}$.

Remark. *Note that the hydrodynamic forces D,SF,L = drag, sideforce, lift are modifications of the SNAME notation. The forces are traditionally represented by X,Y,Z [33, 36, 90].*

Following [33–36, 39], the 6DOF dynamics for a submerged underwater vehicle is derived as

$$\boldsymbol{M}\dot{\boldsymbol{\nu}} + \boldsymbol{C}(\boldsymbol{\nu})\boldsymbol{\nu} + \boldsymbol{D}(\boldsymbol{\nu}) + \boldsymbol{g}(\boldsymbol{\eta}) = \boldsymbol{\tau}_c \tag{2.2}$$

where:

- $\boldsymbol{M} \in \mathbb{R}^{6\times 6}$ - Is the system inertia matrix that describes the transnational rigid-body dynamics and correlating added mass effects.

- $\boldsymbol{C}(\boldsymbol{\nu}) \in \mathbb{R}^{6\times6}$ - Defines the system coriolis and centripetal matrix that forms the rotational rigid-body dynamics with rotational added mass effects

- $\boldsymbol{D}(\boldsymbol{\nu}) \in \mathbb{R}^{6\times6}$ - Is the hydrodynamic damping matrix that describes the hydrodynamic forces and moments that act on the vehicle. The hydrodynamic forces and moments for a fixed-wing gliders share similarities with aerodynamic forces such as drag forces, sideforce and lift forces.

- $\boldsymbol{g}(\boldsymbol{\eta}) \in \mathbb{R}^{6\times1}$ - Details the hydrostatic forces, which are results of gravitational and buoyant effects.

- $\boldsymbol{\tau}_c \in R^{6\times1}$ - Describes the control force vector, which consists of external applied forces and moments that acts on the vehicle.

We start to derive some assumptions about the general marine craft dynamics in eq. 2.2 to suit the motions of an underwater glider:

Assumption 1. *The applied control forces and moments which acts on the vehicle are considered constraint forces, hence* $\boldsymbol{\tau_c} = \mathbf{0}^{6\times1}$

Assumption 2. *The hydrostatic forces* $\boldsymbol{g(\eta)}$ *are derived based on a variable buoyant vehicle*

Remark. *Control moments in underwater gliders are a result of slowly moving internal mass actuators that are translated and rotated along a rail inside the vehicle housing. To avoid modelling complex coupled rigid body dynamics between the two systems, which in practice are only "slightly interactive", we follow assumption 1 by neglecting these effects and consider the moving mass system as constraint forces. As the mathematical model is used for simulation purposes only, and not to derive model-based control systems or observers, we accept the unmodelled actuator dynamics.*

2.1.1 The Relative Velocity Model

The marine craft dynamics presented in equation 2.2 are derived by the velocity vector $\boldsymbol{\nu} \in R^6$. In real ocean conditions, the velocity vector will have an ocean current component. Thus, we rewrite the marine craft dynamics using a relative velocity model.

Assumption 3. *The glider dynamics and kinematics are influenced by an ocean current V_c that is constant and irrotational in the inertial frame - $\dot{V}_c^n = 0$*

Assumption 4. *The ocean current is defined by the planar vector components: $V_c^n = [V_x^n, V_y^n, 0]^T$. Vertical ocean currents are neglected, $V_z^n \approx 0$*

Remark. *On a macro scale, ocean currents are not assumed constant and irrotational. However, since marine vehicles tends to operate at a micro scale, where ocean currents are slowly changing, we can follow assumption 3 and simplify the ocean current model.*

Following assumption 3, 5, and [36], the ocean current vectors in the body-fixed frame $\boldsymbol{\nu}_c^b = [u_c^b, v_c^b, 0]^T$ are given by

$$\boldsymbol{\nu}_c^b = \begin{bmatrix} V_c^n \cdot cos(\beta_c - \psi) \\ V_c^n \cdot sin(\beta_c - \psi) \\ 0 \end{bmatrix}, \; V_c^n = \sqrt{u_c^n + v_c^n} \tag{2.3}$$

Where β_c is the direction of the ocean current. The relative velocity vector is then defined as $\boldsymbol{\nu}_r = \boldsymbol{\nu} - \boldsymbol{\nu_c^b} = [u - u_c^b, v - v_c^b, 0, 0, 0, 0]^T$. Finally, the marine craft dynamics in eq. 2.2 are rewritten in a relative velocity model derived by

$$\boldsymbol{M}_{rb}\dot{\boldsymbol{\nu}}_r + \boldsymbol{M_A}\dot{\boldsymbol{\nu}}_r + \boldsymbol{C}_{rb}(\boldsymbol{\nu}_r)\boldsymbol{\nu_r} + \boldsymbol{C}_A(\boldsymbol{\nu}_r)\boldsymbol{\nu_r} + \boldsymbol{D}(\boldsymbol{\nu_r}) + \boldsymbol{g}(\boldsymbol{\eta}) = \boldsymbol{\tau}_c \tag{2.4}$$

In the latter equation we introduce two new matrices, $\boldsymbol{M}_A \in \mathrm{R}^{6\times6}$ and $\boldsymbol{C}_A(\boldsymbol{\nu}_r) \in \mathrm{R}^{6\times6}$ which are the added mass matrices correlating to transnational and rotational motion, and will be addressed later in this chapter. The marine craft dynamics is often described in a simplified notation where $\boldsymbol{M} = \boldsymbol{M}_A + \boldsymbol{M}_{rb}$ and $\boldsymbol{C}(\boldsymbol{\nu}_r) = \boldsymbol{C}_{rb}(\boldsymbol{\nu}_r) + \boldsymbol{C}_A(\boldsymbol{\nu}_r)$

2.1.2 Distribution of Masses

There are multiple masses to consider in an underwater glider. Firstly there is the internal moving mass system denoted m_p, which can be translated and rotated along a rail inside the vehicle housing. Next we have a buoyancy mass m_b, often represented as an oil reservoir inside the housing. Lastly there are the hull mass m_h and static mass m_s, where the static mass consists of all the other components inside the vehicle. All masses are defined in three-dimensional Cartesian space by a vector $\boldsymbol{r}_{m_i} \in \mathbb{R}^3$ with respect to a center of origin (CO). Following previous works [41, 60], the center of buoyancy (CB) vector is aligned with CO. The geometric center of buoyancy is located at the center of the displaced fluid/water. Assuming a symmetric prolate spheroid hull shape, CB is located at the center of the symmetric glider body.

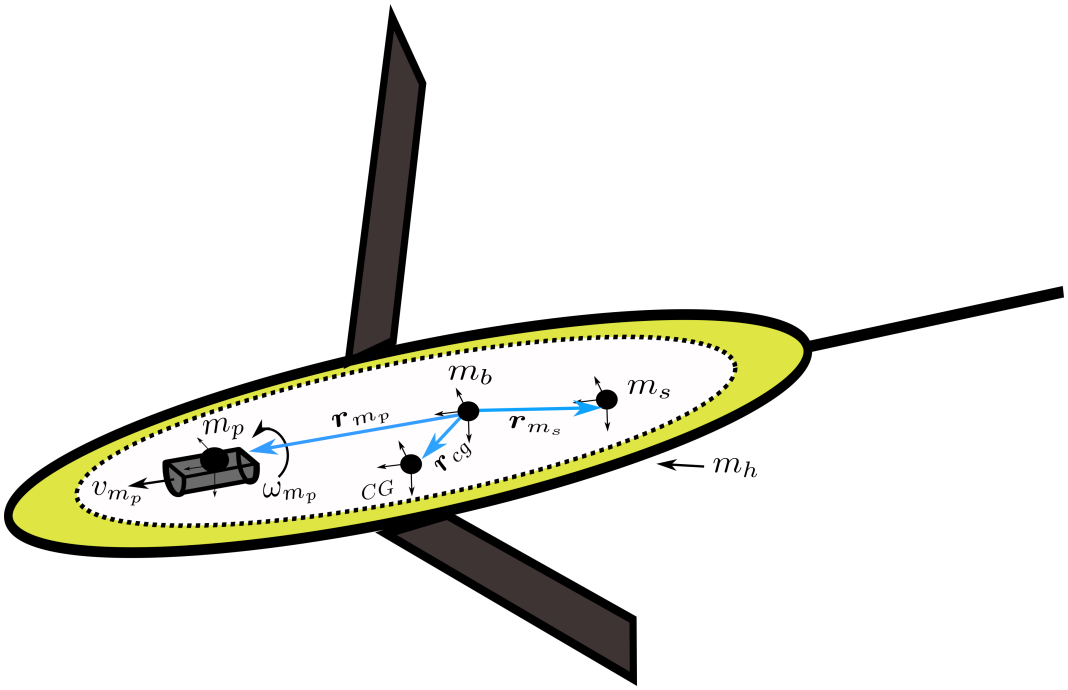

Figure 2.1: Distribution of glider masses

Remark. *Note that the location of the masses in 2.1 are not necessarily ideal for glider designs, but merely used for illustration purposes.*

We define the masses and vector definitions of the notation in figure 2.1 as

- CB: The center of buoyancy is an origin and located at the center of the displaced fluid. Hence, $CB = [x_{cb}, y_{cb}, z_{cb}]^T = [0, 0, 0]^T$. Note that CB coincides with m_b in figure 2.1.
- CG is the center of gravity vector denoted by $CG = [x_{cg}, y_{cg}, z_{cg}]^T$
- m_h is the hull mass, with a vector $\boldsymbol{r}_{m_h} = [x_{m_h}, y_{m_h}, z_{m_h}]^T$. Since the hull mass is uniformly distributed, we neglect $\boldsymbol{r}_{m_h}$ when computing the center of gravity vector.
- m_s is the static mass, composed of the electronics and internal components (except the moving mass system and hull mass) and have the vector $\boldsymbol{r}_{m_s} = [x_{m_s}, y_{m_s}, z_{m_s}]^T$ with respect to CB.
- m_p is the moving mass, which typically consists of a custom-shaped battery pack that can be translated and rotated inside the housing. It's vector is denoted by $\boldsymbol{r}_{m_p} = [x_{m_p}, y_{m_p}, z_{m_p}]^T$ with respect to CB. Note that the moving mass vector is not fixed in time.
- m_b is the buoyancy mass, which is an oil reservoir located inside the glider housing with a vector $\boldsymbol{r}_{m_b} = [x_{m_b}, y_{m_b}, z_{m_b}]^T$. This mass is often located in the front or back to aid pitching moments when altering between upward and downward glides. However, when deriving the glider dynamics, the oil mass is often considered fixed and aligned with CB [41, 60, 113] to simplify the mathematical model.

2.2 Rigid-Body Dynamics

The rigid-body dynamics of an underwater glider can be derived in terms of transnational and rotational motions. Transnational rigid-body dynamics is described by the system inertia matrix $\boldsymbol{M}_{rb}$, while the rotational rigid-body dynamics is determined by the Coriolis and centripetal matrix $\boldsymbol{C}_{rb}(\boldsymbol{\nu}_r)$. The rigid-body dynamics described in the vectorial marine craft equations originates from Newtonian mechanics using the renowned Newton-Euler equations. In underwater vehicles it's convenient to derive the rigid-body dynamics at the center of buoyancy CB [36, 41, 60], and not the center of gravity CG which is more common for non-submerged bodies. The Newton-Euler equations in matrix notation are derived following the work in [34, 34, 36, 39]

$$\boldsymbol{M}_{rb}\dot{\boldsymbol{\nu}} + \boldsymbol{C}_{rb}(\boldsymbol{\nu})\boldsymbol{\nu} + = \boldsymbol{\tau}_{rb} \tag{2.5}$$

where $\boldsymbol{\tau}_{rb}$ represents the forces and moments acting on the rigid-body. We fist introduce some assumption about the rigid-body dynamics.

Assumption 5. *The transnational and rotational rigid-body dynamics are derived about a center of origin (CO) that coincides with the center of the displaced fluid, also referred to as CB*

Remark. *It's common to derive the glider dynamics about the center of buoyancy as suggested in previous works [41, 60, 113].*

2.2.1 Preliminaries

We start by deriving the Newton-Euler equations about the center of gravity CG, which will later be transformed to the center of buoyancy CB.

Consider an arbitrary vector $\boldsymbol{x} \in \mathbb{R}^3$, that satisfies $\boldsymbol{S}(\boldsymbol{x})\boldsymbol{y} = \boldsymbol{x}$ x $\boldsymbol{y}$, where $\boldsymbol{S}$ is given by

$$\boldsymbol{S}(\boldsymbol{x}) = \begin{bmatrix} 0 & -x_3 & x_2 \\ x_3 & 0 & -x_1 \\ -x_2 & x_1 & 0 \end{bmatrix}, \ \boldsymbol{x} \in \{x_1, x_2, x_3\} \tag{2.6}$$

The skew-symmetric properties in 2.6 are further exploited to derive the translational and rotational motion of a rigid body.

2.2.2 Newton-Euler Equations

Following [33, 36] the transnational and rotational dynamics are represented by a force vector $\boldsymbol{f}_{cg} \in \mathbb{R}^3$ and moment vector $\boldsymbol{m}_{cg} \in \mathbb{R}^3$

$$\begin{bmatrix} \boldsymbol{f}_{cg} \\ \boldsymbol{m}_{cg} \end{bmatrix} = \boldsymbol{M}_{cg} \begin{bmatrix} \dot{\boldsymbol{v}}_{cg} \\ \dot{\boldsymbol{\omega}}_{cb} \end{bmatrix} + \boldsymbol{C}_{cg} \begin{bmatrix} \boldsymbol{v}_{cg} \\ \boldsymbol{\omega}_{cb} \end{bmatrix}, \ \in \mathbb{R}^6 \tag{2.7}$$

If we expand the inertia matrix $\boldsymbol{M}_{cg}$ and the Coriolis and centripetal matrix $\boldsymbol{C}_{cg}$, equation 2.7 can be rewritten as

$$\begin{bmatrix} \boldsymbol{f}_{cg} \\ \boldsymbol{m}_{cg} \end{bmatrix} = \begin{bmatrix} m\boldsymbol{I}_{\boldsymbol{3\times 3}} & \boldsymbol{0}_{\boldsymbol{3\times 3}} \\ \boldsymbol{0}_{\boldsymbol{3\times 3}} & \boldsymbol{I}_{cg} \end{bmatrix} \begin{bmatrix} \dot{\boldsymbol{v}}_{cg} \\ \dot{\boldsymbol{\omega}}_{cb} \end{bmatrix} + \begin{bmatrix} m\boldsymbol{S}(\boldsymbol{\omega}_{cb}) & \boldsymbol{0}_{\boldsymbol{3\times 3}} \\ \boldsymbol{0}_{\boldsymbol{3\times 3}} & -\boldsymbol{S}(\boldsymbol{I}_{cg}\boldsymbol{\omega}_{cb}) \end{bmatrix} \begin{bmatrix} \boldsymbol{v}_{cg} \\ \boldsymbol{\omega}_{cb} \end{bmatrix} \tag{2.8}$$

Equation 2.8 represents the Newton-Euler equations with respect to the body-fixed center of gravity (CG). For submerged underwater vehicles, it is convenient to represent the equations of motion about the center of buoyancy (CB). A coordinate transformation is needed to map the rigid body dynamics about a new body-fixed coordinate frame CB. Following [36] a coordinate transformation matrix can be defined by

$$\boldsymbol{Z}(\boldsymbol{r}_{cg}) = \begin{bmatrix} \boldsymbol{I}_{\boldsymbol{3\times 3}} & \boldsymbol{S}(\boldsymbol{r}_{cg}) \\ \boldsymbol{0}_{\boldsymbol{3\times 3}} & \boldsymbol{I}_{\boldsymbol{3\times 3}} \end{bmatrix}, \quad \boldsymbol{Z}^T(\boldsymbol{r}_{cg}) = \begin{bmatrix} \boldsymbol{I}_{\boldsymbol{3\times 3}} & \boldsymbol{0}_{\boldsymbol{3\times 3}} \\ \boldsymbol{S}(\boldsymbol{r}_{cg}) & \boldsymbol{I}_{\boldsymbol{3\times 3}} \end{bmatrix} \tag{2.9}$$

Furthermore we can use the coordinate transformation matrix to convert the Newton-Euler equations to the body-fixed frame CB.

$$\boldsymbol{Z}^T(\boldsymbol{r}_{cg}) \begin{bmatrix} \boldsymbol{f}_{cg} \\ \boldsymbol{m}_{cg} \end{bmatrix} = \boldsymbol{Z}^T(\boldsymbol{r}_{cg}) \boldsymbol{M}_{cg} \boldsymbol{Z}(\boldsymbol{r}_{cg}) \begin{bmatrix} \dot{\boldsymbol{v}}_{cg} \\ \dot{\boldsymbol{\omega}}_{cb} \end{bmatrix} + \boldsymbol{Z}^T(\boldsymbol{r}_{cg}) \boldsymbol{C}_{cg} \boldsymbol{Z}(\boldsymbol{r}_{cg}) \begin{bmatrix} \boldsymbol{v}_{cg} \\ \boldsymbol{\omega}_{cb} \end{bmatrix} \tag{2.10}$$

From the new Newton-Euler equations with respect to CB we can rewrite the inertia matrix and Coriolis and centripetal matrix as

$$\boldsymbol{M}_{cb} = \boldsymbol{Z}^T(\boldsymbol{r}_{cg}) \boldsymbol{M}_{cg} \boldsymbol{Z}(\boldsymbol{r}_{cg}) = \begin{bmatrix} m\boldsymbol{I}_{\boldsymbol{3\times 3}} & -m\boldsymbol{S}(\boldsymbol{r}_{cg}) \\ m\boldsymbol{S}(\boldsymbol{r}_{cg}) & \boldsymbol{I}_{cg} - m\boldsymbol{S}^2(\boldsymbol{r}_{cg}) \end{bmatrix}$$

$$\boldsymbol{C}_{cb} = \boldsymbol{Z}^T(\boldsymbol{r}_{cg}) \boldsymbol{C}_{cg} \boldsymbol{Z}(\boldsymbol{r}_{cg}) = \begin{bmatrix} m\boldsymbol{S}(\boldsymbol{\omega}_{cb/n}) & -m\boldsymbol{S}(\boldsymbol{\omega}_{cb/n})\boldsymbol{S}(\boldsymbol{r}_{cg}) \\ m\boldsymbol{S}(\boldsymbol{\omega}_{cb/n})\boldsymbol{S}(\boldsymbol{r}_{cg}) & -\boldsymbol{S}((\boldsymbol{I}_{cg} - m\boldsymbol{S}^2(\boldsymbol{r}_{cg})\boldsymbol{\omega}_{cb/n}) \end{bmatrix} \tag{2.11}$$

The inertia terms in equation 2.11 defined by $\boldsymbol{I}_{cg} - m\boldsymbol{S}^2(\boldsymbol{r}_{cg})$ are derived using the Parallel Axes theorem [36], [41], where the inertia is diagonal $I = diag(I_x, I_y, I_z)$. We start by deriving the static inertia of the underwater glider following the theory in [41,62] yielding

$$\boldsymbol{I_s} = \boldsymbol{I_h} - m_t \boldsymbol{S}(\boldsymbol{r}_{cg}) \boldsymbol{S}(\boldsymbol{r}_{cg}) \tag{2.12}$$

Where $\boldsymbol{I_h}$ relates to the inertia of the uniformly distributed hull of the glider. The total rigid body inertia $\boldsymbol{I}_{rb}$ is derived by adding the static inertia term $\boldsymbol{I}_s$ with the inertia for the moving mass system $\boldsymbol{I}_{m_p}$ such that

$$\boldsymbol{I}_{rb} = \boldsymbol{I}_s + \boldsymbol{I}_{m_p} \tag{2.13}$$

The inertia of the internal moving mass system is defined by a principal rotation matrix of the servo angle γ and the static inertia $\boldsymbol{I_0}$ [60, 113]

$$\boldsymbol{I}_{m_p} = \boldsymbol{R}^{\boldsymbol{T}}_{\boldsymbol{m_p}}(\gamma) \boldsymbol{I_0} \boldsymbol{R}_{\boldsymbol{m_p}}(\gamma) \tag{2.14}$$

As the cylindrical battery pack is rotated about the body-fixed x-axis of the glider, we need to use a rotation matrix that maps the rotation of the servo angle γ about the body x-axis given as

$$\boldsymbol{R_{m_p}}(\gamma) = \begin{bmatrix} 1 & 0 & 0 \\ 0 & cos(\gamma) & -sin(\gamma) \\ 0 & sin(\gamma) & cos(\gamma) \end{bmatrix} \tag{2.15}$$

Given a radius, length L_p, width w_p and depth d_p and mass m_p, we can compute the static inertia of a semi cylinder following [26, 62]

$$\boldsymbol{I}_0 = \begin{bmatrix} \frac{m_p}{12}(w_p^2 + L_p^2) & 0 & 0 \\ 0 & \frac{m_p}{12}(w_p^2 + L_p^2) & 0 \\ 0 & 0 & \frac{m_p}{12}(d_p^2 + w_p^2) \end{bmatrix} \tag{2.16}$$

Remark. *When the rolling mass is located at it's origin $\gamma = 0$ the rotation matrix $\boldsymbol{R}_{m_p}(0)$ results in a identity matrix with diagonal ones. Hence, when $\gamma = 0$ we can rewrite the inertia as $\boldsymbol{I}_{rb} = \boldsymbol{I}_s + \boldsymbol{I}_{m_p} = \boldsymbol{I_h} - m_t\boldsymbol{S}^2(\boldsymbol{r}_{cg}) + \boldsymbol{I_0}$*

The vector locating the center of gravity is a sum of the masses and correlating positions divided by the total mass. Following [34, 41, 60] we have

$$\boldsymbol{r}_{cg} = \frac{\sum m_i \boldsymbol{r}_{mi}}{m_t} = \frac{m_s\boldsymbol{r}_{m_s} + m_p\boldsymbol{r}_{m_p} + m_b\boldsymbol{r}_b + m_h\boldsymbol{r}_{m_h}}{m_p + m_s + m_b + m_h} \tag{2.17}$$

Where $\boldsymbol{r_{m_i}} = [x_{m_i}, y_{m_i}, z_{m_i},]^T$ is the x-y-z coordinates of the ith masses with respect to the origin located at CB. According to [41] the hull mass m_h is uniformly distributed, meaning that the vector $\boldsymbol{r}_{m_h}$ coincides with the center of origin $\boldsymbol{r}_{m_h} = [0, 0, 0]$. The buoyancy mass (internal oil tank) is often located in the front or back to induce a pitching moment during transitions between upward and downward glides [41, 60]. However, the location of the mass is not always known and often assumed aligned with CB as in [41, 62]. Given a radius of the cylindrical battery pack r_c the servo angle of the rotating actuator γ, the position of the moving mass system is defined by [60, 60, 113]

as

$$\boldsymbol{r}_{m_p} = \begin{bmatrix} r_{x_p} \\ r_{y_p} \\ r_{z_p} \end{bmatrix} = \begin{bmatrix} r_{x_p} \\ r_c \cdot cos(\gamma + \pi/2) \\ r_c \cdot sin(\gamma + \pi/2) \end{bmatrix} \tag{2.18}$$

For semi-cylindrical moving mass systems, the mass is rotated within the space of $\gamma \in \{-\pi/2, \pi/2\}$ rad. Where the origin $\gamma_0 = 0$ rad is located at the lower part of the cylindrical housing.

Finally, we rewrite the translational dynamics into the systen inertia matrix following [33, 34, 36] with the properties $\boldsymbol{M}_{rb} = \boldsymbol{M}_{rb}^T > 0$ and $\dot{\boldsymbol{M}}_{rb} = \boldsymbol{0} \in \mathbb{R}^{6\times6}$

$$\boldsymbol{M}_{rb} = \begin{bmatrix} m\boldsymbol{I}_{3\times3} & -m\boldsymbol{S}(\boldsymbol{r}_{cg}) \\ m\boldsymbol{S}(\boldsymbol{r}_{cg}) & \boldsymbol{I}_{rb} \end{bmatrix}$$

$$= \begin{bmatrix} m_t & 0 & 0 & 0 & m_t z_{cg} & -m_t y_{cg} \\ 0 & m_t & 0 & -m_t z_{cg} & 0 & m_t x_{cg} \\ 0 & 0 & m_t & m_t y_{cg} & -m_t x_{cg} & 0 \\ 0 & -m_t z_{cg} & m_t y_{cg} & I_x & 0 & 0 \\ m_t z_{cg} & 0 & -m_t x_{cg} & 0 & I_y & -I_{yz} \\ -m_t y_{cg} & m_t x_{cg} & 0 & 0 & -I_{zy} & I_z \end{bmatrix} \tag{2.19}$$

Remark. *Recall that the inertia matrix is given by* $\boldsymbol{I}_{rb} = \boldsymbol{I}_s + \boldsymbol{I}_{m_p} = \boldsymbol{I_h} - m_t\boldsymbol{S}^2(\boldsymbol{r}_{cg}) + \boldsymbol{R}_{\boldsymbol{m_p}}^{\boldsymbol{T}}(\gamma)\boldsymbol{I_0}\boldsymbol{R}_{\boldsymbol{m_p}}(\gamma)$

The Coriolis and centripetal matrix $\boldsymbol{C(\nu)}$ describe the rotational dynamics of a rigid-body. According to [33, 34, 36] the Coriolis and centripetal matrix is symmetrical such that $\boldsymbol{C}_{rb}(\boldsymbol{\nu}) = -\boldsymbol{C}_{rb}^{T}(\boldsymbol{\nu})$ is satisfied. Accordingly, we have

$$\boldsymbol{C}_{rb}(\boldsymbol{\nu}_r) = \begin{bmatrix} \mathbf{0}_{3\times 3} & -m_t\boldsymbol{S}(\boldsymbol{v}) - m_t\boldsymbol{S}(\boldsymbol{\omega})\boldsymbol{S}(\boldsymbol{r}_{cg}) \\ \\ -m_t\boldsymbol{S}(\boldsymbol{v}) + m_t\boldsymbol{S}(\boldsymbol{r_{cg}})\boldsymbol{S}(\boldsymbol{\omega}) & -\boldsymbol{S}(\boldsymbol{I}_{rb}\boldsymbol{\omega}) \end{bmatrix} \tag{2.20}$$

The expanded matrix of (2.20) can be defined as

$$\boldsymbol{C}_{rb}(\boldsymbol{\nu}_r) = \begin{bmatrix} 0 & 0 & 0 \\ 0 & 0 & 0 \\ 0 & 0 & 0 \\ -m_t(y_{cg}q + z_{cg}r) & m_t(y_{cg}p + w) & m_t(z_{cg}p - v) \\ m_t(x_{cg}q - w) & -m_t(z_{cg}r + x_{cg}p) & m_t(z_{cg}q + u) \\ m_t(x_{cg}r - v) & m_t(y_{cg}r - u) & -m_t(x_{cg}p + y_{cg}q) \end{bmatrix} \\ \begin{bmatrix} m_t(y_{cg}q + z_{cg}r) & -m_t(x_{cg}q - w) & -m_t(x_{cg}r + v) \\ -m_t(y_{cg}p + w) & m_t(z_{cg}r + x_{cg}p) & -m_t(y_{cg}r - u) \\ -m_t(z_{cg}p - v) & -m_t(z_{cg}q + u) & m_t(x_{cg}p + y_{cg}q) \\ 0 & -I_{yz}q + I_z r & I_{yz}r - I_y q \\ I_{yz}q - I_z r & 0 & I_x p \\ -I_{yz}r + I_y q & I_x p & 0 \end{bmatrix} \tag{2.21}$$

2.3 Kinematics

Kinematics of a rigid body describes the geometric aspects of motion without including forces and moments. Kinematics are derived in an inertial North-East-Down (NED) reference frame [33, 34, 36]. The NED frame is defined by the local coordinates $\{n\} = [x_n, y_n, z_n]^T$ relative to an origin o_n that is fixed. Furthermore, the x-axis points north, the y-axis points east and the z-axis points downward.

The kinematic equations of an underwater vehicle is represented by the vector $\boldsymbol{\eta} = [x, y, z, \phi, \theta, \psi]^T$, which contains transnational and angular positions of the vehicle. Be-

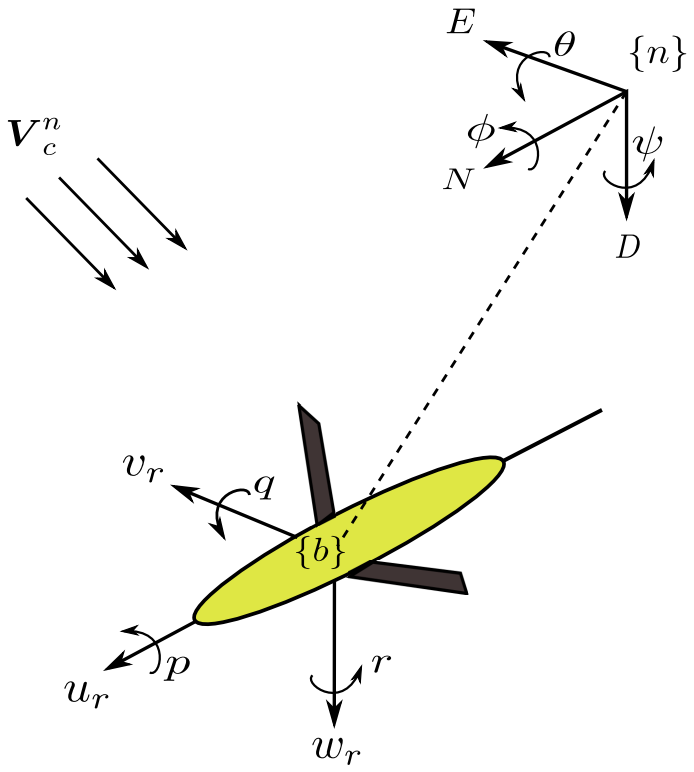

Figure 2.2: Glider kinematics

fore deriving the kinematic equations, we introduce some assumptions:

Assumption 6. *The kinematic equations are true for all euler angle combinations* $\boldsymbol{\Theta} = [\phi, \theta, \psi]^T$ *except for the geometric point where* $\theta = \pi/2$

Assumption 7. *The kinematics are influenced by a constant and irrotational ocean current* $\boldsymbol{V}_c^n$ *that is fixed in the inertial frame.*

Remark. *Assumption 6 is true when using euler angle representation of the kinematics. The trigonometric equations suffer from a singularity at specific points. This phenomena is often referred to gimbal lock, see e.g., [22,45] for more details on this topic. The kinematics can alternatively be represented by unit quaternions to avoid the singularity problem [36].However, since we are not operating close to the singularity at* $\theta = \pi/2$*, we can use an euler angle representation.*

Following [36] the 6DOF kinematic equations are given by

$$\dot{\boldsymbol{\eta}} = \boldsymbol{J}(\boldsymbol{\eta})\boldsymbol{\nu}_r + \boldsymbol{V}_c^n \tag{2.22}$$

We can expand this to

$$\begin{bmatrix} \dot{\boldsymbol{P}}_b^n \\ \dot{\boldsymbol{\theta}} \end{bmatrix} = \begin{bmatrix} \boldsymbol{R}_b^n(\boldsymbol{\Theta}) & \boldsymbol{0}_{3\times3} \\ \boldsymbol{0}_{3\times3} & \boldsymbol{T}_b^n(\boldsymbol{\Theta}) \end{bmatrix} \cdot \begin{bmatrix} \boldsymbol{\nu}_1 \\ \boldsymbol{\nu}_2 \end{bmatrix} + \begin{bmatrix} \boldsymbol{V}_c^n \\ \boldsymbol{0}_{3\times1} \end{bmatrix} \tag{2.23}$$

Where $\boldsymbol{\upsilon} = [u_r, v_r, w_r]^T$ and $\boldsymbol{\omega} = [p, q, r]^T$ .Following [36], the transformation between the body frame {b} and NED-frame {n} can be described trough the Euler angle rotation matrix $\boldsymbol{R}_b^n(\boldsymbol{\Theta})$ by a zyx-convention.

$$\boldsymbol{R}_b^n(\boldsymbol{\Theta}) = \begin{bmatrix} c\psi c\theta & -s\psi c\phi + c\psi s\theta s\psi & s\psi s\phi + c\psi c\phi s\theta \\ s\psi c\theta & c\psi c\phi + s\phi c\phi s\theta s\psi & -c\psi s\phi + s\theta s\psi c\phi \\ -s\theta & c\theta s\phi & c\theta c\phi \end{bmatrix} \tag{2.24}$$

Where c = cos() and s = sin()

The relationship between inertial velocities $\dot{\boldsymbol{P}}_n^b = [\dot{N}, \dot{E}, \dot{D}]^T$ and body-fixed velocities $\boldsymbol{\upsilon}$ is derived by

$$\dot{\boldsymbol{P}}_{\boldsymbol{b}}^{\boldsymbol{n}} = \boldsymbol{R}_b^n(\boldsymbol{\Theta}) \cdot \boldsymbol{\upsilon} \tag{2.25}$$

The expanded form of the inertial velocities are given as

$$\begin{aligned}
\dot{N} =& u_r \cdot cos(\psi)cos(\theta) + v_r \cdot [cos(\psi)sin(\theta)sin(\phi) - sin(\psi)cos(\phi)] + \\
& w_r \cdot [sin(\psi)sin(\phi) + cos(\psi)cos(\phi)sin(\theta)] + V_x^n \\
\dot{E} =& u_r \cdot sin(\psi)cos(\theta) + v_r[cos(\psi)cos(\phi) + sin(\phi)sin(\theta)sin(\psi)] + V_y^n \\
\dot{D} =& - u_r \cdot sin(\theta) + v \cdot cos(\theta)sin(\phi) + w_r \cdot cos(\theta)cos(\phi)
\end{aligned} \tag{2.26}$$

Following [33, 34, 36] the euler rates $\dot{\boldsymbol{\Theta}}_{\boldsymbol{n}} = [\dot{\phi}, \dot{\theta}, \dot{\psi}]^T$ are defined by multiplying the angular velocities $\boldsymbol{\omega} = [p, q, r]^T$ by a transformation matrix $\boldsymbol{T}_{\boldsymbol{b}}^{\boldsymbol{n}}(\boldsymbol{\Theta})$, yielding

$$\dot{\boldsymbol{\Theta}}_n^b = \boldsymbol{T}_b^n(\boldsymbol{\Theta}) \cdot \boldsymbol{\omega} = \begin{bmatrix} 1 & s\phi t\theta & c\phi t\theta \\ 0 & c\phi & -s\phi \\ 0 & s\phi/c\theta & c\phi/c\theta \end{bmatrix} \cdot \begin{bmatrix} p \\ q \\ r \end{bmatrix} \tag{2.27}$$

Remark. *The transformation matrix in eq. 2.27 is not defined when* $\theta = +- \frac{\pi}{2}$. *In the scenario where the pitch angle is 90 degrees a singularity occurs*

The euler rates in eq. 2.27 are expanded such that

$$\begin{aligned}
\dot{\phi} =& p + q \cdot sin(\phi)tan(\theta) + r \cdot cos(\phi)tan(\theta) \\
\dot{\theta} =& q \cdot cos(\phi) - r \cdot sin(\phi) \\
\dot{\psi} =& q \cdot \frac{sin(\phi)}{cos(\theta)} + r \cdot \frac{cos(\phi)}{cos(\theta)}, \theta \neq +- \frac{\pi}{2}
\end{aligned} \tag{2.28}$$

2.4 Restoring Forces

The restoring forces of an underwater glider relate to hydrostatic forces due to buoyancy and gravity [33, 34, 36]. The gravitational force $\boldsymbol{f}_g^n \in \mathbb{R}^3$ works trough the center of gravity of the glider located at $\boldsymbol{r}_{cg} = [x_{cg}, y_{cg}, z_{cg}]^T$. If we recall from section 2.2 the location of CG is determined by the distribution of masses and their correlating position vector. The buoyant force $\boldsymbol{f}_b^n \in \mathbb{R}^3$ acts off the center of buoyancy CB which is aligned with the vehicle origin.

For a submerged underwater object the weight W and buoyancy force B is derived following [33, 34, 36, 39]

$$B = \rho g \Delta, \quad W = m_t g \tag{2.29}$$

Where ρ is the density of water, Δ is the displaced volume of the submerged object and g is the acceleration of gravity.

Remark. *The displaced fluid volume Δ is sometimes not prior knowledge. Hence, we can alternatively model the buoyancy by the displaced fluid mass $\Delta_m = m_t - m_b$, which have been proposed in previous work on modelling glider dynamics, see [42, 60, 113].*

The weight W and buoyancy W are compensatory forces, meaning that the difference between the two scalars determines if the vehicle will float, sink or be neutral buoyant. If $W < B$ the buoyant force is larger than the weight and the object tend to float. In the opposite scenario, When $W > B$, the weight is larger than the buoyancy and it will tend to sink. An equilibrium occurs when $W = B$, which is referred to as neutral buoyancy. A common practice in glider design is to create a slightly positive buoyant vehicle so that it will use only a small volume displacement in order to sink/dive [41, 60].

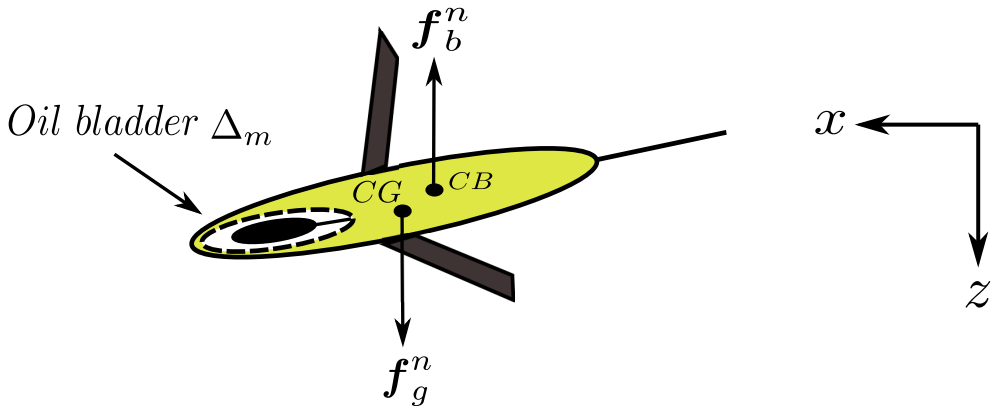

Figure 2.3: Restoring forces

Remark. *We have previously defined the center of buoyancy CB as a fixed location. However, when the external bladder (figure 2.3) is expanded or deflated, a very small volume change occurs, which in theory changes the location of CB. Yet, due to minor changes, the deviation in CB is neglected.*

The vector representation of the weight W and the buoyancy B can be derived in the following manner

$$\boldsymbol{f}_g^n = \begin{bmatrix} 0 \\ 0 \\ W \end{bmatrix}, \quad \boldsymbol{f}_b^n = - \begin{bmatrix} 0 \\ 0 \\ B \end{bmatrix} \tag{2.30}$$

According to [36] we can generalize the restoring forces in the body frame $\{b\}$ as

$$\boldsymbol{g}(\boldsymbol{\eta}) = - \begin{bmatrix} \boldsymbol{R}_b^n(\boldsymbol{\Theta})^{-1}(\boldsymbol{f}_g^n + \boldsymbol{f}_b^n) \\ \\ \boldsymbol{S}(\boldsymbol{r}_{cg}) \cdot \boldsymbol{R}_b^n(\boldsymbol{\Theta})^{-1} \boldsymbol{f}_g^n + \boldsymbol{S}(\boldsymbol{r}_{cb}) \cdot \boldsymbol{R}_b^n(\boldsymbol{\Theta})^{-1} \boldsymbol{f}_b^n \end{bmatrix} \tag{2.31}$$

We recall from the previous page that the vector representing center of buoyancy $\boldsymbol{r}_{cb}$ coincides with the origin of the vehicle so that $\boldsymbol{r}_{cb} = [0, 0, 0]^T$. Accordingly, we can rewrite the generalized forces by removing the terms related to the $\boldsymbol{r}_{cb}$ vector. Then

the generalized restoring forces are simplified by

$$\boldsymbol{g}(\boldsymbol{\eta}) = \begin{bmatrix} (W-B)\,sin(\theta) \\ -(W-B)\,cos(\theta)\,sin(\phi) \\ -(W-B)\,cos(\theta)\,cos(\phi) \\ -y_{cg}W\,cos(\theta)\,cos(\phi) \;+\; z_{cg}W\,cos(\theta)\,sin(\phi) \\ z_{cg}W\,sin(\theta) \;+\; x_{cg}W\,cos(\theta)\,cos(\phi) \\ -x_{cg}Wcos(\theta)sin(\phi) \;+\; y_{cg}Wsin(\theta) \end{bmatrix} \tag{2.32}$$

2.5 Hydrodynamics

In this section we introduce the hydrodynamic effects in fixed-wing underwater gliders. The hydrodynamics are divided into two parts - Firstly, we investigate the hydrodynamic forces and moments which act on the glider body and airfoils of the fixed-wings. Secondly, added mass effects are described, which occur as the glider *pushes* away water when moving trough the water column.

Common practises in hydrodynamics is to represent forces and moments in the flow frame as presented in many works [34, 36, 41, 113]. The flow frame $\{f\}$, also referred to as the *wind-frame* in airborne vehicles, originates from traditional aerodynamics theory and have been extended to fixed-wing gliders in [41, 42, 60].

The relationship between the body-frame $\{b\}$ and flow-frame $\{f\}$ is determined by an rotation of the angle-of-attack (AOA) denoted α and the sideslip angle (SSA) denoted β. Following [41] the angle of attack and sideslip angle are derived by

$$\alpha = tan^{-1}(\frac{u_r}{w_r}), \quad \beta = sin^{-1}(\frac{v_r}{U}) \tag{2.33}$$

where $U = \sqrt{u_r^2 + v_r^2 + w_r^2}$. The rotation matrix from the body frame to the flow frame can then be given by [36, 41, 113] as

$$\boldsymbol{R}_b^f(-\beta, \alpha) = \begin{bmatrix} cos(\beta)cos(\alpha) & sin(\beta) & cos(\beta)sin(\alpha) \\ -sin(\beta)cos(\alpha) & cos(\beta) & -sin(\beta)sin(\alpha) \\ -sin(\alpha) & 0 & cos(\alpha) \end{bmatrix} \tag{2.34}$$

2.5.1 Hydrodynamic Damping

Damping of an submerged underwater glider occurs due to vortex shredding and skin friction effects [33, 36]. For fixed-wing gliders, the hydrodynamic transnational forces are equivalent to aerodynamic forces such as drag, sideforce and lift [41]. As gliders operate at low speed, we can assume that the damping is linear and diagonal. The hydrodynamic forces and moments can be defined by *Morrison's* equation [36]. Given a velocity u, a cross-sectional area under water A, the water density ρ and the drag coefficient C_d the viscous damping force is derived as

$$F(u) = -\frac{1}{2}\rho C_D(R_n) A \boldsymbol{v}^2 \tag{2.35}$$

Where C_D is a function of the *Reynolds numbers* given by $R_n = \frac{uD}{v}$ where D is the length of the body and v is the kinematic viscosity coefficient [36]. Consequently, the hydrodynamic forces and moments can be derived by using eq. 2.35 such that

$$\begin{bmatrix} D_f^b \\ SF_f^b \\ L_f^b \\ K_f^b \\ M_f^b \\ N_f^b \end{bmatrix} = \begin{bmatrix} -\frac{1}{2}\rho C_D(\alpha, \beta, R_n) A \boldsymbol{v}^2 \\ \frac{1}{2}\rho C_{SF}(\alpha, \beta, R_n) A \boldsymbol{v}^2 \\ -\frac{1}{2}\rho C_L(\alpha, \beta, R_n) A \boldsymbol{v}^2 \\ \frac{1}{2}\rho C_K(\alpha, \beta, R_n) A \boldsymbol{v}^2 \\ \frac{1}{2}\rho C_M(\alpha, \beta, R_n) A \boldsymbol{v}^2 \\ \frac{1}{2}\rho C_N(\alpha, \beta, R_n) A \boldsymbol{v}^2 \end{bmatrix} + \begin{bmatrix} 0 \\ 0 \\ 0 \\ C_p p \\ C_q q \\ C_r r \end{bmatrix} \tag{2.36}$$

Where C_p, C_q, C_r are the coefficients for the rotational damping [41, 113]. Following [41, 113] the hydrodynamic forces and moments can be derived in a quasi-state model by

$$\begin{aligned} D_f^b &= (K_{D_0} + K_D \cdot \alpha^2) \cdot U^2 \\ L_f^b &= (K_{L_0} + K_\alpha \cdot \alpha) \cdot U^2 \\ SF_f^b &= K_\beta \cdot \beta \cdot \upsilon^2 \\ K_f^b &= (K_{MR} \cdot \beta + K_p \cdot p) \cdot U^2 \\ M_f^b &= (K_{M0} + K_M \cdot \alpha + K_q \cdot q) \cdot U^2 \\ N_f^b &= (K_{MY} \cdot \beta + K_r \cdot r) \cdot U^2 \end{aligned} \tag{2.37}$$

The hydrodynamic damping terms from eq. 2.37 are defined in the flow frame $\{f\}$, and must be rotated to the body frame by the rotation matrix $\boldsymbol{R}_b^f(-\beta, \alpha)$. Consider the hydrodynamic forces denoted by the vector $\boldsymbol{F}_f^b = [D_f^b, SF_f^b, L_f^b]^T$ and the moments denoted by $\boldsymbol{M}_f^b = [K_f^b, M_f^b, N_f^b]^T$. Using the rotation matrix we can rotate the vectors from the flow frame to the body frame, yielding

$$\begin{aligned} \boldsymbol{F}_b^f &= \boldsymbol{F}_f^b \cdot \boldsymbol{R}(-\beta, \alpha) \\ \boldsymbol{M}_b^f &= \boldsymbol{M}_f^b \cdot \boldsymbol{R}(-\beta, \alpha) \end{aligned} \tag{2.38}$$

where $\boldsymbol{F}_b^f$ and $\boldsymbol{M}_b^f \in \mathbb{R}^3$. Following the matrix notation of the vectorial marine craft dynamics, the hydrodynamic damping can be derived in the body-fixed frame as

$$\boldsymbol{D}(\boldsymbol{\nu}_r) = \begin{bmatrix} diag(\boldsymbol{F}_b^f) & \boldsymbol{0}_{3\times3} \\ \boldsymbol{0}_{3\times3} & diag(\boldsymbol{M}_b^f) \end{bmatrix} = \begin{bmatrix} D_b^f & 0 & 0 & 0 & 0 & 0 \\ 0 & SF_b^f & 0 & 0 & 0 & 0 \\ 0 & 0 & L_b^f & 0 & 0 & 0 \\ 0 & 0 & 0 & K_b^f & 0 & 0 \\ 0 & 0 & 0 & 0 & M_b^f & 0 \\ 0 & 0 & 0 & 0 & 0 & N_b^f \end{bmatrix} \tag{2.39}$$

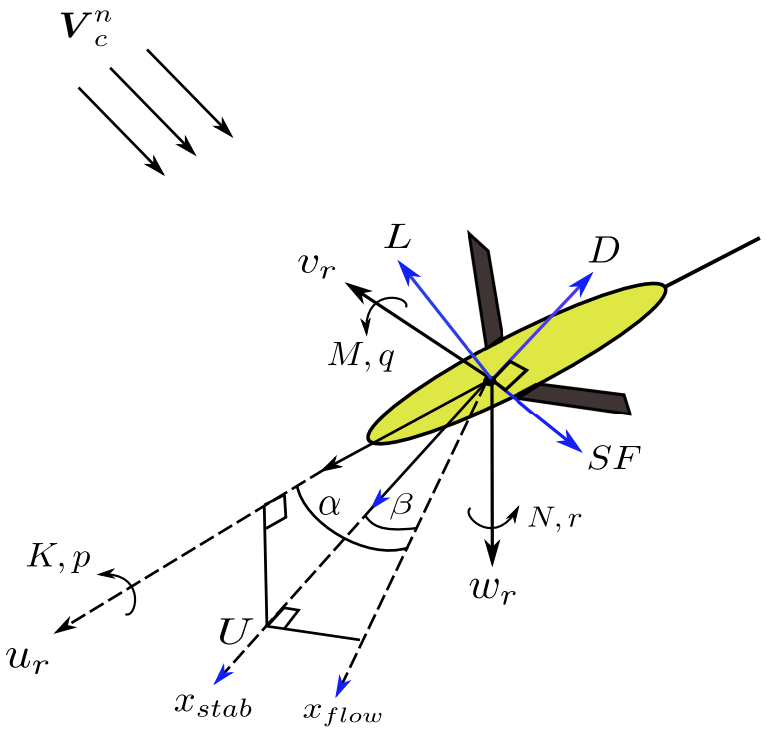

Figure 2.4: Glider hydrodynamics

Figure 2.4 illustrates the hydrodynamic forces (D,SF,L) and moments (K,M,N) which acts on the glider. x_{stab} (stability) and x_{flow} are the two axes in which we rotate the glider hydrodynamics from the flow frame $\{f\}$ to the body frame $\{b\}$. The rotation matrix $\boldsymbol{R}(-\beta, \alpha)$ consists of two rotations, yielding $\boldsymbol{R}(-\beta, \alpha) = \boldsymbol{R}_{z,-\beta} \cdot \boldsymbol{R}_{y,\alpha}$. Firstly, the flow axis is rotated to by a negative SSA $-\beta$ about the vertical axis (z-axis), which results in a new coordinate system referred to as stability axis (see figure 2.4. Finally, this coordinate system is rotated about the y-axis by the AOA α to get to the body-fixed frame $\{b\}$ [34, 36, 41]

2.5.2 Added Mass

A secondary non-dimensional hydrodynamic force occurs for submerged objects - added mass effects. This occur due to displacement of fluid when the glider travels trough

the water column. As the water and the glider cannot occupy the same space at the same time, the vehicle must *push* the water away in order to move forward. Following [36, 41, 113], the added mass effects for the transnational dynamics are given by

$$\boldsymbol{M}_A = -\begin{bmatrix} X_{\dot{u}} & X_{\dot{v}} & X_{\dot{w}} & X_{\dot{p}} & X_{\dot{q}} & X_{\dot{r}} \\ Y_{\dot{u}} & Y_{\dot{v}} & Y_{\dot{w}} & Y_{\dot{p}} & Y_{\dot{q}} & Y_{\dot{r}} \\ Z_{\dot{u}} & Z_{\dot{v}} & Z_{\dot{w}} & Z_{\dot{p}} & Z_{\dot{q}} & Z_{\dot{r}} \\ K_{\dot{u}} & K_{\dot{v}} & K_{\dot{w}} & K_{\dot{p}} & K_{\dot{q}} & K_{\dot{r}} \\ M_{\dot{u}} & M_{\dot{v}} & M_{\dot{w}} & M_{\dot{p}} & M_{\dot{q}} & M_{\dot{r}} \\ N_{\dot{u}} & N_{\dot{v}} & N_{\dot{w}} & N_{\dot{p}} & N_{\dot{q}} & N_{\dot{r}} \end{bmatrix} \tag{2.40}$$

The added mass matrix $\boldsymbol{M}_A$ in 2.40 is a fully coupled model, and in practice, "over-complicated" for low-speed underwater gliders. *Off-diagonal* terms are very small compared to the diagonal terms. Consequently, as gliders are slow vehicles and spends most of it's time in steady-state glides, the *off-diagonal* terms can be neglected following [36, 42, 60] such that the matrix 2.40 is rewritten with only diagonal terms

$$\boldsymbol{M}_A = -diag[X_{\dot{u}}, Y_{\dot{v}}, Z_{\dot{w}}, K_{\dot{p}}, M_{\dot{q}}, N_{\dot{r}}] \in \mathbb{R}^{6\times 6} \tag{2.41}$$

The matrix $\boldsymbol{M}_A$ represents the added mass effects in transnational motion. We also need to model the added mass effects for rotational motions. The rotational added mass effects for the coriolis and centripetal matrix $\boldsymbol{C}_A(\boldsymbol{\nu}_r)$ is parameterized with skew-symmetric properties yielding: $\boldsymbol{C}_A(\boldsymbol{\nu}_r) = -\boldsymbol{C}_A^T(\boldsymbol{\nu}_r)$, where $\boldsymbol{\nu}_r = [\boldsymbol{\upsilon}, \boldsymbol{\omega}]^T \in \mathbb{R}^6$ [33,34,36], which yields

$$\boldsymbol{C}_A(\boldsymbol{\nu}_r) = \begin{bmatrix} \boldsymbol{0}_{3\times 3} & -\boldsymbol{S}(\boldsymbol{A}_{11}\cdot\boldsymbol{\upsilon} + \boldsymbol{A}_{12}\cdot\boldsymbol{\omega}) \\ -\boldsymbol{S}(\boldsymbol{A}_{11}\cdot\boldsymbol{\upsilon} + \boldsymbol{A}_{12}\cdot\boldsymbol{\omega}) & -\boldsymbol{S}(\boldsymbol{A}_{21}\cdot\boldsymbol{\upsilon} + \boldsymbol{A}_{22}\cdot\boldsymbol{\omega}) \end{bmatrix} \tag{2.42}$$

Where $\boldsymbol{A}_{ij} \in \mathbb{R}^{3\times3}$ is the quadrants of the added mass matrix in eq. 2.40.

$$\boldsymbol{M}_A = \begin{bmatrix} \boldsymbol{A}_{11} & \boldsymbol{A}_{12} \\ \boldsymbol{A}_{21} & \boldsymbol{A}_{22} \end{bmatrix} \tag{2.43}$$

Expanding the matrix 2.42 results in

$$\boldsymbol{C}_A(\boldsymbol{\nu}) = \begin{bmatrix} 0 & 0 & 0 & 0 & -Z_{\dot{w}}w & Y_{\dot{v}}v \\ 0 & 0 & 0 & Z_{\dot{w}}w & 0 & -X_{\dot{u}}u \\ 0 & 0 & 0 & -Y_{\dot{v}}v & X_{\dot{u}}u & 0 \\ 0 & -Z_{\dot{w}}w & Y_{\dot{v}}v & 0 & -N_{\dot{r}}r & M_{\dot{q}}q \\ Z_{\dot{w}}w & 0 & -X_{\dot{u}}u & N_{\dot{r}}r & 0 & -K_{\dot{p}}p \\ -Y_{\dot{v}}v & X_{\dot{u}}u & 0 & M_{\dot{q}}q & K_{\dot{p}}p & 0 \end{bmatrix} \tag{2.44}$$

2.6 Simulations

As the OASYS glider lack empirical testing of the hydrodynamic properties of the vehicle, the parameters of a similar glider, the Seawing glider [82, 109, 110, 113] is exploited to validate the numerical model. The Seawing glider is a fixed-winged underwater glider that shares similarities of the OASYS glider in terms of a cylindrical moving mass system and a variable buoyancy system based on hydraulic oil. The mechanical and hydrodynamic parameters of the Seawing glider is found in Appendix A.

2.6.1 Actuator models

As previously mentioned, underwater gliders are driven by buoyancy and internal moving mass actuators. They are able to adjust the net buoyancy by pumping an oil mass m_b between an internal reservoir and external bladder. The variable buoyancy system (VBS) for the OASYS glider is driven by a miniaturized pump and a valve to distribute the oil. The second actuator is the moving mass system, where a battery-pack is translated and rotated inside the glider housing. The mass m_p is attached to a rail system consisting of threaded screws. Common for the two actuating systems is that they are driven by rotary motors e.g., brush less DC/stepper motors [28, 92]. We let $\boldsymbol{u} = [\omega_x, \omega_\gamma, \omega_{mb}]^T$ be the control input vector consisting of the motor revelations of the moving mass system and VBS system respectively, which yields the following assumptions:

Assumption 8. *The three actuators $\omega_x, \omega_\gamma, \omega_{mb}$ and their outputs are considered decoupled.*

Assumption 9. *The transnational ω_x and rotational ω_γ moving mass actuators can be activated simultaneously.*

Remark. *To simultaneously translate and rotate the internal moving mass, there must be two motors that control each motion. Accordingly, the moving mass system is considered a 2DOF actuator.*

The actuator components of the OASYS glider are showcased in the following figure, consisting of the VBS system and internal moving mass system

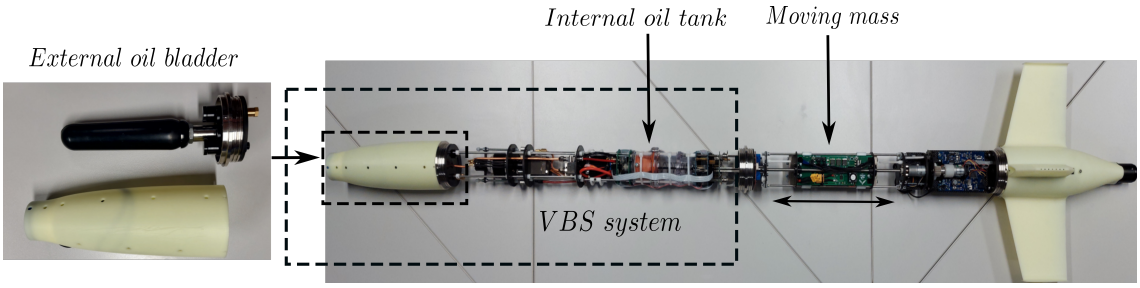

Figure 2.5: Internal components of the OASYS glider [28]

From a control perspective, the moving mass system is used for pitch and heading control, while the VBS system is for buoyancy control. Buoyancy control is often achieved trough simple bang-bang/on-off controllers and is only activated during transition between upward and downward glides. Heading and pitch control are more active as the internal mass actuator have faster response compared to the VBS system. This control system is also a little more advanced where the control laws are cascaded with a battery position controller. Accordingly, the output of the pitch and heading controllers (see figure 2.6) are the desired moving mass positions r_{x_d}, r_{x_γ} that are further cascaded with the battery position controller.

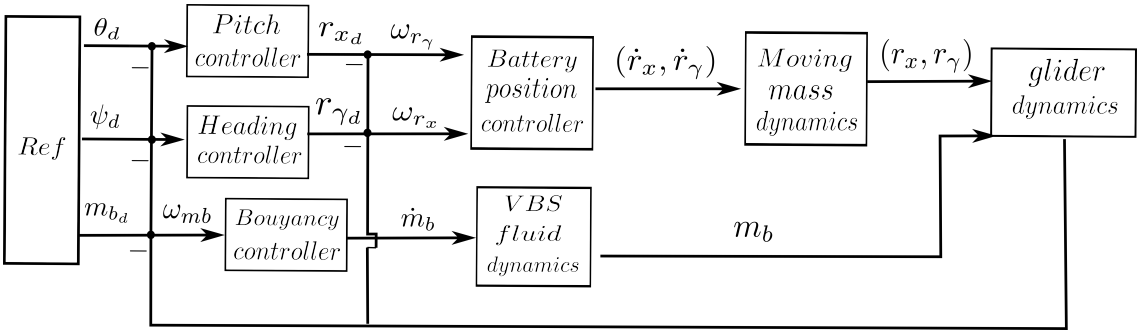

Figure 2.6: Actuators in control loop

Ideally, the VBS and moving mass dynamics should be modelled to improve the quality of the glider dynamics. However, modelling coupled moving mass systems and fluid dynamics for the VBS requires complex and cumbersome mathematical models. As the glider model will be used for simulation purposes and not to derive model-based control laws or observers, a simplified model of the actuator dynamics is suggested. Rate-limiters are proposed to reflect the actuator dynamics as both systems introduce time-delays.

Assumption 10. *The VBS system pumps oil with a constant flow rate -* $\dot{m}_b = \kappa$

Assumption 11. *The velocities of the translating and rotating mass actuators are constant -* $\dot{r}_x = \kappa$, $\dot{r}_\gamma = \kappa$

Following [67] the rate-limiters of the two actuators can be defined. The translational moving mass is used as an example, which have the rate

$$\dot{r}_x(k) = \frac{\omega_{r_x}(k) - r_x(k-1)}{t(k) - t(k-1)} \tag{2.45}$$

where $t(k)$ is the time incremented by k. Next we define rising and falling slew rate parameters denoted by ϵ_r, ϵ_f. If the rate satisfies $\dot{r}_x > \epsilon_r$, the output is limited by the rise slew rate ϵ_r, such that

$$r_x(k) = \Delta k + \epsilon_r + r_x(k-1) \tag{2.46}$$

If the rate is lower than the falling slew rate ϵ_f, the output $r_x(k)$ yields

$$r_x(k) = \Delta k + \epsilon_f + r_x(k-1) \tag{2.47}$$

Remark. *Note that the simplified actuator models for the moving mass system neglect the battery position controller as this is only necessary for actual hardware.*

2.6.2 Open-Loop simulations

We start by simulating the glider dynamics using open-loop control actions. The first simulation illustrates the repeating undulating trajectory by adjusting the net buoyancy m_b and translational moving mass position r_x. This is considered a *wings-levelled* flight where the heading ψ is fixed.

The following initial state vectors were introduced in the simulation: $\boldsymbol{\nu}_o = [0, 0, 0, 0, 0, 0]^T$ and $\boldsymbol{\eta}_0 = [0, 0, 0, 0, 0, 0]^T$. As presented in figure 2.7, three simulations were conducted with different ocean current headings - $\beta_c = 0\, rad, \beta_c = \pi/2\, rad$, and $\beta_c = -\pi/2\, rad$. An ocean current magnitude of $\boldsymbol{V}_c^n = \sqrt{u_c^n + v_c^n} = 0.1$ m/s was recurring for all three simulation cases.

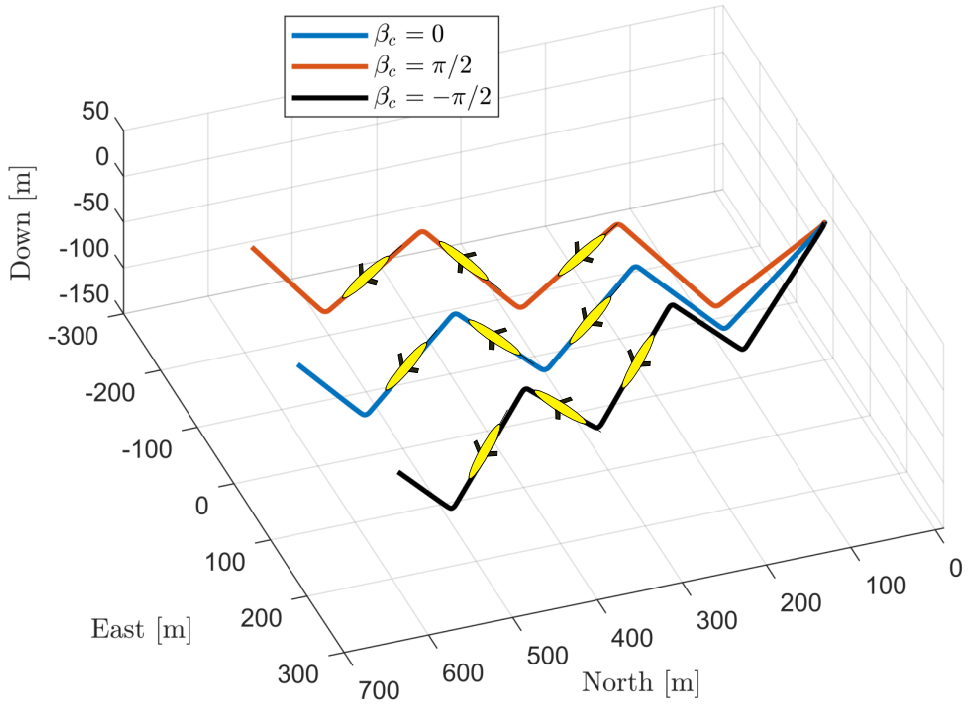

Figure 2.7: Open-loop simulation - case 1

The open loop control inputs are presented in figure 2.8, where the net buoyancy and moving mass position are adjusted between upward and downward glides. When descending, the net buoyancy mass is 0.3 kg and -0.3 kg when rising. The transition between the two states introduces an instant drop in the surge velocity as seen at the top right plot. The moving mass control inputs are activated simultaneously with the buoyancy displacement. For downward glides, the moving mass is located in the front and moved to the back of the vehicle when rising.

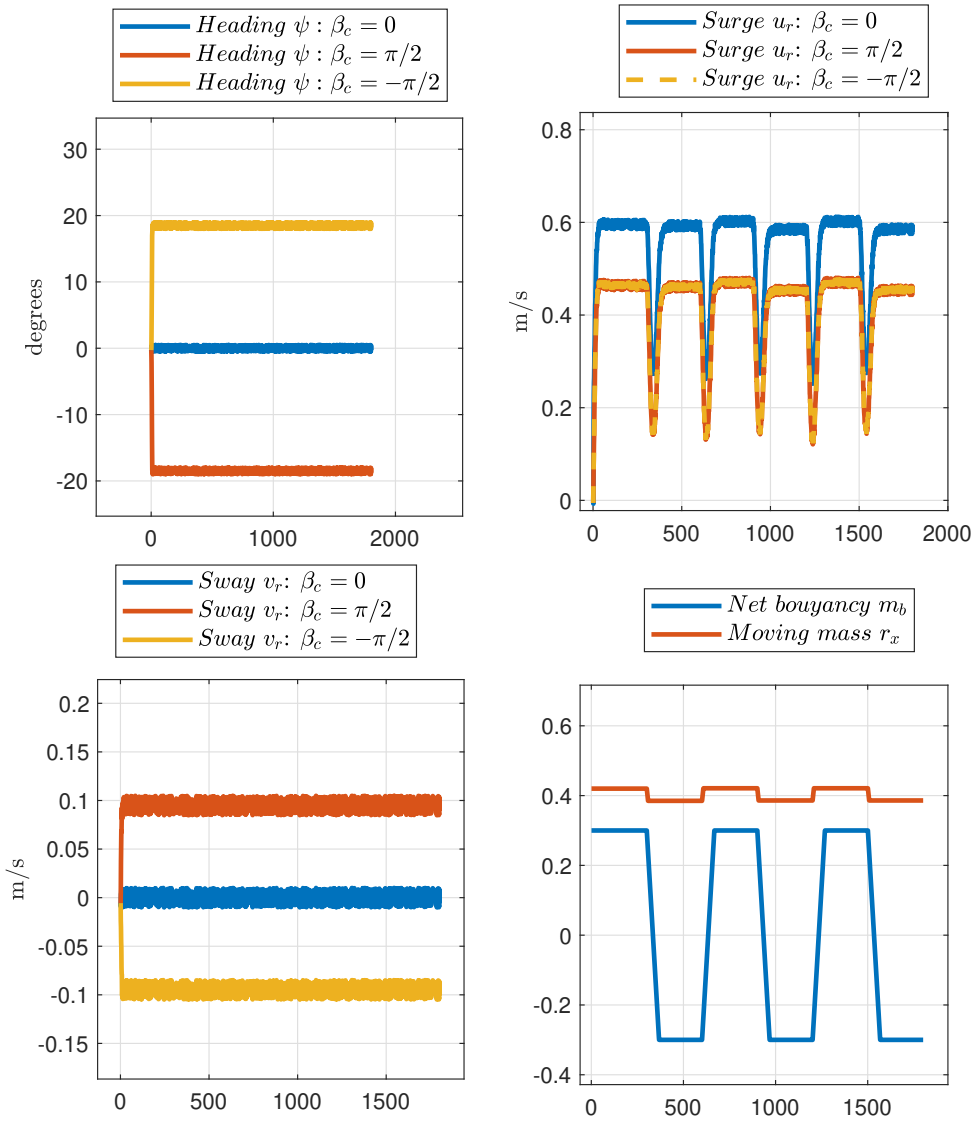

Figure 2.8: Simulation parameters - Case 1

The second simulation experiment is the characteristic *vertical spiral*. This happens when the rotating mass is shifted from it's origin, introducing a constant angular velocity r about the yaw axis. When the glider body is rolled, the wings are no longer aligned in the vertical axes, making the vehicle enter a vertical spiral. The initial state vectors in this simulation are the same as with case 1, where: $\boldsymbol{\nu}_o = [0, 0, 0, 0, 0, 0]^T$ and $\boldsymbol{\eta}_0 = [0, 0, 0, 0, 0, 0]^T$. Instead of changing the ocean current vector β_c, we alter the ocean current magnitudes for the three simulation cases - Accordingly, three different scenarios were proposed with the following magnitudes: $\boldsymbol{V}_c^n = 0.1$ m/s, $\boldsymbol{V}_c^n = 0.2$ m/s, and $\boldsymbol{V}_c^n = 0.3$ m/s. During these experiments the ocean current direction was set to zero - $\beta_c = 0$.

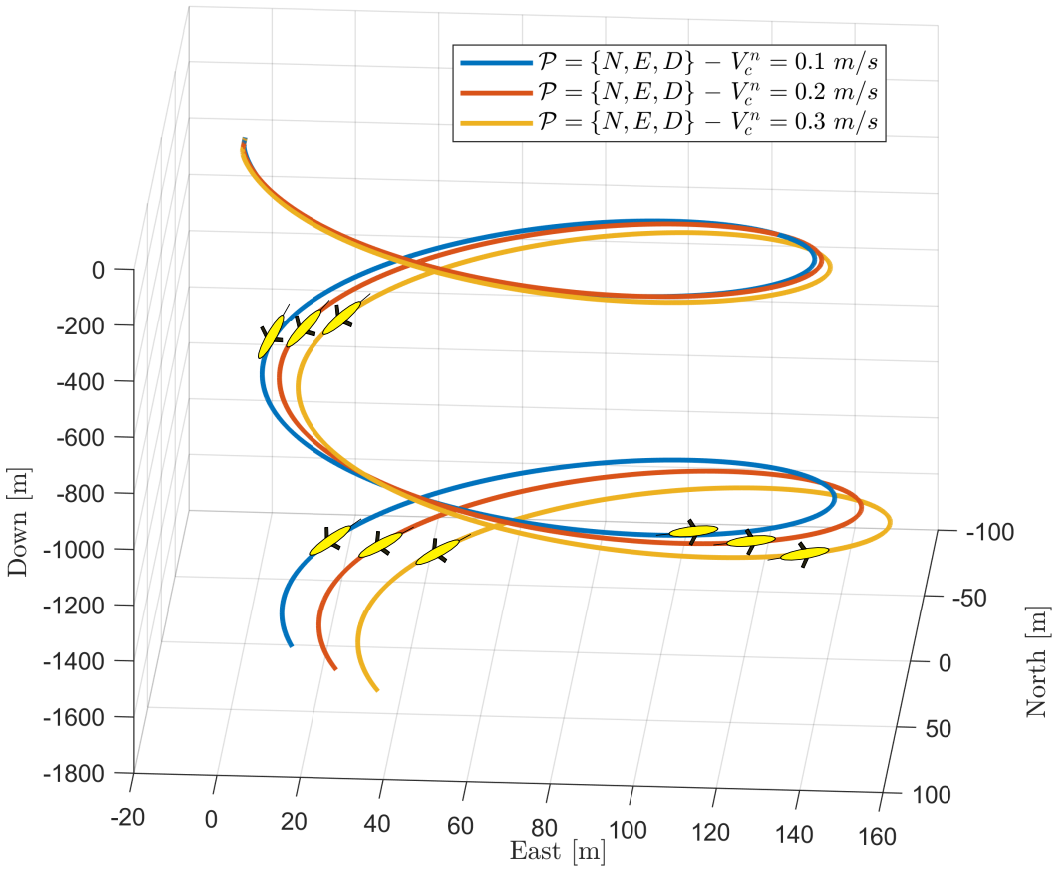

Figure 2.9: Simulation case 2 - vertical spiral

Conversely to the first experiment, the control inputs are only initialized at the beginnings and remained constant throughout the simulation experiments. The rotating mass angle was set to 2 rad (resulting in a left-turn), while the net buoyancy mass was initialized to $m_b = 0.3$ kg where the vehicle is negatively buoyant (downward glide). Depending on the ocean current magnitude $\boldsymbol{V}_c^n$, the surge and sway velocities in figure 2.10 have sinusoidal responses due to the circular motions.

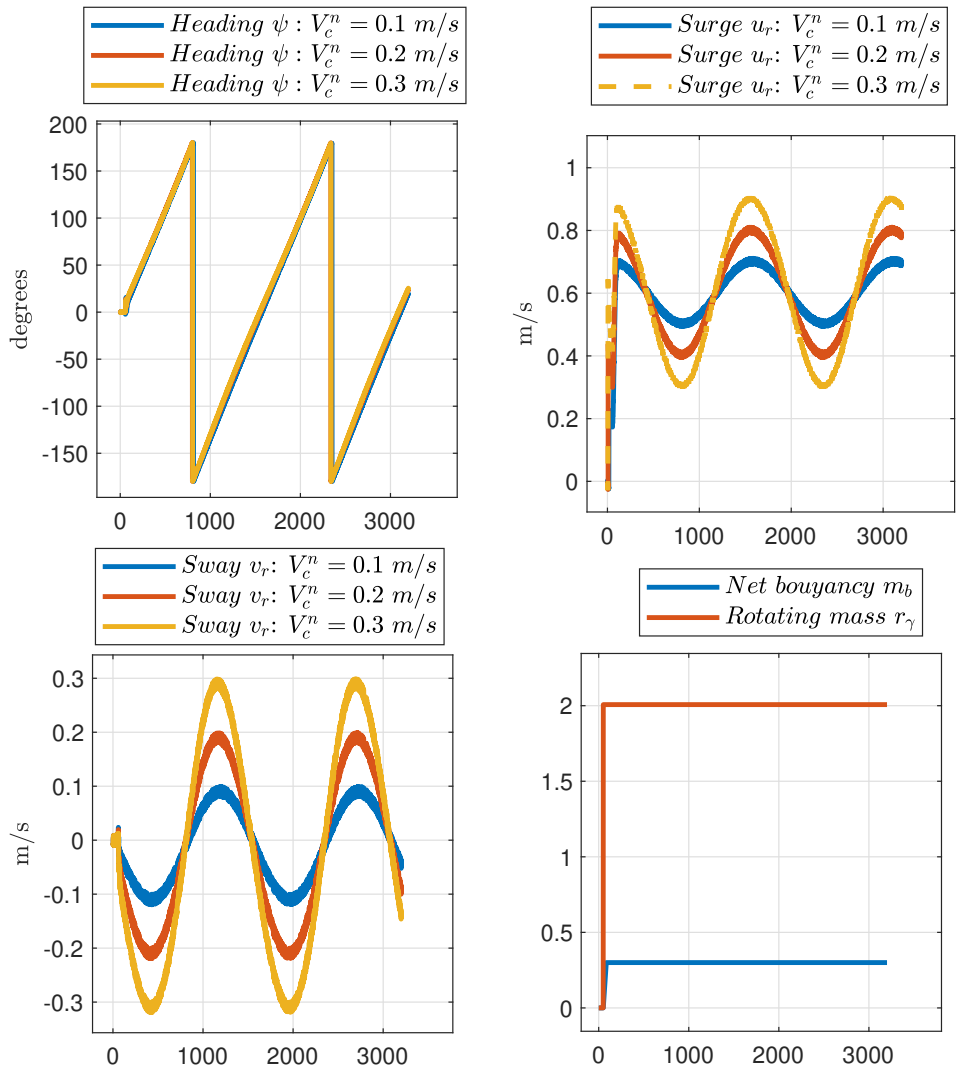

Figure 2.10: simulation parameters - case 2

2.7 Control

This section details low-level control of underwater gliders. In practice, gliders control their net buoyancy mass m_p and pitch θ and heading ψ angles. The attitude and heading is controlled using the internal moving mass system, which is translated and rotated along a rail inside the housing using rotary motors connected to trapezidoal screws. The bouyancy control, consists of pumping oil between an internal reservoir and an external bladder. The oil is pumped using a geared motor [28].

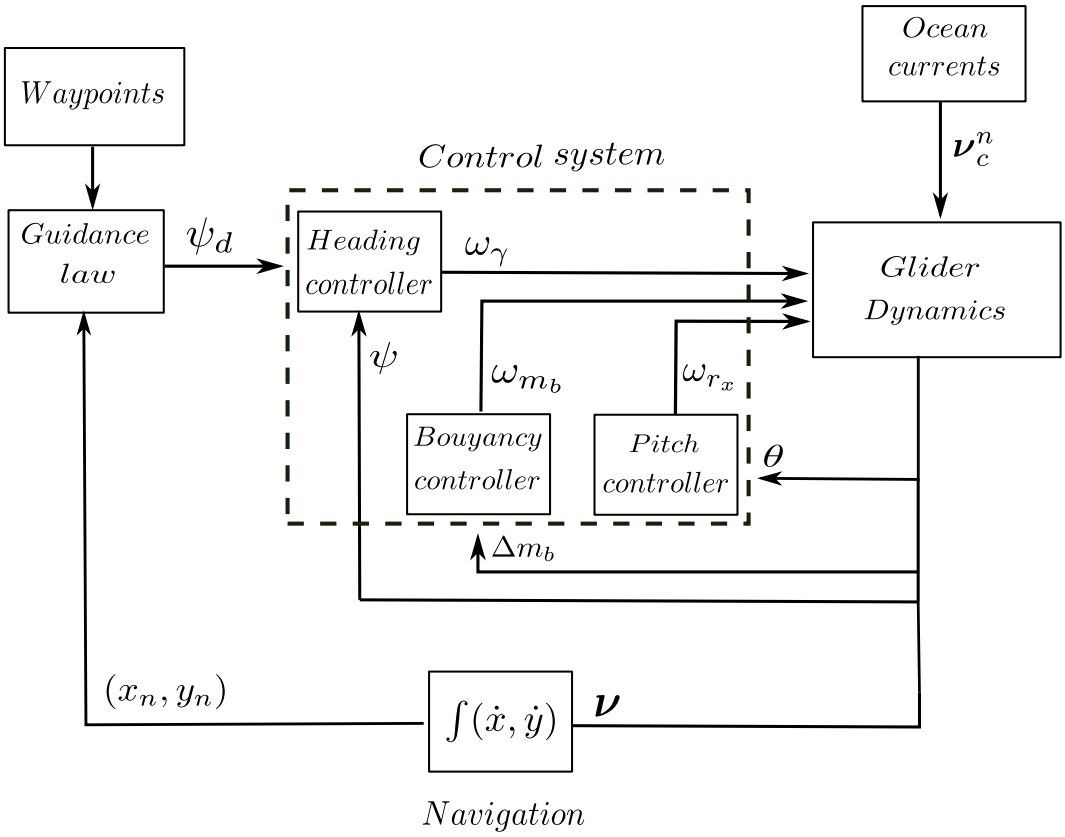

Figure 2.11: Control - Block-diagram

Given the latter description, we want to relax the following conditions:

$$\begin{aligned} &\lim_{t\to\infty}(m_{b_d} - m_b) = 0 \\ &\lim_{t\to\infty}(\psi - \psi_d) = 0, \;\; \psi \in (-\pi, \pi) \\ &\lim_{t\to\infty}(\theta - \theta_d) = 0, \;\; \theta \in (-\pi/4, \pi/4) \end{aligned} \tag{2.48}$$

Remark. *The pitch angle is configured for* $\theta \in (-\pi/4, \pi/4)$ *rad due to practical limitations. Optimized pitching angles are documented in ranges from* $20 - 30$ *degrees* $(0.35 - 0.5\, rad)$ *[31, 61, 100, 104, 113] depending on the glider shape and design.*

For the buoyancy control, the open-loop inputs presented in the previous section are reused. In practice, however, this is achieved by simple bang-bang/on-off controllers, where the displaced buoyancy mass (oil) Δm_b of the internal tank is used as feedback.

2.7.1 Plant Identification for Pitch and Heading Control

In this section we propose a system identification scheme for the kinematic plants of the vehicle. This will further be used to tune linear PID controllers for the underwater glider using autotuner tools in the MATLAB control system toolbox [69]. The proposed system identification model is a nonlinear auto-regressive exogenous model (NARX). This type of system identification uses regression models of past data, typically in form of past inputs and outputs from the nonlinear dynamic system.

Nonlinear Auto-Regressive Exogenous (NARX) System identification

The linear SISO (Single-Input-Single-Output) linear auto regressive exogenous model is derived Following [7, 58, 59] as

$$\begin{aligned} &y(t) + a_1 y(t-1) + a_2(t-2) + \ldots a_{na}(t-na) = b_1 u(t) + b_2 u(t-1) + \ldots \\ &+ b_{nb}(t - nb + 1) + e(t) \end{aligned} \tag{2.49}$$

Where y is the output, u is the input and e is the noise. Accordingly, na and nb represents the number of past outputs and inputs respectively, these are often referred to as regressors. We can rewrite equation 2.49 so that the output $y(t)$ is left alone on the left side of the equation, yielding

$$\begin{aligned} y(t) =&[-a_1, -a_2, \dots, -a_n, b_1, b_2, \dots, b_{nb}] \cdot [y(t-1), y(t-2), \dots, \\ & y(t-na), u(t), u(t-1), \dots, u(t-nb+1)]^T \end{aligned} \tag{2.50}$$

The structure of the linear ARX model consists of weighted sums of past output values and current and past input values to predict the current output $y(t)$. The nonlinear ARX model is derived in the following manner

$$y(t) = \boldsymbol{F}(y(t-1), y(t-2), y(t-3), \dots, u(t), u(t-1), \dots) \tag{2.51}$$

Where $\boldsymbol{F}(x)$ is the nonlinear function that consists of a linear and nonlinear function in parallel. and x consists is the regressors for the output and input variables. The function $\boldsymbol{F}(x)$ can be derived as

$$\boldsymbol{F}(x) = \boldsymbol{L}^T(x-r) + d + g(\boldsymbol{Q}(x-r) \tag{2.52}$$

As real datasets from the glider is not available, we revisit the simulation of the nonlinear glider dynamics to generate "fictitious" datasets for heading and pitch system identification. We can rewrite eq. 2.51 to represent the heading and pitch plants as two decoupled SISO plants. Accordingly, the heading/yaw plant have ψ as an output and the rotating mass positionr_γ as input. The pitch plant consists of the output θ and the input r_x which is the translational position of the moving mass. Accordingly, we introduce the two SISO plants in the following form

$$\begin{aligned} \psi(t) &= \boldsymbol{F}(\psi(t-1), \psi(t-2), \dots, \psi(t-na), \dots, r_\gamma(t), r_\gamma(t-1), \dots, r_\gamma(t-nb)) \\ \theta(t) &= \boldsymbol{F}(\theta(t-1), \psi(t-2), \dots, \theta(t-na), \dots, r_x(t), r_x(t-1), \dots, r_x(t-nb)) \end{aligned} \tag{2.53}$$

2.7.2 Heading and Pitch control

Control in underwater gliders relate to controlling the heading/yaw and pitch angle of the vehicle induced by the internal moving mass system. In practice, glider dynamics is considered linear due to its slow cruising speeds and symmetric properties. Hence, linear controllers such as PID have been proposed in various research [31,60,61,76,89,112]. PID controllers are extended to the simulated glider in this thesis.

Given a control error $e = (y_{ref} - y)$ the PID control law is derived as

$$u(k) = k_p \cdot e(k) + k_i \int_0^t e(k)\, dt + k_d \cdot \dot{e}(k) \tag{2.54}$$

where $\{k_p, k_i, k_d\}$ are tuning parameters. In this work a closed-loop autotuner in MATLAB [68] is used to determine the control parameters that satisfy stable and transient behaviour. The control output in figure 2.12 $u + \Delta u$ is a sine signal with a desired ampitude that is feed into the NARX control plants in order to tune the PID control parameters.

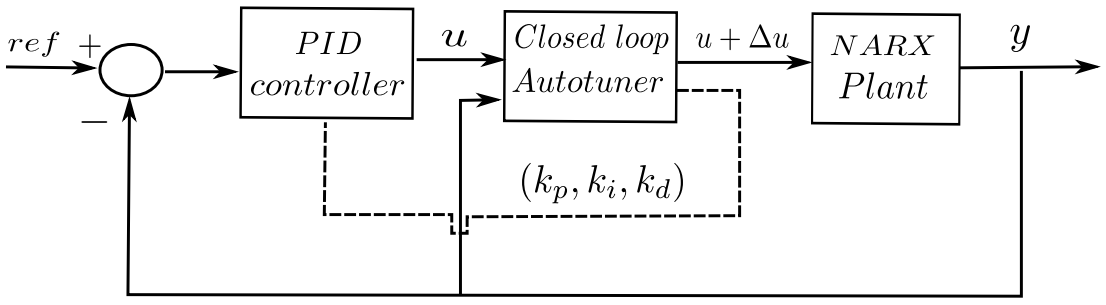

Figure 2.12: PID autotune loop

2.7.3 Pitch control

Three different controllers are proposed - PI, PID, and PD. The tuning parameters $\{k_p, k_i, k_d\}$ where obtained for each controller. After tuning the PID controllers using the NARX plants, we implement the tuning parameters into the nonlinear simulation framework.

Gains	PI controller	PID controller	PD controller
P-term k_{p_θ}	-0.1	-0.15	-0.14
I-term k_{i_θ}	-0.01	-0.03	0
D-term k_{d_θ}	0	-0.08	-0.03

Table 2.2: PID tuning - Pitch control

The parameters from table 2.2 are further compared in the glider simulation as presented in the following figure. The simulation considers a combined upward and downward glide where the net buoyancy m_b is altered using open loop control inputs. The step responses for the pitch controllers are presented in figure 2.13:

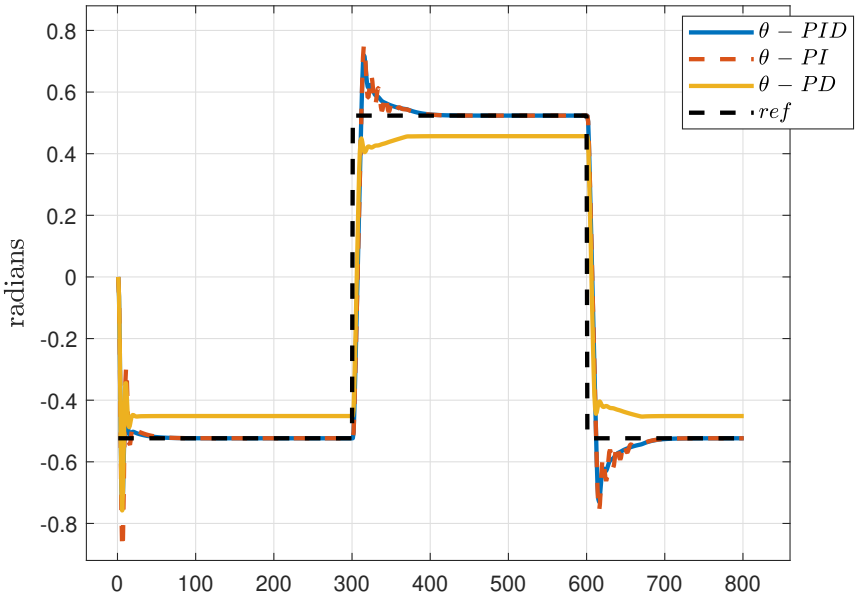

Figure 2.13: Comparing PID,PI,PD controllers

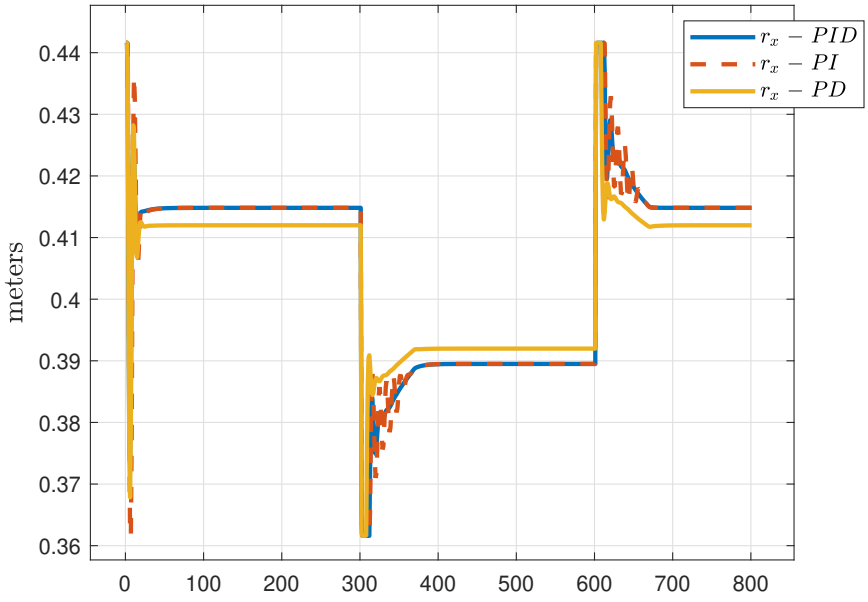

Figure 2.14: Moving mass control actions - r_x

The control input r_x for pitch control is presented in fig. 2.14 for the different PI,PID, and PD controllers. We observe that the position of the moving mass is located forward in the glider $r_x \in \{0.4, 0, 45\}$ m for downward glides, while position in the back $r_x \in \{0.35, 0, 4\}$ during upward glides. In transition between upward and downward glides, the speed of the vehicle is reduced as the buoyancy of the vehicle is changed from negative to positive. Accordingly, this will impact the control moments made by the internal moving mass such that the rise time of the pitch controller will be longer than in nominal speeds.

2.7.4 Heading control

In this section we investigate heading control where the internal mass actuator is rotated to create a yaw moment. We follow the same tuning procedure as with pitch control by comparing PI,PID, and PD controllers. Note - the autotuner did not provide transient tuning parameters for the control plant, hence the the terms in table 2.3 was manually tuned based on the initial autotuning results.

Gains	PI controller	PID controller	PD controller
P-term k_{p_θ}	7.43	8.32	8.87
I-term k_{i_θ}	0.21	0.56	0
D-term k_{d_θ}	0	1.23	0.75

Table 2.3: PID tuning - Heading control

The tuning parameters in table 2.3 are further implemented in the glider simulation. The case study for heading control only considers a downward glide where the vehicle performs left and right turns.

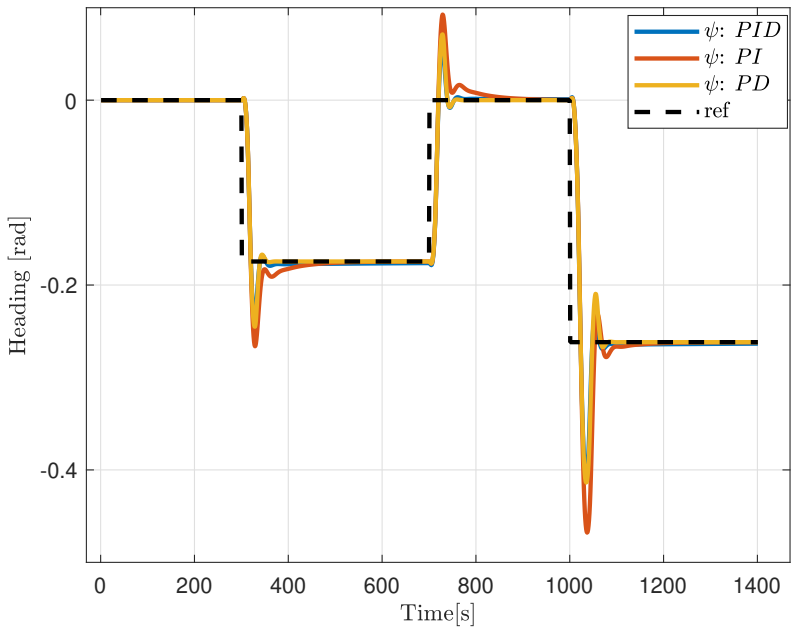

Figure 2.15: Comparing PID,PI,PD controllers - Heading control

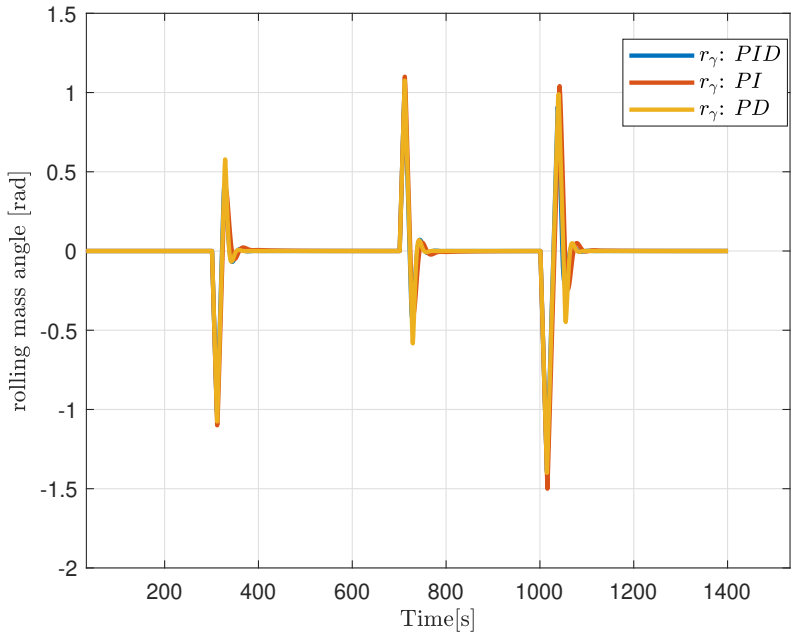

Figure 2.16: Rolling mass control actions - r_x

Figure 2.16 presents the control input r_γ which is the rolling mass servo angle. We observe that the mass is rotated in short periods before returning to it's initial position $r_\gamma = 0$. If the mass was fixed at a non-zero angle, the glider would enter a spiral, accordingly it has to return to a wings-levelled flight to maintain a constant course - the turning maneuver is analogous to how aircraft's make turns. We can also observe that overshoots are compensated by rolling the mass in the opposite direction after returning to $r_\gamma = 0$.

The heading control is performed during a downward glide, hence the rise time is faster as the speed is nominal and not reduced due to buoyancy alternation as with pitch control.

2.8 Conclusion

In this chapter we have derived a 6DOF mathematical model of a buoyancy driven underwater glider, which has been presented in a numerical simulation. Open-loop simulations were conducted with various ocean current disturbances to validate the merit of the proposed glider dynamics. Consequently, control laws for heading and pitch were proposed using linear PID controllers. Nonlinear system identification models were developed to autotune the control plants using MATLABs control system toolbox. We show that the simulation of the glider dynamics reflects documented glider characteristics, such as wings-levelled motions and vertical spirals. Also, the proposed linear PID controllers show transient and converging behaviour for pitch and heading control, which will further be used in path-following applications in chapter 4.

Chapter 3

Navigation: A Deep Learning Approach

This chapter presents a deep/machine learning approach to aid dead-reckoning (DR) navigation. Recurrent Neural Networks (RNN) are proposed to predict the relative velocities of an underwater glider using data from an IMU, pressure sensor, and control inputs. The predictions of the relative velocities are implemented in a dead-reckoning algorithm to approximate north and east positions. The experimental part of this chapter is twofold I) Sea-trial data from a hybrid glider/AUV is firstly presented. Datasets from a series of surveys in Monterey Bay, California (U.S) are used to train and test the RNN velocity observers. II) The second study explore datasets generated by the simulated underwater glider from chapter 2. The proposed neural network approach to DR navigation is compared to the on-board DVL-aided navigation system and ground truth simulated positions.

The theory presented in this chapter was firstly introduced in a preliminary project by the author in [49] and later extended to a conference paper published at the IEEE Oceans conference in 2021.

[83] *Saksvik, I. B., Alcocer, A., Hassani, V. (2021). A Deep Learning Approach To Dead-Reckoning Navigation For Autonomous Underwater Vehicles With Limited Sensor Payloads. Presented at Global Oceans 2021: Porto–San-Diego (pp. 1-10). IEEE.* (Paper is attached in **Appendix D**)

3.1 Introduction

A notorious challenge for gliders is to navigate and *georeference* acquired sensor data as GPS signals propagate poorly in water. Conventional solutions to this issue involve adding acoustic navigational or/and positioning instruments to the glider payload. Due to the good propagation of sound in water, doppler velocity loggers (DVLs) and baseline positioning systems are considered novel solutions to underwater navigation and localization [5, 21, 25, 42, 80, 104]. However, these acoustic instruments are often expensive and consume large amounts of power.

In this chapter we consider a limited glider sensor suite consisting of an IMU sensor and a pressure transducer, where acoustic instruments (e.g., DVL or baseline positioning systems) are partially available to collect experimental training data. Collected *ground truth* measurements from only a few missions are used as a reference in supervised neural network training. The aim for the trained network is to complement DR navigation when DVLs or acoustic positioning systems are inaccessible, for example in glider fleets with budget limitations (OASYS project).

The absence of acoustic navigational and positioning instruments have traditionally been compensated by model-based observers like Extended Kalman Filters (EKFs) in various AUVs/gliders, see [88, 100]. These are derived from the vehicle dynamics to form an estimation model. Unfortunately, model-based observers rely on parameters that are difficult to obtain in practice. As we recall from chapter 2 on modelling glider dynamics, intricate hydrodynamic models are required. Experiments must be carried

out in a towing-tank facility or using expensive CFD (Computational Fluid Dynamics) software to obtain hydrodynamic damping coefficients [88, 113]. If the external geometry of the glider changes, e.g. when making small modifications to payload sections, the coefficients need to be updated.

To avoid deriving complex glider models and conducting time consuming towing-tank or CFD experiments, this chapter presents a data-driven approach to dead-reckoning navigation. Using experimental data from glider missions and simulations, neural networks are trained to learn and generalize relative glider motions. Recurrent neural networks (RNNs) are developed to capture time-delayed glider dynamics. With an input layer composed of onboard sensors (pressure sensor, inertial measurement unit) and control actions, the RNN networks aim to predict relative surge u_r and sway v_r velocities. These are further implemented in a dead-reckoning algorithm to approximate North and East positions while the glider is submerged and not able to receive a GPS fix.

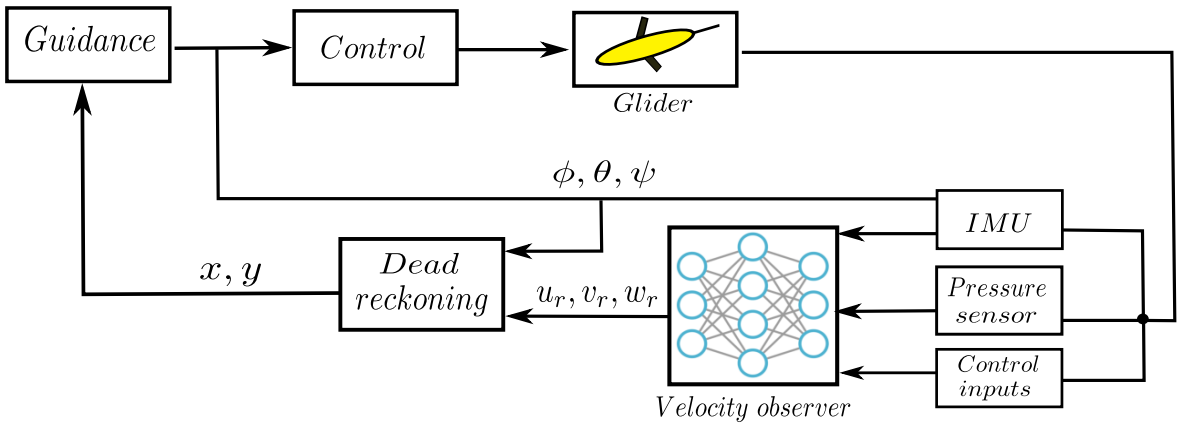

Figure 3.1: Proposed DL approach to dead-reckoning

Figure 3.1 illustrates the GNC (guidance, navigation and control) feedback loop with the proposed neural network velocity observers. The navigation system is cascaded with a guidance system, where the estimated position of the glider is used as feedback in path-following control.

3.1.1 Related work

Several articles have addressed neural network observers to aid navigation for marine vehicles. In [114] a Short-Long-Term-Memory (LSTM) recurrent neural network is proposed to estimate the relative position of an AUV. The LSTM network used data from a pressure sensor, IMU, and an acoustic doppler velocity logger (DVL) to predict the horizontal north and east positions. Training and validation data were collected from a series of surface trajectories while logging GPS locations, which were projected as ground truth measurements. A similar study with the same AUV is presented in Mu *et al.* [74], where a bi-directional LSTM network was proposed. A neural network approach to dead-reckoning navigation of dynamically positioned ships is presented in Skulestad *et al.* [88]. Control actions and commands from vessel thrusters combined with heading measurements were used as input data in a RNN network to aid navigation during GNSS outages. Experiments were conducted in a vessel simulator with time-varying environmental disturbances such as wind forces, sea waves and ocean currents. In Chen *et al.* [57] a neural network is presented to assist navigation during DVL malfunction. A nonlinear autoregressive network with exogenous SINS (Strapdown Inertial Navigation System) inputs was used. The network was tested and validated on a ship with a DVL mounted on the vessel hull to provide training and validation data.

3.2 Dead-Reckoning Navigation

In the absence of GNSS (Global Navigation Satellite Systems), underwater gliders enters a mode called dead-reckoning. Given some initial position (typically a GPS fix before diving), the displacement for each time-step is estimated trough time integration of the transnational velocities [31, 80, 91, 104, 105]. To compute the position of the glider in a local frame of reference, the measured/estimated relative velocities are rotated with respect to the inertial reference frame of the vehicle. We recall from chapter 2 , the

planar position in the inertial frame, given by

$$\dot{\boldsymbol{P}}_b^n = \boldsymbol{R}_b^n(\boldsymbol{\Theta}) \cdot \boldsymbol{\upsilon} + \boldsymbol{V}_c^n \in \mathrm{R}^2 \tag{3.1}$$

Where $\boldsymbol{\Theta} = [\phi, \theta, \psi]^T$ are the attitude and heading of the vehicle provided by an inertial measurement unit (IMU), $\boldsymbol{\upsilon} = [u_r, v_r, w_r]^T$ are the translational velocities, and $\boldsymbol{V}_c^n = [V_x^n, V_y^n, 0]^T$ are the ocean currents in the inertial frame. Equation 3.1 is written in expanded form as

$$\dot{\boldsymbol{P}}_n^b = \begin{bmatrix} \dot{x} \\ \\ \dot{y} \end{bmatrix} = \begin{bmatrix} u_r \cdot c(\psi)c(\theta) + v_r \cdot (c(\psi)s(\theta)s(\phi) - s(\psi)c(\phi)) \\ +w_r \cdot (s(\psi)s(\phi) + c(\psi)c(\phi)s(\theta))) + V_x^n \\ \\ u_r \cdot s(\psi)c(\theta) + v \cdot (c(\psi)c(\phi) + s(\phi)s(\theta)s(\psi)) \\ +w \cdot (s(\theta)s(\psi)c(\phi).c(\psi)s(\phi) + V_y^n \end{bmatrix} \tag{3.2}$$

Remark. *Equation 3.2 contains all three euler angles $\boldsymbol{\Theta} = [\phi, \theta, \psi]^T$ it is assumed that the vehicle have active roll motions. Note that some gliders (e.g, Slocum) are stable in roll and creates yaw moments from an aft rudder. In this case, when $\phi \approx 0$, eq. 3.2 is truncated.*

To obtain the position of the vehicle, we integrate the inertial positions $\dot{\boldsymbol{P}}_b^n$. In discrete form, the numerical integration of eq. 3.1 is given by

$$\boldsymbol{P}_b^n(k+1) = \boldsymbol{P}_b^n(k) + (\boldsymbol{R}_b^n(\boldsymbol{\Theta}) \cdot \boldsymbol{\upsilon}(k+1) + \boldsymbol{V}_c^n) \cdot \Delta k \tag{3.3}$$

where Δk is the sampling time.

3.2.1 Existing DR Strategies In Underwater Gliders

In this section we investigate an existing DR algorithm in a commercial glider (Slocum). As previously mentioned, DVLs are rarely available in underwater gliders and often considered an optional payload. Default dead-reckoning navigation relies on IMU and

depth sensors to approximate the planar velocities of the vehicle. Algorithm 1 presents the default DR algorithm in Slocum gliders. It is firstly initialized with a GPS fix (logged at the surface). The initial WGS84 (GPS) coordinates $\boldsymbol{P}_{wgs84} = [\lambda, \varphi, h]^T$ (lat,long,alt) are transformed to a local frame denoted by $\boldsymbol{P}_i = [x_i, y_i, z_i]^T$. After the initialization, the speed U in the body frame is computed. The speed is estimated by the depth-rate $\dot{z}$ and pitch angle θ measurements. The speed is further used in a simplified kinematic model to be represented in an inertial frame.

Algorithm 1 DR navigation Slocum [105], [104]

Require: GPS fix: $\boldsymbol{P}_{wgs84} = [\lambda, \varphi, h]^T$
Require: Transform GPS fix to local frame $\boldsymbol{P}_{wgs84} = [\lambda, \varphi, h]^T \rightarrow \boldsymbol{P}_i = [x_i, y_i, z_i]^T$

$U(k) = \frac{\dot{z}}{tan(\theta)}$ ▷ Horizontal speed in body frame
$\dot{x}(k) = U \cdot sin(\psi)$ ▷ North velocity
$\dot{y}(k) = U \cdot cos(\psi)$ ▷ East velocity

if $\Delta k = true$ **then**
  $x(k+1) = x_0 + \sum(\dot{x} \cdot \Delta k)$ ▷ Local approximated north position
  $y(k+1) = y_0 + \sum(\dot{y} \cdot \Delta k)$ ▷ Local approximated east position
end if

if $Cycle = end$ **then**
  Climb to surface ▷ Surface after n cycles of upward and downward glides
$\boldsymbol{P}_{wgs84}(k+1) = [\lambda, \varphi, h]^T$ ▷ Get GPS fix
$\boldsymbol{P}_{wgs84}(k+1) = [\lambda, \varphi, h]^T \rightarrow \boldsymbol{P}_i(k+1) = [x_i, y_i, z_i]^T$ ▷ Convert $\boldsymbol{P}_{wgs84}$ to local NED frame
end if

Remark. *Algorithm 1. is proposed for the Slocum glider that have stable roll motions where* $\phi \approx 0$.

The DR algorithm propose a simplified kinematic model for approximating the planar displacement of the glider. The speed $U = \frac{\dot{z}}{tan(\theta)}$ is represented in the x-z plane, where sway velocities are neglected $v \approx 0$. As this model does not introduce any dynamic parameters, the velocity estimation will be prone to errors as documented in sea-trials [104].

3.3 Neural Network Aided Navigation

The main contribution in this chapter is two neural network velocity observers that predict the relative surge u_r and sway v_r velocities of the glider. We refer to the two networks as *recurrent neural networks (RNNs)*, that is, a network topology that introduces feedback or temporal memory in its hidden layers. The proposed model-free observers are presented in figure 3.2, where the network architecture consists of an input layer, composed of measurements from an IMU, control actions and a depth sensor. The inputs are further passed on to two *Long-Short-Term Memory (LSTM)* recurrent neural networks which estimate the nonlinear relationship between the inputs and outputs. This is followed by a numerical integration in the "DR algorithm" block to predict the planar glider displacement (x_k, y_k).

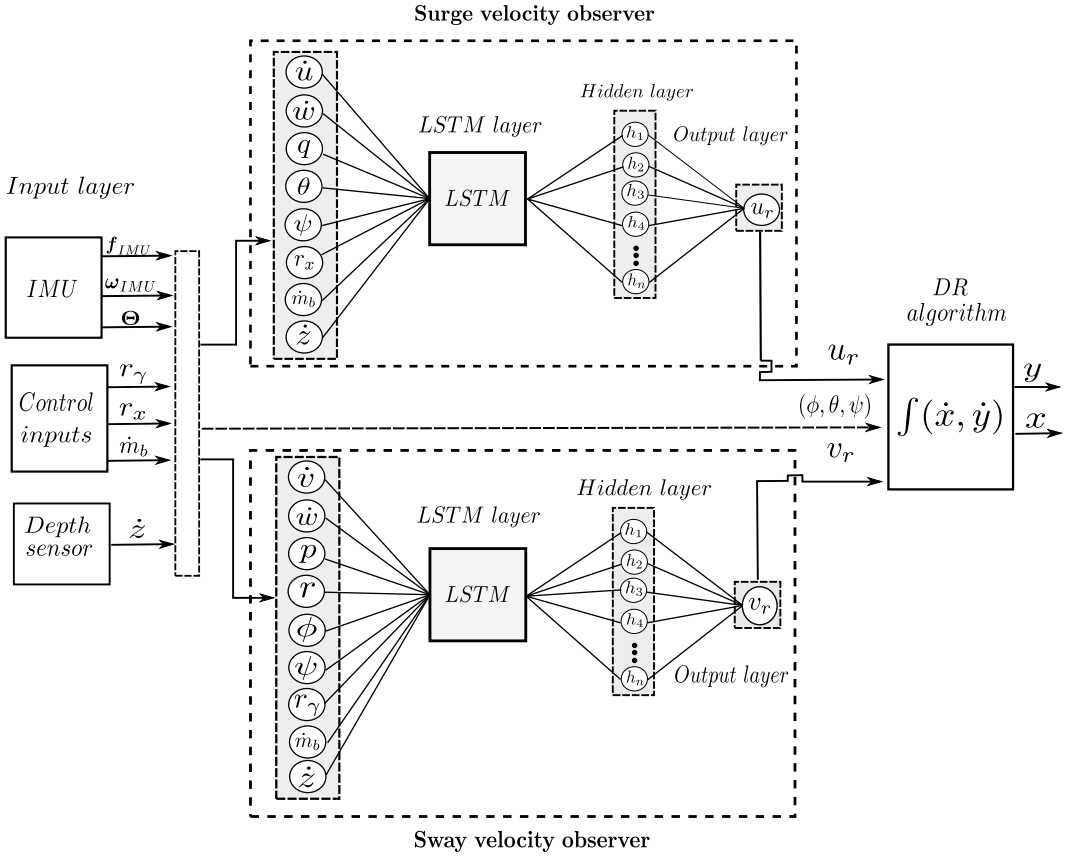

Figure 3.2: Overview of RNN aided DR navigation

In addition to the neural network velocity observers, extensive kinematic models are proposed (eq. 3.2) assuming the glider have active roll motions. Given the RNN velocity observers denoted by $\hat{u}_r(k) = net(r_x, \dot{u}, \dot{w}_r, \theta, \psi, q, \Delta m_b, w_r)$ and $\hat{v}_r(k) = net(r_\gamma, \dot{v}, w_r, \phi, \psi, p, r, \Delta m_b)$, we define the overview of the deep learning approach to DR navigation in the following algorithm

---

Algorithm 2 RNN-aided DR navigation [83]

Require: Initialize position at the surface $\boldsymbol{P}_0^i = [x_0^i, y_0^i, z_0^i]^T$

$\hat{u}_r(k) = net(r_x, \dot{u}, \dot{w}_r, \theta, \psi, q, \Delta m_b, w_r)$ ▷ Neural network surge estimation

$\hat{v}_r(k) = net(r_\gamma, \dot{v}, w_r, \phi, \psi, p, r, \Delta m_b)$ ▷ Neural network sway estimation

▷ North velocity

$$\dot{x}(k) = \hat{u}_r \cdot c(\psi)c(\theta) + \hat{v}_r \cdot (c(\psi)s(\theta)s(\phi) - s(\psi)c(\phi)) + w_r \cdot (s(\psi)s(\phi) + c(\psi)c(\phi)s(\theta)))$$

▷ East velocity

$$\dot{y}(k) = \hat{u}_r \cdot s(\psi)c(\theta) + \hat{v}_r \cdot (c(\psi)c(\phi) + s(\phi)s(\theta)s(\psi)) + w_r \cdot (s(\theta)s(\psi)c(\phi)c(\psi)s(\phi))$$

if $k + 1 = \Delta k$ **then**

$x(k+1) = x_0 + \sum(\dot{x}(k) \cdot \Delta k)$ ▷ Approximated north position

$y(k+1) = y_0 + \sum(\dot{y}(k) \cdot \Delta k)$ ▷ Approximated east position

end if

if $Cycle = end$ **then**

Climb to surface ▷ Surface after n cycles of upward and downward glides

$\boldsymbol{P}_i(k+1) = [x_i, y_i, z_i]^T$ ▷ Reinitalize DR by a "GPS" fix

end if

Remark. *The latter algorithm is proposed for an underwater glider with active roll motions, $\phi \neq 0$. Hence, all euler angles $\boldsymbol{\Theta} = [\phi, \theta, \psi]^T$ are exploited for the kinematic models. Also note that the relative heave velocity w_r is assumed known from depth-rate measurements.*

3.3.1 Artificial Neural Networks (ANNs)

Artificial neural networks (ANNs) have in the last decades become popular in classification and regression problems such as image recognition and time-series forecasting due to its universal properties and ability to learn nonlinear relationships. ANNs mimic biological neural networks trough a simplified mathematical matrix representation consisting of an array of layers with connecting nodes. The nodes represents a mathematical operation which summarizes all the inputs to further be passed onto an activation function that resembles the biological *synapse*.

3.3.2 Long-Short-Term-Memory (LSTM) Neural Networks

One of the most renowned RNN architectures is the LSTM network which has been proposed in many works including state-estimation for marine vehicles [88, 114]. The LSTM cell is known for better *long-term* dependency estimation compared to early *vanilla RNN* networks [88, 111]

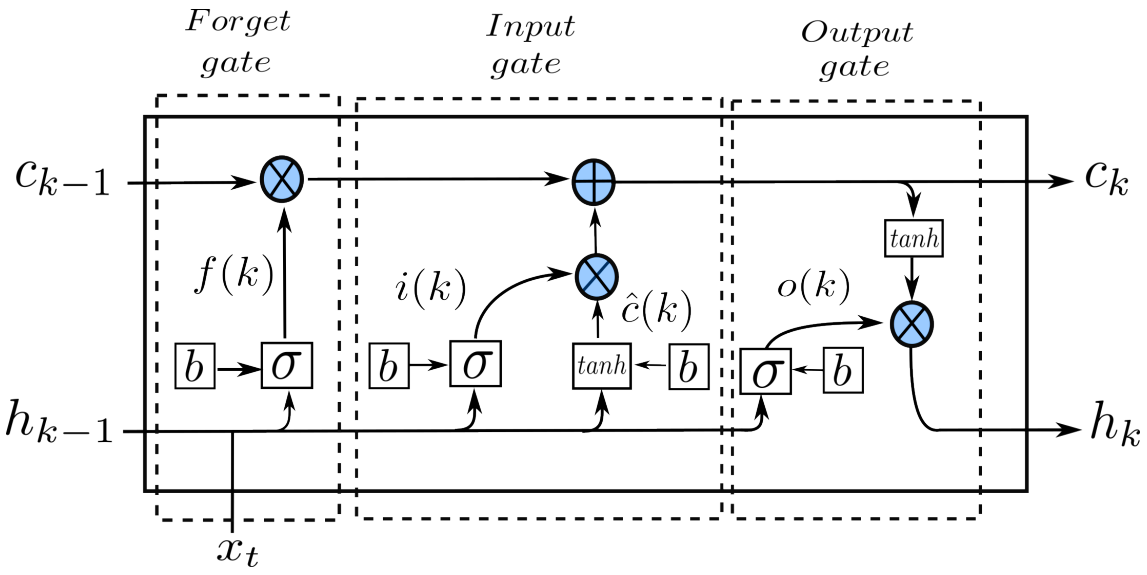

Figure 3.3: LSTM Network topology

The LSTM network topology in figure 3.3 consists of a variety of mathematical operations and functions. Essential to the neural network are the *activation functions* σ (sigmoid) and *tanh* (hyperbolic tangent). These are nonlinear functions, that trough sequential learning, determine when the neuron will be activated.

$$\begin{aligned} \sigma(x) &= \frac{1}{1+e^{-x}}, \ \in \{0,1\} \\ \tanh(x) &= \frac{e^{x}-e^{-x}}{e^{x}+e^{-x}}, \ \in \{-1,1\} \end{aligned} \tag{3.4}$$

The tunable parameters in a LSTM network are the weights w and biases b. Combined with the latter activation functions, the different gates and states of the network topology in figure 3.3 are derived following [111], yielding

$$\begin{aligned} f_k &= \sigma\left(w_{fk} \cdot h_{k-1} + w_{fx} \cdot x_k + b_f\right) \\ i_k &= \sigma\left(w_{ik} \cdot x_k + b_i\right) \\ \hat{c}_k &= tanh\left(W_{\hat{c}_h} \cdot h_{k-1} + W_{\hat{c}_x} \cdot x_k + b_{\hat{c}}\right) \\ c_k &= f_k \cdot c_{k-1} + i_k \cdot \hat{c}_k \\ o_k &= \sigma\left(W_{o_h} \cdot h_{k-1} + W_{ox} \cdot x_k + b_o\right) \\ h_k &= o_k \cdot tanh\left(c_k\right) \end{aligned} \tag{3.5}$$

where c_k is the cell state, f_k is the forget state and h_k is the output state. Accordingly, c_{k-1} and h_{k-1} are the recurring cell and output states respectively. Trough *sequential learning* the LSTM networks are trained. Given a set of inputs $\boldsymbol{x} \in \mathbb{R}^n$ (for instance glider sensor data and control inputs) and reference ground truth outputs $\hat{\boldsymbol{h}}_k \in R^n$ (e.g., DVL measurements), the network is trained by the renowned concept of back-propagation [24,44,94,111], in which the network weights and biases are updated/tuned. Formally, this is referred to neural network regression.

The performance of the output h_k is evaluated by comparing it to a ground truth reference denoted $\hat{h_k}$, commonly referred to as the cost function denoted e, which is typically derived as the mean squared error of the output prediction [94, 111]

$$e = \frac{1}{2}\sum_{k}(\hat{h}_k - h_k)^2 \tag{3.6}$$

where $\hat{h}_k - h_{ik}$ is the difference between the actual and predicted output. The objective of the neural network is to resemble the ground truth reference. From a mathematical perspective, this is achieved trough minimizing the cost function e, by determining the weights w and biases b that minimizes the MSE error in eq. 3.6. Various optimization algorithms have been proposed for sequential learning e.g., gradient decent, stochastic gradient decent (SDG), adaptive moment estimation (Adam optimizer) etc. [2, 111]

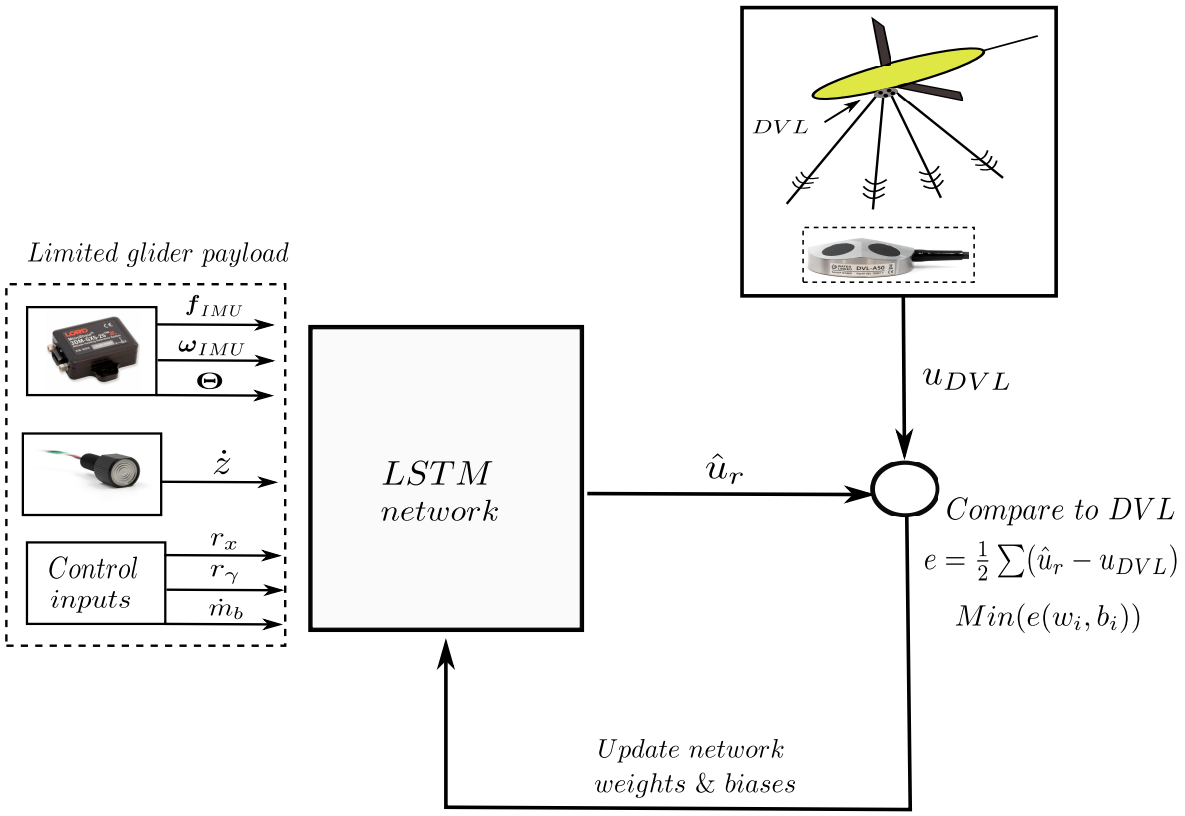

Figure 3.4: Illustrating sequential learning using DVL as ground truth

Remark. *Note that the comparable ground truth variable is just a reference that typi-*

cally holds accurate measurements that we want to reflect. DVLs does not provide absolute measurements of the relative surge and sway velocities, but it's estimation errors are considered acceptable as the instrument is easily integrated to underwater vehicles and cheaper than other novel methods such as underwater motion capture systems, e.g., qualisys [10].

In the latter illustration a DVL is proposed to provide reference measurements for neural network training, which is one of the possible methods for obtaining accurate glider velocities. Other methodologies such as range-only acoustic localization is also convenient for collecting machine/deep learning datasets due to small estimation errors.

3.3.3 Input Layer

The main goal of the neural network velocity observers is to to predict the planar surge u_r and sway v_r velocities of the glider using a limited sensor payload. IMU data, consisting of triaxial accelrometers and gyroscopes are proposed as input variables to the RNN network together with depth-rate measurements and control actions from the onboard actuators. As the surge and sway dynamics is considered decoupled in nominal steady-state glides, we propose two independent neural network velocity observers with the relevant input variables. If the network inputs have little relevance to the predicted output, the network is harder to generalize and may lead to the issue of *overfitting* [44].

3.4 Training data

To train and validate the neural network approach to DR navigation, glider datasets are needed. In this chapter, two gliders are investigated. The first dataset originates from the numerical glider model presented in chapter 2, while the second dataset is from the Tethys hybrid glider/AUV. The Tethys dataset is from a series of sea-trials in Monterey Bay (U.S) and is available trough the Monterey Bay Aquarium Research Institute (MBARI) open source data repository.

3.4.1 Glider datasets

Training datasets from the simulated underwater glider was conducted in Simulink with varying ocean current disturbances. In total, three experiments were conducted with increasing ocean current magnitude and a fixed direction. Furthermore, by performing a square trajectory, the glider collects data from the entire spectrum of $\psi_c = \beta_c - \psi, \ , \psi \in (-\pi, \pi)$. The three different simulation cases were introduced with increasing ocean currents, ranging from $V_c^n \in \{0.14, 0.24, 0.32\}$ m/s. The state variables of in the glider simulation $\boldsymbol{\nu}_r \in \mathbb{R}^6$ and $\boldsymbol{\eta} \in \mathbb{R}^6$ were logged to be used to train the RNN networks. Furthermore, the surge u_r and sway v_r velocities from the three experiments are used as a reference in supervised neural network training.

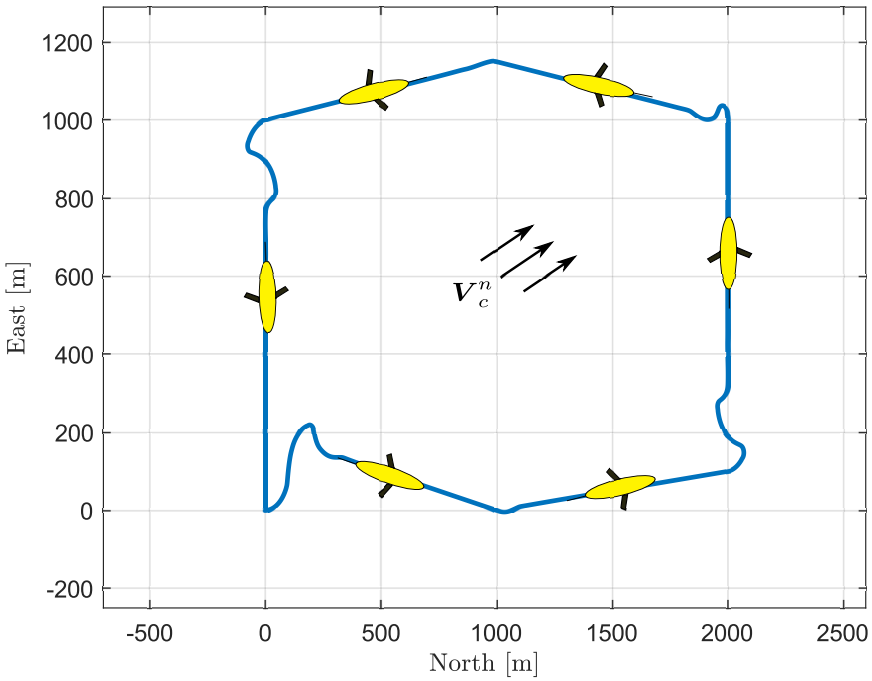

Figure 3.5: Glider simulation scenario 1, $V_c^n = 0.14$ m/s

3.4.2 Tethys datasets

The Tethys hybrid glider/AUV [8, 46] was developed by the Monterey Bay Research Institute (MBARI) as a research vehicle with long-range capabilities. It's characterized as a hybrid AUV as it shares similar control actuators to underwater gliders. This allows it to operate both in undulating glider-like trajectories and at fixed depths using aft thrusters. A series of missions in Monterey bay, California (U.S) were used to train and validate the neural networks. In-situ measurements from a Microstrain 3DM-GX5-24 IMU, Neil Brown pressure sensor and the control actuators were used as inputs to the neural network. Ground truth relative surge and sway velocities $[u_r, v_r]^T$ were provided by a LinkQuest 600 KHz micro DVL.

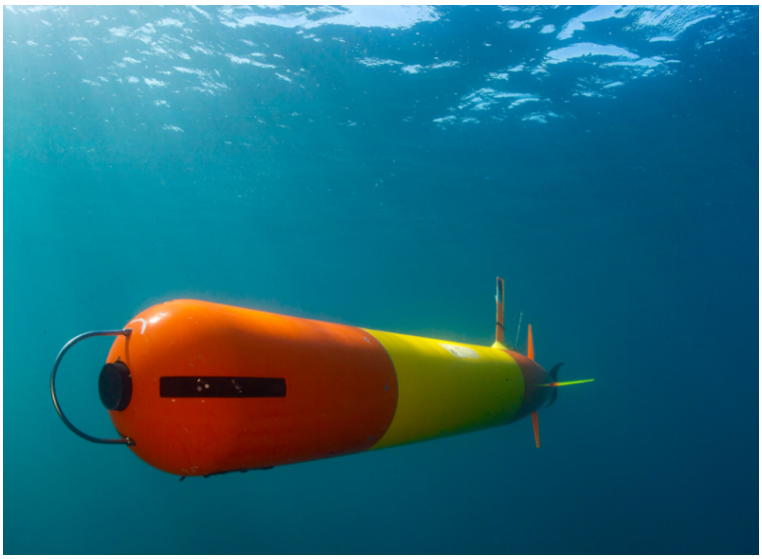

Figure 3.6: Tethys AUV, courtesy of MBARI

The parameters for the IMU and DVL sensors hosted on the Tethys is presented in table 3.1 and 3.2 respectively. The maximum operating altitude refer to *bottom lock* navigation, where the AUV measures it's velocities relative to the seafloor. When out of range the DVL can measure the velocities relative to the water (*water lock*). However, water is often considered as a moving reference frame due to ocean currents, which introduces estimation errors depending on the magnitude of the ocean current vector [80].

Error	value
Accelorometer Bias Instability	$\pm$ 0.04 mg
Gyroscope Bias Instability	$\pm$ 8°/h
Attitude Accuracy	EKF - $\pm$ 0.25° RMS
Heading Accuracy	EKF - $\pm$ 0.8° RMS

Table 3.1: Microstrain 3DM-GX5-25 IMU Parameters

Parameter	Value
Max Altitude	120 meters
Min Altitude	0.3 meters
Accuracy	1 % $\pm$ 1 mm/s
Ping rate	5 Hz

Table 3.2: LinkQuest 600 KHz Micro DVL Parameters

3.5 Experimental and Simulation Results

This section presents two studies which consists of simulated and experimental datasets. The collected datasets were allocated into Matlab and further used to develop, train, and test the neural networks. The Deep Learning Toolbox [67] was used to design network architectures and perform backpropogation training. The Adam (adaptive moment estimation) optimizer was chosen as the training algorithm which is a default option in MATLAB. To improve the generalization of the neural networks, a dropout layer was added to the RNN networks. By stochastically removing/dropping neural network nodes, we prevent the notorious issue of overfitting and improve network generalization [6]. The network architecture consist of a single LSTM layer with 500 hidden nodes. The output layer of the neural network is a fully connected layer with a linear activation function, where the output variable of the two networks are the surge and sway velocities.

Remark. *Because we are removing nodes in the dropout layer it is convenient to have a sufficient number of initial hidden nodes in the network architecture. If the initial configuration has few hidden nodes, the network may end up being too shallow after training.*

3.5.1 Case Study 1 - Seawing Glider

We start by testing the neural network velocity observers to a test dataset/trajectory of the underwater glider. The trajectory is a straight-line trajectory where the glider does repeating upward and downward glides. At each 1000 meters the glider surface to receive a "GPS fix" to reinitialize the DR algorithm. The simulation was carried out with an ocean current magnitude of $V_c^n = 0.23$ m/s and a direction $\beta_c = \pi/2$ rad.

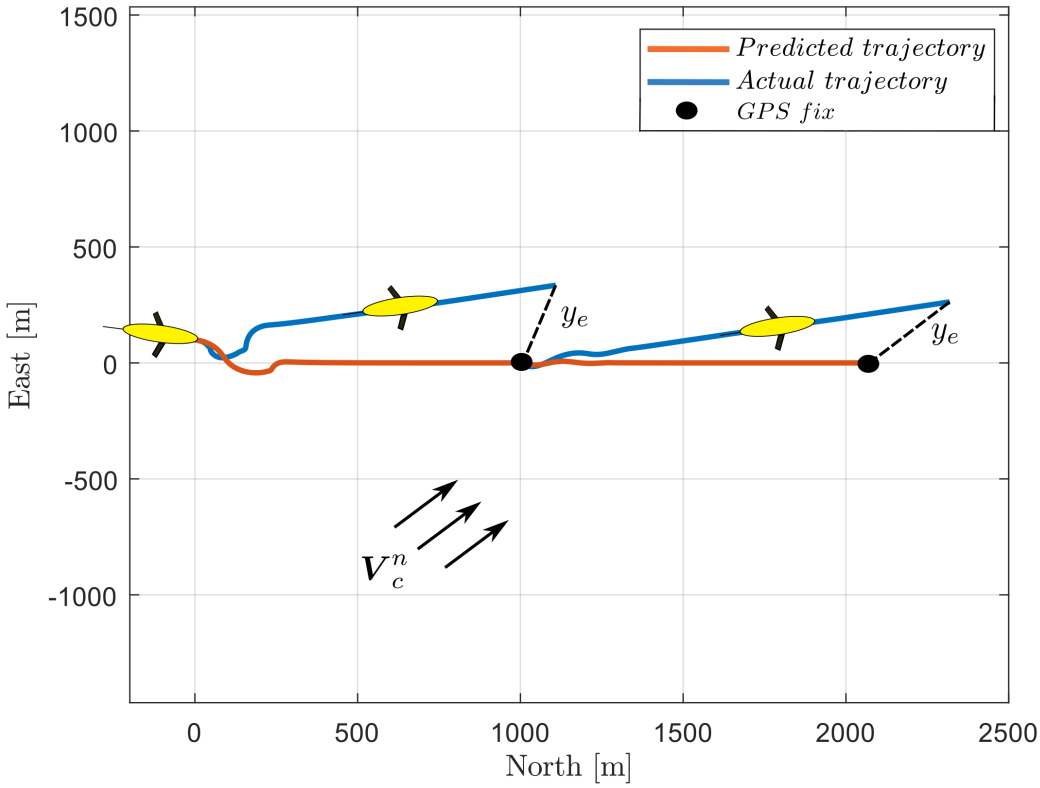

Figure 3.7: Seawing glider - DL navigation

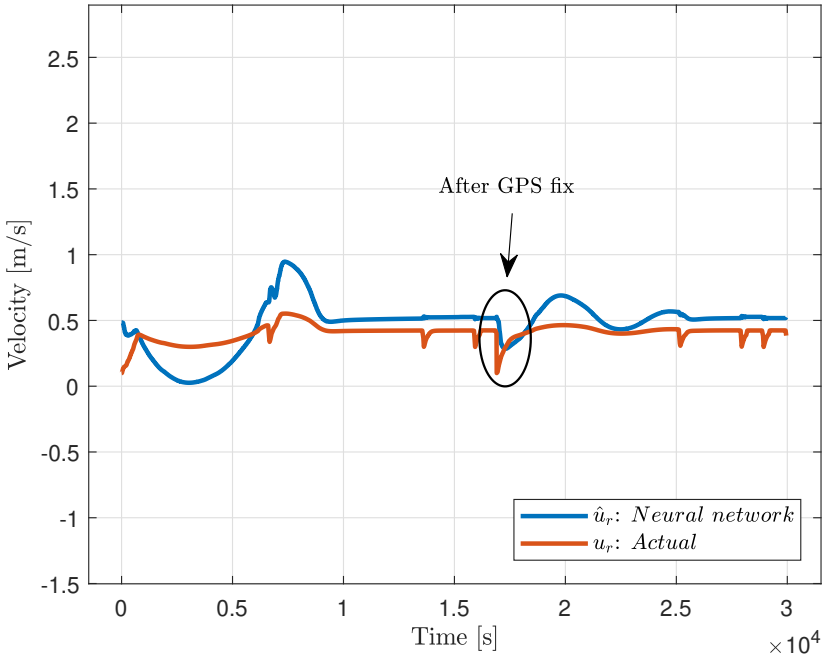

Figure 3.8: Estimated surge velocity $\hat{u}_r$ vs actual surge velocity u_r

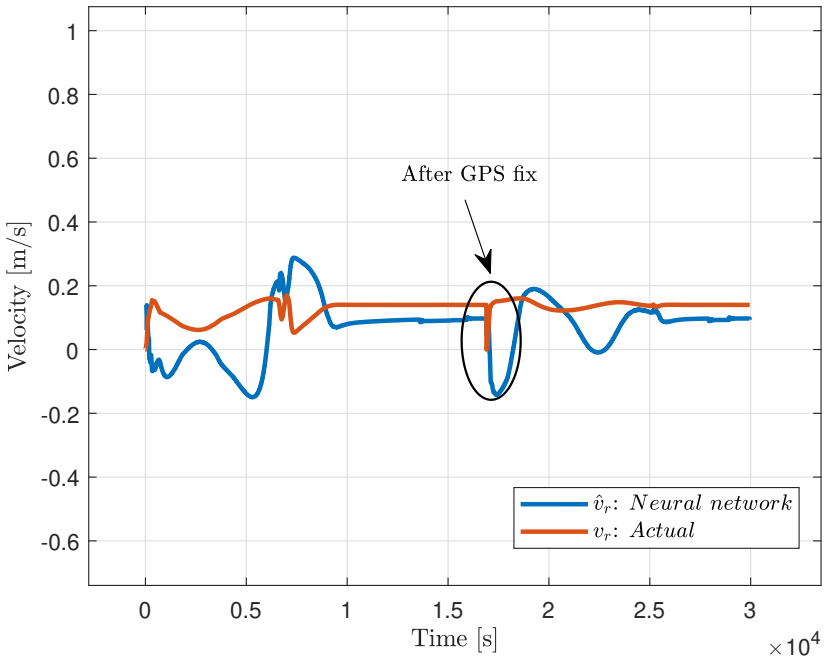

Figure 3.9: Estimated sway velocity $\hat{v}_r$ vs actual sway velocity v_r

3.5.2 Case Study 2 - Tethys AUV

Experimental data from the Tethys AUV/glider was investigated in the second study. Data from three individual surveys were concatenated as a time-series vector and used as training data. Datasets from another mission are used to test the neural network on unseen data. The traning data and test trajectory were conducted in shallow waters where the Linkquest DVL was able to get a bottom lock, although some samples were out of reach for the operating altitude of the DVL sensor. Outliners in the DVL data were removed and further filtered with Gaussian smoothing.

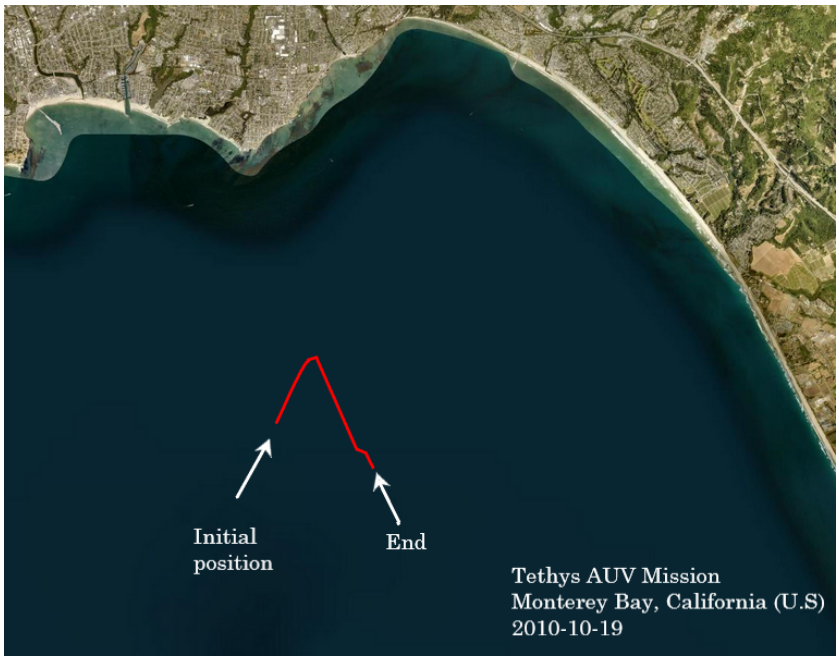

Figure 3.10: Test trajectory in Monterey Bay, California

The test trajectories consist of undulating saw-tooth motions with non-zero angle of attack α as showed in figure 3.14. Note that periodic GPS fixes was not accounted for in the Tethys AUV.

The results are presented in figure 3.13 and 3.14. The blue line represents the predicted position based on estimated surge and sway velocities from the RNN network. The orange line is the estimated position based on measured DVL velocities.

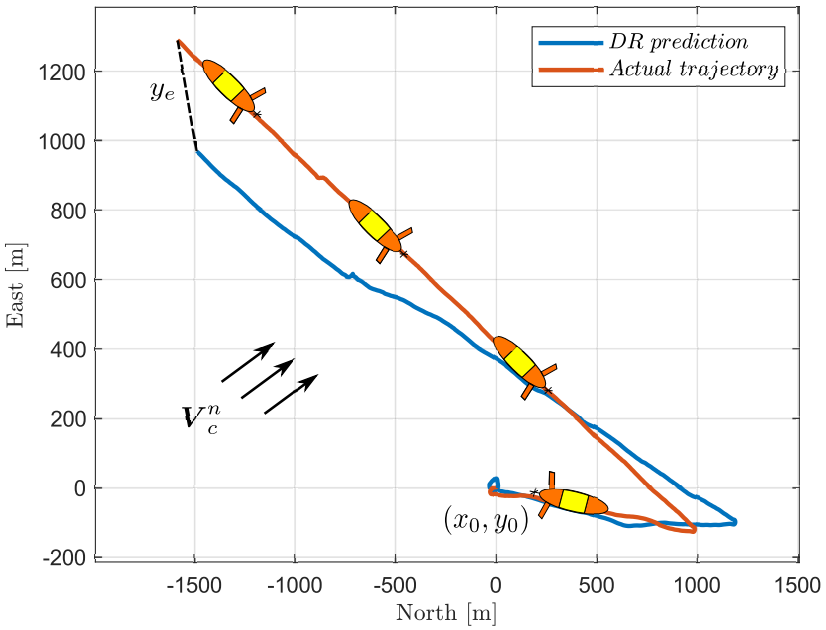

Figure 3.11: Neural network aided navigation - Top view

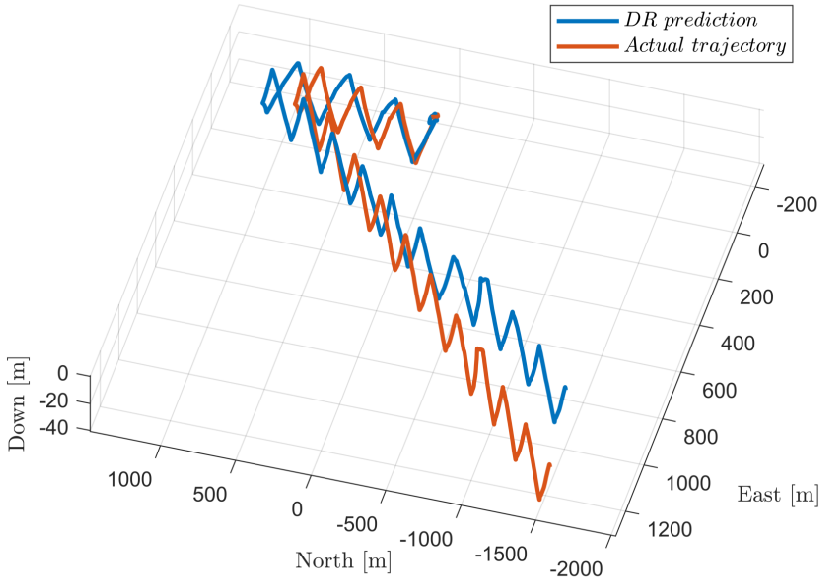

Figure 3.12: Neural network aided navigation - 3D view

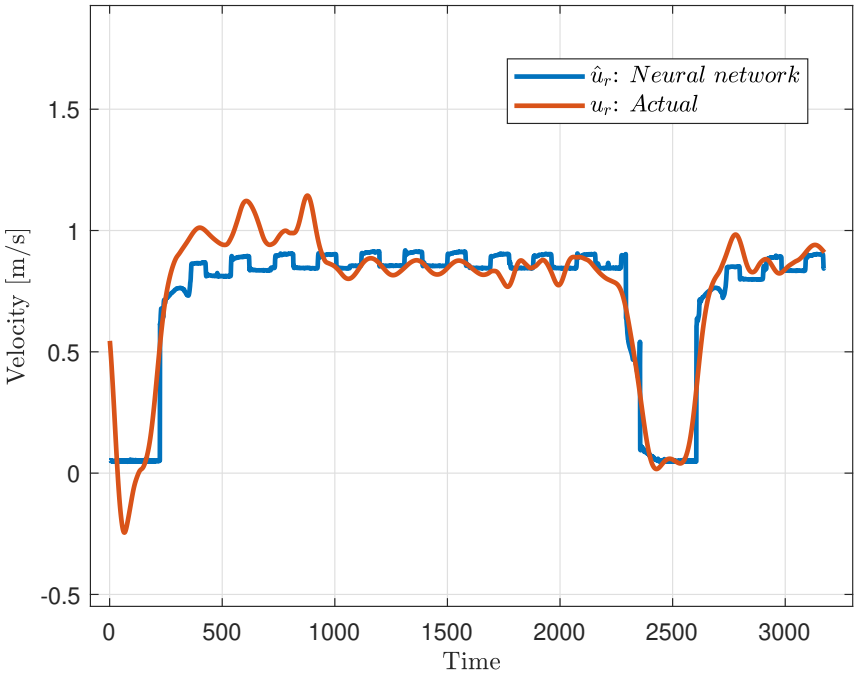

Figure 3.13: Tethys - Estimated surge velocity $\hat{u}_r$ vs actual surge velocity u_r

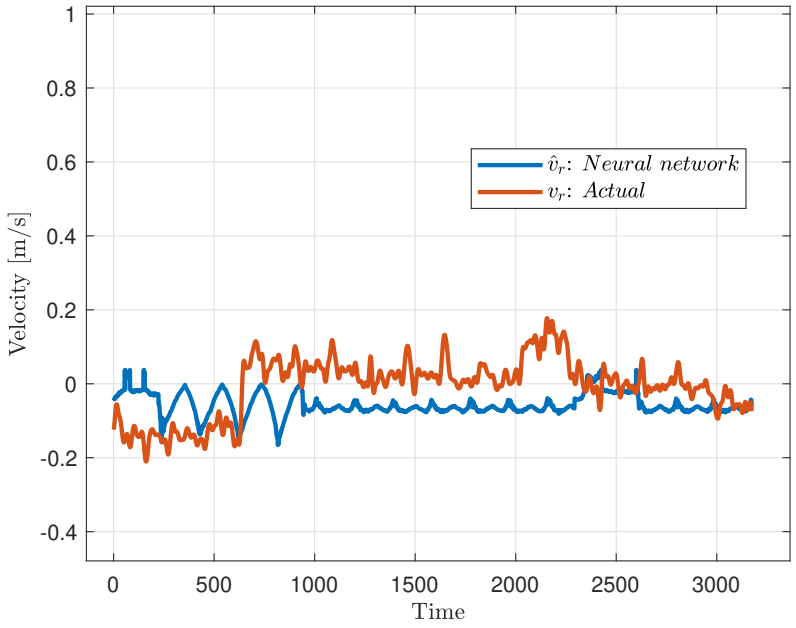

Figure 3.14: Tethys - Estimated sway velocity $\hat{v}_r$ vs actual sway velocity v_r

3.6 Conclusions

In this chapter we have proposed a neural network approach to aid dead-reckoning navigation for gliders with limited sensor suites. Experimental data from an IMU, a pressure sensor and control actions were gathered from sea-trials and simulations with correlating ground truth DVL and simulated velocities. The objective for the trained RNN networks is to complement glider navigation in absence of acoustic navigational instruments. Results from the proposed method show promising potential considering a limited sensor payload, although DR navigation errors are significant and not ideal. The navigation system will be further used as feedback in path-following control, as investigated in the next chapter.

Chapter 4

Path-Following

This chapter investigates planar-motion *path-following* in underwater gliders. We consider two guidance laws for the path-following control problem: I) A *line-of-sight* controller, and II) an *integral line-of-sight* controller, where an integral action corrects drifts from unknown ocean current disturbances. The on-board navigation system, which is the main feedback component to the planar motion guidance laws, is aided by the recurrent neural network (RNN) velocity observers presented in chapter 3 to better approximate the planar position of the glider. The performance of the proposed path-following controllers are analysed in the glider simulation from chapter 2 with varying ocean current conditions.

The theory and results of this chapter were extended to a draft paper for the 14th IFAC CAMS conference:

[84] *Saksvik, I. B., Alcocer, A., Hassani, V. (2022). Path-Following for Underwater Gliders With Limited Navigation Payloads. Draft submitted to the 14th IFAC CAMS: Kgs. Lyngby, Denmark* (Paper is attached in **Appendix B**)

4.1 Introduction

The general guidance application in underwater gliders is straight-line path following, typically defined by a series of waypoints. Due to underactuation, the path-following problem is formulated by the *helsman principle*. The vehicle must change it's course while moving forward to follow an arbitrary planar path. From a mathematical perspective, this consists of computing the heading necessary to converge on the path, while maintaining a steady cruising speed. Furthermore, a *low-level* control system (heading controller) is cascaded with the guidance law to bound the heading control error. Note that the path-following problem does not impose any temporal constraints in the control objective, conversely to *trajectory-tracking* which needs to arrive on a path at a specific time.

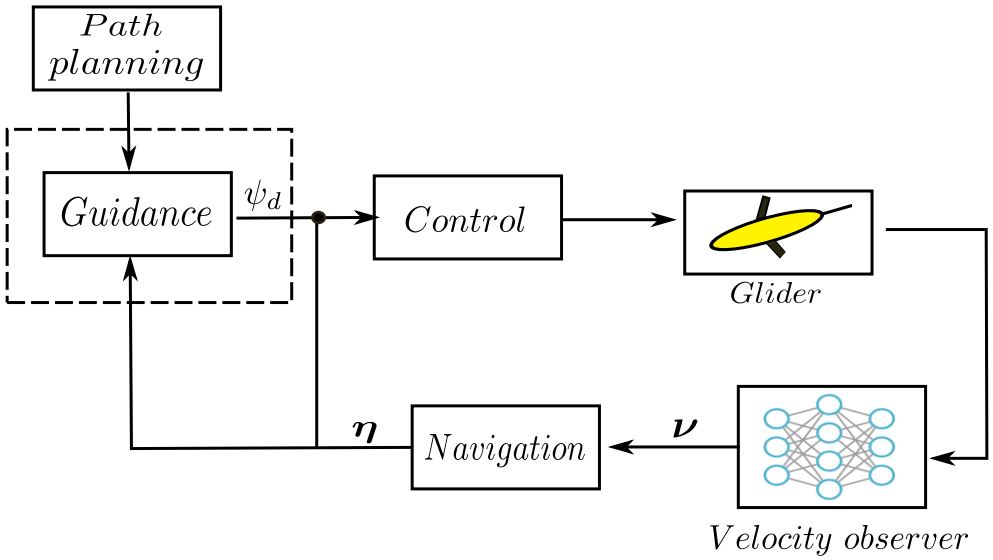

Figure 4.1: GNC block - Guidance

There have been many approaches presented to the path-following control problem for underactuated marine vehicles, mostly by deriving kinematic guidance laws, see [9,13,16,55,103,117], but also reinforcement learning methods have been proposed [64]. *Legacy gliders* such as Slocum use a velocity vector assignment to compute the heading references for the planar motion case [104,105]. This consists of exploiting the velocity

vector of the vehicle with respect to the path and optionally using the ocean current vector to compensate for trajectory drifts.

In recent time, *line-of-sight* (LOS) guidance laws have received popularity in various underactuated marine vehicles [13,55,117]. To compensate for environmental loads, e.g, ocean currents, an integral term can be added to the LOS guidance law as presented in [9, 16, 103]. The purpose of the integral action is to bound the drift between the vehicle and the path, usually manifested by a parallel path due to constant or *slowly-changing* ocean currents.

Based on the latter works in line-of-sight and integral line-of-sight based path-following for AUVs and surface vessels, we aim to extend this approach to underactuated underwater gliders in presence of unknown ocean current disturbances. And, also, investigate the performance of the path-following controllers considering a limited navigation suite with significant dead-reckoning errors.

4.2 Planar Motion Path-following

In this section we derive the *line-of-sight (LOS)* and *integral line-of-sight (ILOS)* guidance laws for the planar motion path-following problem.

The majority of glider missions consists of travelling between geodetic waypoints. The vehicle must occasionally turn when transitioning to a new set of waypoint coordinates. We consider that the path $\mathcal{P}$ is parameterized as a straight line between the predefined waypoints. We can parametarize the straight-line path assuming a scalar $\zeta \in \mathbb{R}$ is given so that

$$\mathcal{P} = \begin{bmatrix} x_p \\ y_p \end{bmatrix} = \begin{bmatrix} x_k + \zeta \cdot cos(\xi_p) \\ y_k + \zeta \cdot sin(\xi_p) \end{bmatrix} \tag{4.1}$$

Where (x_k, y_k) is a fixed location on the path and ξ_p is the angle between the path and the x-axis along the stationary reference frame [13]. Most underwater gliders use internal rotating masses to create a yaw moment by rolling the glider body. The roll

motion will force the wings to be non-collinear in the z-axis, causing the glider to enter a vertical spiral/turn. Due to active roll motions, the kinematic equations of the vehicle are derived by all euler angles $\boldsymbol{\Theta} = [\phi, \theta, \psi]^T$. Following [36] the position of the vehicle in the inertial NED (north-east-down) frame is defined as

$$\begin{bmatrix} \dot{x} \\ \\ \dot{y} \end{bmatrix} = \begin{bmatrix} u_r \cdot c(\psi)c(\theta) + v_r \cdot [c(\psi)s(\theta)s(\phi) - s(\psi)c(\phi)] \\ +w_r \cdot [s(\psi)s(\phi) + c(\psi)c(\phi)s(\theta))] + V_x^n \\ \\ u_r \cdot s(\psi)c(\theta) + v \cdot (c(\psi)c(\phi) + s(\phi)s(\theta)s(\psi)) \\ +w \cdot (s(\theta)s(\psi)c(\phi).c(\psi)s(\phi) + V_y^n \end{bmatrix} \tag{4.2}$$

where $c() = cos()$ and $s() = sin()$. The relative linear velocities are defined as $\boldsymbol{v}_r = [u_r, v_r, w_r]^T = [u - u_c^b, v - v_c^b, w - w_c^b]^T$. Where the ocean current ν_c^b is considered constant and irrotational in the inertial frame.

We start deriving the guidance law by representing the position of the vehicle with respect to the path $\mathcal{P}$. The path is defined by the initial waypoints $(x_k, y_k) \in \mathbb{R}^2$ and the consecutive waypoints $(x_{k+1}, y_{k+1}) \in \mathbb{R}^2$. The straight-line represented by the two waypoints have a *path-tangential angle* defined as

$$\xi_p = atan2(y_{k+1} - y_k, x_{k+1} - x_k) \tag{4.3}$$

where *atan2(x,y)* represents the fourth-quadrant of $tan^{-1}(\frac{y}{x}) \in (-\pi/2, \pi/2)$. Following [55] we can derive the position of the glider with respect to the fixed path, denoted by the cross-track distance x_e and cross-track error y_e:

$$\begin{aligned} x_e &= (x - x_k) \cdot cos(\xi_p) + (y - y_k) \cdot sin(\xi_p) \\ y_e &= -(x - x_k) \cdot sin(\xi_p) + (y - y_k) \cdot cos(\xi_p) \end{aligned} \tag{4.4}$$

The time-derivative of the cross-track error y_e is given by

$$\begin{aligned}\dot{y}_e =& -\dot{x}\cdot s(\xi_p)+\dot{y}\cdot c(\xi_p)\\ =& u_r\cdot c(\psi)\cdot c(\theta)\cdot s(\xi_p)+v_r\cdot(c(\psi)\cdot s(\theta)\cdot s(\phi)\\ & -s(\psi)\cdot c(\phi))\cdot s(\xi_p)+w_r\cdot(s(\psi)\cdot s(\phi)\\ & +c(\psi)\cdot c(\phi)\cdot s(\theta))\cdot s(\xi_p)+V_x^n+u_r\cdot s(\psi)c(\theta)\cdot c(\xi_p)\\ & +v_r\cdot(c(\psi)\cdot c(\phi)+s(\phi)\cdot s(\theta)\cdot s(\psi))\cdot c(\xi_p)\\ & +w_r\cdot(s(\theta)\cdot s(\psi)\cdot c(\phi)-c(\phi)\cdot s(\phi))\cdot c(\xi_p)+V_y^n\end{aligned} \tag{4.5}$$

Stability proofs of eq. 4.5 at the equilibrium $y_e = 0$ have been derived for planar LOS and ILOS guidance laws in various literature, see e.g. [9, 13, 16, 55].

We now derive the LOS guidance law which is defined by the kinematic properties previously defined in this section. Given a path-tangential angle ξ_p, cross-track error y_e and a *look-a-head distance* denoted Λ, the planar motion guidance law is derived by

$$\psi_{LOS} = \xi_p + tan^{-1}(\frac{-y_e}{\Lambda}) \tag{4.6}$$

where $\Lambda > 0$ determines the convergence rate towards the desired path. This is a design parameter (given in meters) that must be tuned correctly. If Λ is too large, the convergence time will be long. If Λ is too small, the convergence rate may be faster than the response of the underactuated vehicle, resulting in oscillating trajectories.
The ILOS guidance law is derived as an extension of eq. 4.6. Following [16] and [9], it is derived as

$$\psi_{ILOS} = \xi_p + tan^{-1}(\frac{-y_e}{\Lambda} + k_i\cdot\int_0^t y_e\, dt) \tag{4.7}$$

In [9] eq. 4.7 is rewritten to avoid anti-windup effects due to the integral term:

$$\psi_{ILOS} = \xi_p - tan^{-1}(\frac{y_e + k_i \cdot \sigma_{int}}{\Lambda})$$
$$\dot{\sigma}_{int} = \frac{y_e \cdot \Lambda}{\Lambda^2 + (y_e + k_i \cdot \sigma_{int})^2} \tag{4.8}$$

where k_i is a design parameter. Equations 4.8 satisfies the property $\{\dot{\sigma}_{int} \to 0\}$ when $\{y_e \to \infty\}$ [9]. Thus, the integration rate is slowed down for large values of y_e, for example when $\psi << \psi_{ILOS}$ which can occur when transitioning between waypoints where $\xi_{p+1} >> \xi_p$.

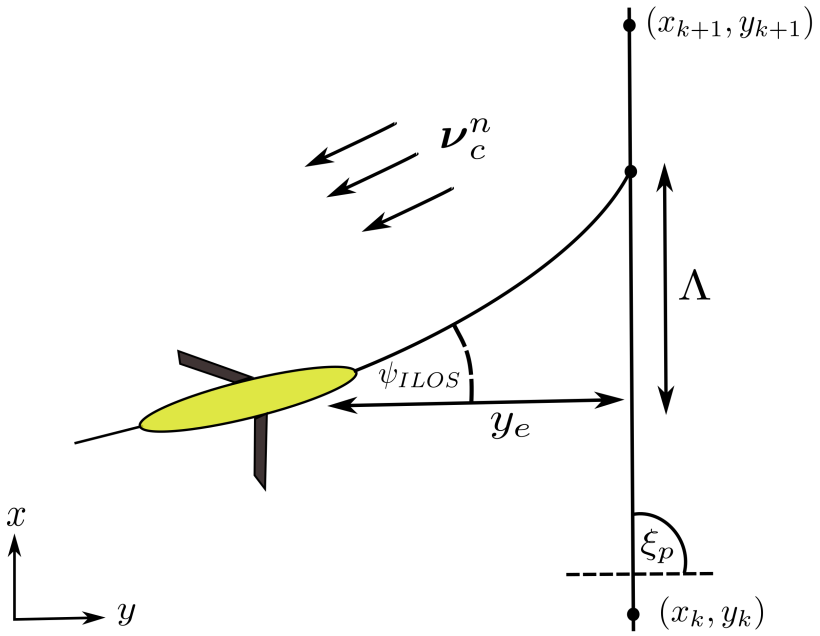

Figure 4.2: ILOS guidance - 2D view

4.2.1 Control Objective

To follow an arbitrary planar path $\mathcal{P} \in \mathrm{R}^2$ the vehicle has to achieve a geometric task (LOS guidance laws) and dynamic tasks (maintaining a constant cruising speed). Hence, the following control objectives are introduced:

$$\begin{aligned} &\lim_{t\to\infty} y_e = 0 \\ &\lim_{t\to\infty} x_e = 0 \\ &\lim_{t\to\infty} (\psi - \psi_{ILOS}) = 0, \;\; \psi \in (-\pi, \pi) \\ &\lim_{t\to\infty} (\theta - \theta_d) = 0, \;\; \theta \in (-\pi/4, \pi/4) \end{aligned} \tag{4.9}$$

The three first conditions imply convergence along the path $\mathcal{P}$. While the last condition ensures that the vehicle will have a relative speed $U_r = \sqrt{u_r^2 + v_r^2 + w_r^2} > 0 \, \forall \, t$.

Remark. *The control objectives imply the that the maneuvering task is underactuated as we want to control 4DOF using only two inputs* $\boldsymbol{u} \in \mathbb{R}^2$.

4.2.2 GNC (Guidance, Navigation & Control)

As previously mentioned we have a GNC feedback loop where the guidance/path-following law is cascaded with the control and navigation systems that were introduced in chapter 2 and chapter 3 respectively. The aim of this chapter is to combine all three systems to relax the control objectives in eq. 5.18. Furthermore, in this chapter the three systems are implemented in the numerical glider model. Following the theory in the latter chapters and in this chapter, the GNC loop is introduced in the following algorithm, which is an extended version of the navigation algorithm 3.3 in the previous chapter.

Algorithm 3 Planar motion path-following

Require: Initialize position at the surface $\boldsymbol{P}_0^i = [x_0^i, y_0^i, z_0^i]^T$

Require: Set look-a-head distance Λ
Require: Set acceptance radius R_e
Require: Set waypoint list $\mathcal{B} = [(x(k), y(k)), (x(k+1), y(k+1)), \ldots, (x(k+n), y(k+n))]$

$\hat{u}_r(k) = net(r_x, \dot{u}, w_r, \theta, \psi, q)$ ▷ Neural network surge estimation
$\hat{v}_r(k) = net(r_\gamma, \dot{v}, w_r, \phi, \psi, p, r)$ ▷ Neural network sway estimation

$$\dot{x}(k) = \hat{u}_r \cdot c(\psi)c(\theta) + \hat{v}_r \cdot (c(\psi)s(\theta)s(\phi) - s(\psi)c(\phi)) + w_r \cdot (s(\psi)s(\phi) + c(\psi)c(\phi)s(\theta)))$$

$$\dot{y}(k) = \hat{u}_r \cdot s(\psi)c(\theta) + \hat{v}_r \cdot (c(\psi)c(\phi) + s(\phi)s(\theta)s(\psi)) + w_r \cdot (s(\theta)s(\psi)c(\phi)c(\psi)s(\phi))$$

if $k + 1 = \Delta k$ **then**
$x(k+1) = x_0 + \sum(\dot{x}(k) \cdot \Delta k)$ ▷ Approximated north position
$y(k+1) = y_0 + \sum(\dot{y}(k) \cdot \Delta k)$ ▷ Approximated east position
end if

$\xi_p(k) = atan2(y_{k+1} - y_k, x_{k+1} - x_k)$ ▷ Path-tangential angle
$y_e(k) = -(x - x_k) \cdot sin(\xi_p) + (y - y_k) \cdot cos(\xi_p)$ ▷ Cross-track error
$\psi_{LOS} = \xi_p + tan^{-1}(\frac{-y_e}{\Lambda})$ ▷ Heading reference
R = $(\mathrm{x}_{k+1} - x)^2 + (y_{k+1} - y)^2$ ▷ Acceptance radius to transit waypoint

$e_\psi(k) = (\psi_{ILOS} - \psi)$
$r_\gamma(k) = e_\psi \cdot k_{p_\psi} + \dot{e_\psi} \cdot k_{d_\psi}$ ▷ Heading control action

if $R <= R_e$ **then**
Climb to surface ▷ Surface after waypoint is reached
$\boldsymbol{P}_i(k+1) = [x_i, y_i, z_i]^T$ ▷ Reinitalize DR by a "GPS" fix
end if

Algorithm 3 is an extension of the dead-reckoning algorithm presented in chapter 3, where path-following control and heading control is added. The approximated north and east positions from DL aided navigation are used to compute the cross-track error y_e. Next, the computed heading reference ψ_{LOS} is fed to the low-level PID heading control law.

4.3 Simulations & Results

The numerical glider model from chapter 2 is used to evaluate the path-following controllers cascaded with the control and navigation systems introduced in previous chapters. The simulation results are twofold - firstly the LOS and ILOS guidance laws are compared with the same ocean current disturbances. In the first simulation ground truth north and east position are proposed as feedback in the planar motion guidance laws. This is not ideal in real glider missions, but illustrates the difference between LOS and ILOS path-following when exposed to ocean current disturbances more clearly. Secondly, the DL aided navigation system presented in chapter 3 is cascaded with the LOS/ILOS guidance laws. Moreover, multiple simulations are carried out to evaluate performance with increased ocean current magnitude $\boldsymbol{V}_c^n$ and directions β_c.

In a real world scenario the path $\mathcal{P}$ cannot be perfectly tracked. Thus, a switching function is needed when the vehicle is close to the desired waypoint. From [13] a *circle of acceptance* mechanism is derived, yielding

$$(x_{k+1} - x)^2 + (y_{k+1} - y)^2 \leq R_{k+1}^2 \tag{4.10}$$

Where R_{k+1} is the radius which must be chosen by the operator. Eq. 4.10 must be satisfied in order to switch to the next waypoint coordinates (x_{k+i}, y_{k+i}).

Before the two simulation cases, the characterization of the look-a-head distance *Lambda* is investigated. Four different scenarios were simulated using the LOS guidance law, where $\Lambda \in \{7, 10, 15, 20\}$ meters.

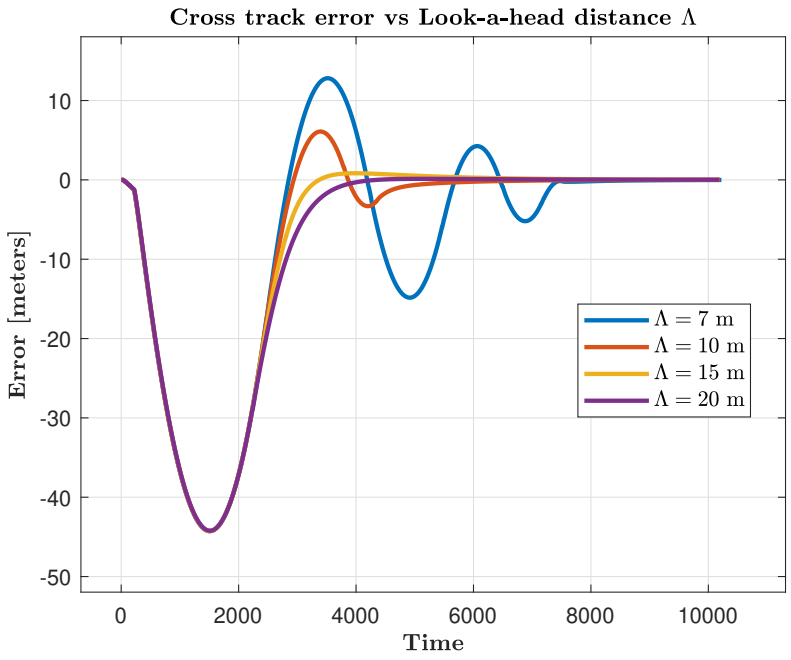

Figure 4.3: Λ vs y_e

Figure 4.3 compares the cross-track error y_e by the different look-a-head distances. Accordingly, when Λ is too short, we observe overshoots and oscillations about the origin $y_e = 0$. Transient responses are present when $\Lambda > 10$ m.

4.3.1 Simulation case 1 - Comparing ILOS and LOS

In the first simulation case the absolute (ground truth) north and east positions are proposed as feedback to the guidance laws. This is to illustrate the differences between LOS and ILOS path-following control laws. The desired path is a straight-line with the initial waypoint $(x_k, y_k) = (0, 0)$ and consecutive waypoint $(x_{k+1}, y_{k+1}) = (3000, 0)$. The initial position and heading of the glider is set to $(x_0, y_0, \psi_0) = (0, 20\,m, \pi/4\,rad)$. An ocean current was present during the simulation with magnitude $V_c^n = 0.15$ m/s and direction $\beta_c = \pi/2$ rad. Accordingly, we let $\Lambda = 12$ m and $\sigma_{int} = 0.05$.

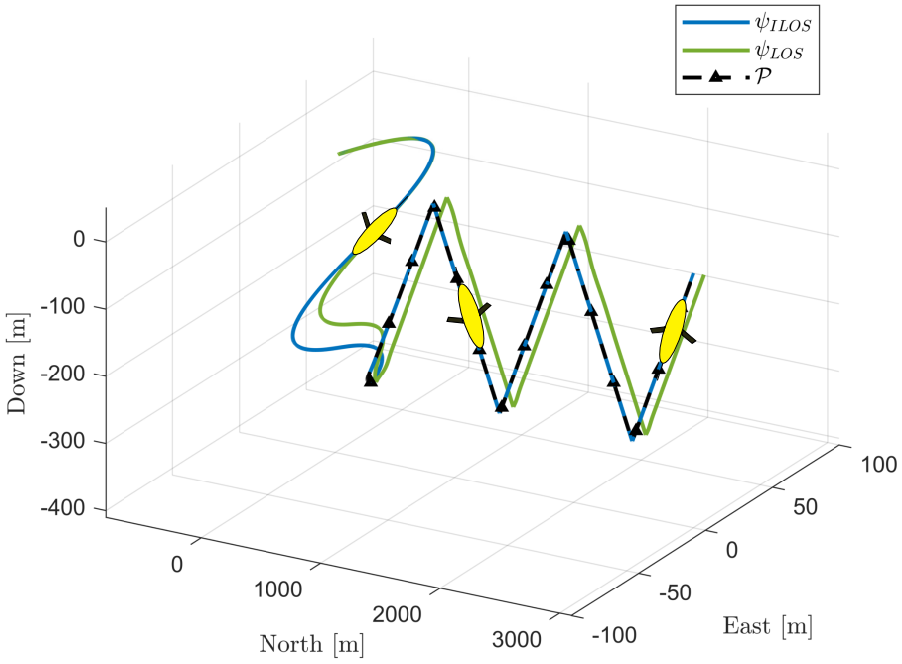

Figure 4.4: Simulation case 1 - 3D positions

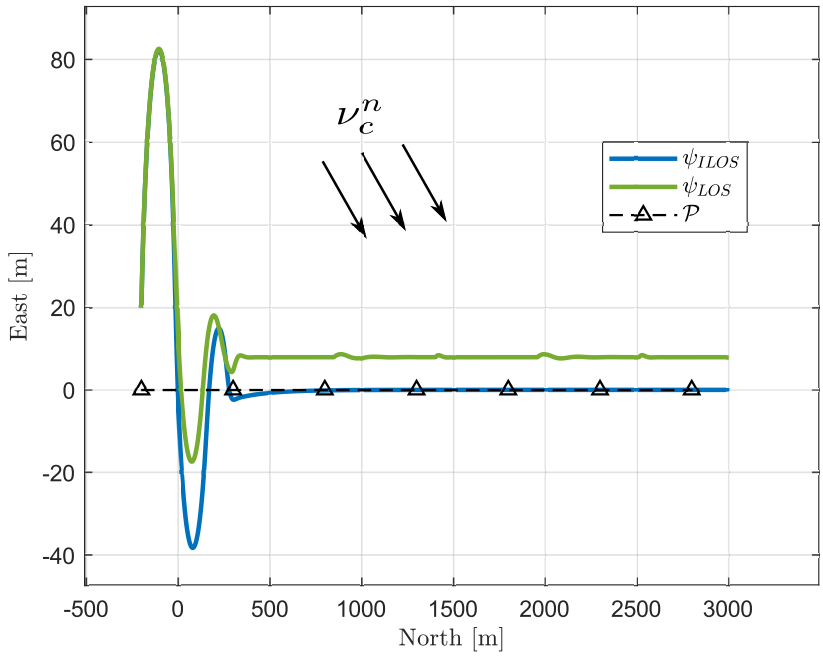

Figure 4.5: Simulation case 1 - 2D positions

Observations in figure 4.4 and 4.5 implies that there is a significant difference in the cross track error y_e between LOS and ILOS guidance. As previously mentioned, the LOS equation fails to correct the drifts from the ocean currents and converge along a parallel path to the desired one. By adding the integral action, the ILOS controller is able to converge along the desired path with very small uncertainties.

4.3.2 Simulation Case 2 - Path-following using RNN velocity observers

In the previous simulation case the ground truth north and east positions were used as feedback for the guidance laws. Having such accurate position estimates is very unlikely for underwater gliders. Thus, the RNN velocity observers from the previous chapter is proposed to predict the north and east position of the glider, which is further fed to the guidance law(s). This section propose two simulation cases, the first considers the same straight-line path as in the previous section, but with different initial conditions. Secondly, a zig-zag path is investigated which have varying path-tangential angles ξ_p. For the straight-line path simulation, the initial state of the glider is $(x_0, y_0, \psi_0) = (0, 100\,m, 0\,rad)$, while the zig-zag path have $(x_0, y_0, \psi_0) = (0, 0, 0)$. The ocean current parameters in the simulations is the same as simulation case 1.

As the RNN-aided navigation system is prone to estimation error, the glider must frequently surface. The glider returns to the surface to get a GPS fix when the DR navigation system "believes" that it has reached the next waypoint (x_{k+1}, y_{k+1}).

Remark. *The simulation is carried out in a local frame (NED) and not geodetic (GPS/WGS84). The "GPS" fix is not of geodetic coordinates in the simulation, but the local NED position it has when returning to the surface. In practice, however, the glider would need to receive a GPS fix and then transform it to the local frame. But, this is not necessary in a simulation environment.*

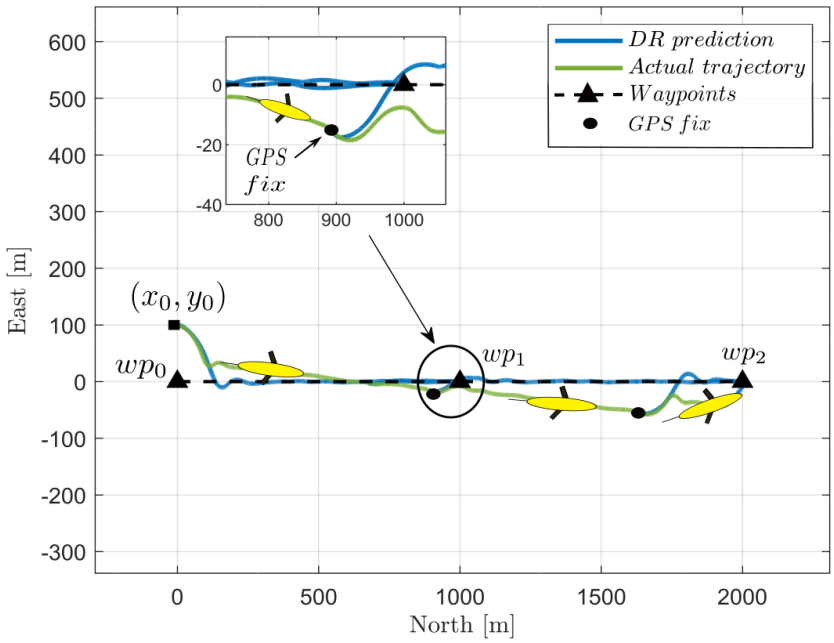

Figure 4.6: Simulation case 2 - straight-line path

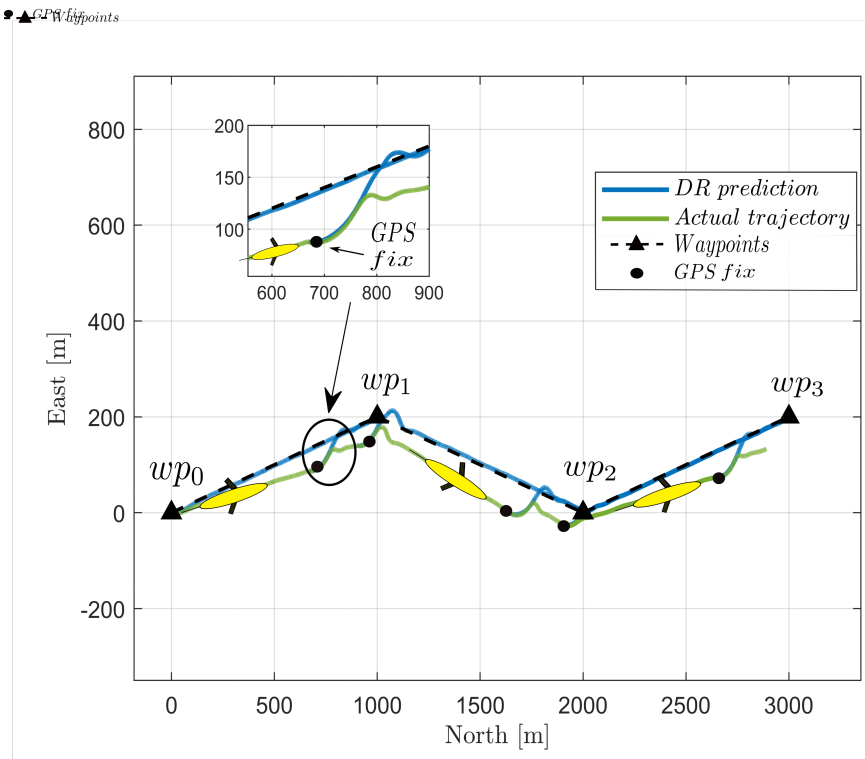

Figure 4.7: Simulation case 2 - zig-zag path

The results in figure 4.6 and 4.7 have far larger cross-track errors than with the previous simulation case using ground truth position feedback in the guidance laws. For the straight-line simulation, the glider surfaced three times to reinitialize the DR algorithm, while 5 times in the secondary simulation with the zig-zag path. Although there are significant dead-reckoning errors present in the results, the glider is able to stay relatively close to the desired path with frequent GPS fixes.

4.3.3 Simulation Case 3 - Comparing LOS and ILOS Guidance Laws in Different Ocean Current Scenarios

In the final simulation case of this chapter, we revisit the straight-line path in the previous simulation case using RNN observers to aid navigation. In this section we introduce increased ocean current magnitudes and direction to investigate the performance of LOS and ILOS guidance laws. The current magnitudes are increased by $V_c^n = \sqrt{u_c^{n2} + v_c^{n2}} \in \{0.1, 0.2, 0.4\}$ m/s, while the direction is step-wise increased by $\beta_c \in \{0, 30, 90, 150, 210, 270, 330\}$ degrees. The different ocean current directions are applied for each magnitude, in total 41 simulations were carried out.

$V_c^n = 0.1m/s$ $(\beta_c, \bar{y}_e)$	$V_c^n = 0.2m/s$ $(\beta_c, \bar{y}_e)$	$V_c^n = 0.4m/s$ $(\beta_c, \bar{y}_e)$
	ILOS	
(0°, 21.0 m)	(0°, 21.2 m)	(0°, 21.1 m)
(30°, 21.6 m)	(30°, 22.4 m)	(30°, 24.0 m)
(90°, 32.5 m)	(90°, 34.6 m)	(90°, 32.5 m)
(150°, 25.0 m)	(150°, 25.9 m)	(150°, 26.6 m)
(210°, 22.2 m)	(210°, 21.8 m)	(210°, 23.0 m)
(270°, 22.1 m)	(270°, 20.1 m)	(270°, 23.8 m)
(330°, 21.9 m)	(330°, 21.4 m)	(330°, 20.7 m)
	LOS	
(0°, 21.5 m)	(0°, 21.3 m)	(0°, 21.4 m)
(30°, 22.8 m)	(30°, 22.1 m)	(30°, 23.9 m)
(90°, 25.7 m)	(90°, 30.9 m)	(90°, 31.1 m)
(150°, 24.9 m)	(150°, 25.8 m)	(150°, 26.32 m)
(210°, 22.9 m)	(210°, 21.5 m)	(210°, 22.6 m)
(270°, 21.6 m)	(270°, 21.4 m)	(270°, 20.7 m)
(330°, 22.6 m)	(330°, 22.0 m)	(330°, 21.0 m)

Table 4.1: Path-following with different ocean current conditions

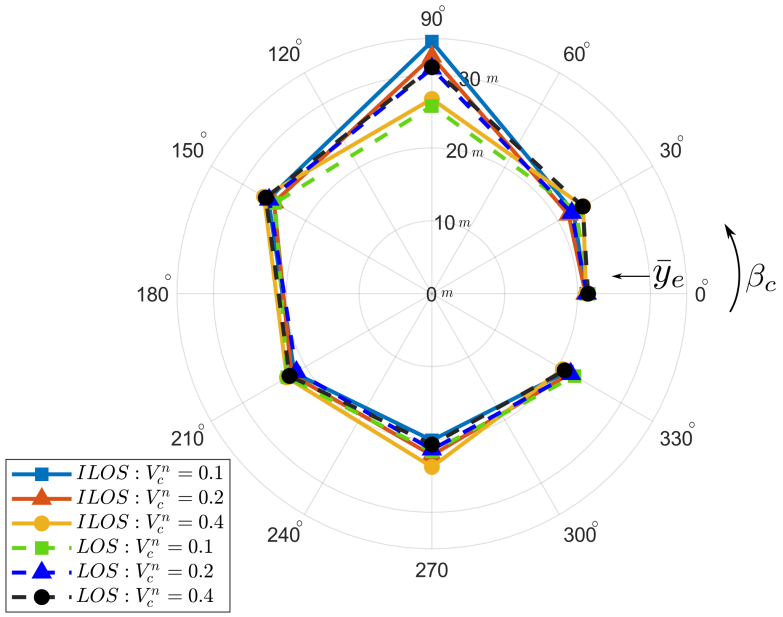

Figure 4.8: Polar plot of table 4.1

4.4 Conclusions

In this chapter we have investigated LOS and ILOS guidance law for the planar motion path-following problem. The guidance laws were compared in the glider simulation framework with different ocean current disturbances. The DL aided navigation system from chapter 3 was added in the GNC loop, providing approximated north and east feedback to the path-following controllers. We show trough extensive simulations, that both guidance laws have convergent behavior when the ocean current disturbance is increased in magnitude and direction. Due to significant DR errors, the glider frequently surface to reinitialize the path-following controller and navigation system.

4.5 Stability Considerations

To end this chapter we discuss the stability of the proposed kinematic LOS and ILOS guidance laws of the origin $y_e = 0$, where the vehicle has converged on the path $\mathcal{P} \in \mathbb{R}^2$. Stability proofs of planar motion line-of-sight path-following control laws are presented in many works [3, 9, 16, 55].

4.5.1 LOS Guidance

We start by investigating the stability for the look-a-head based LOS guidance law that was firstly introduced in this chapter. In this scenario, the ocean current component is not considered, such that $\boldsymbol{V}_c^n = \boldsymbol{0}$. Some assumptions about the kinematic models are firstly defined:

Assumption 12. *The heading and pitch angle is perfectly tracked, such that* $\psi = \psi_{LOS}$, $\theta = \theta_d$.

Assumption 13. *The look-a-head distance* Λ *is chosen such that sway dynamics is relaxed and the rolling mass actuator is fixed at it's initial position* $r_\gamma = 0$ *rad after convergence along the path* $\mathcal{P} \in \mathbb{R}^2$.

Remark. *The pitch control objective imply that the glider is either in an upward or downward steady-state glide, in which the vertical path is fixed. The look-a-head distance must be tuned to hold transient convergence. Otherwise, if too small, it may cause unnecessary oscillations about the desired path.*

Assumption 13 imply that the glider sway dynamics is relaxed, resulting in a zero roll angle $\phi = 0$. Hence, the cross-track error derivative is reduced to

$$\begin{aligned}\dot{y}_e =& - \dot{x} \cdot s(\xi_p) + \dot{y} \cdot c(\xi_p) \\ =& u \cdot c(\psi) \cdot c(\theta) \cdot s(\xi_p) - v \cdot s(\psi) \cdot s(\xi_p) \\ &+ w \cdot c(\psi) \cdot s(\theta)) \cdot s(\xi_p) + u \cdot s(\psi) c(\theta) \cdot c(\xi_p) \\ &+ v \cdot c(\psi) \cdot c(\xi_p) + w \cdot s(\psi) \cdot s(\theta) \cdot c(\xi_p)\end{aligned} \tag{4.11}$$

Accordingly, eq. 4.11 can be simplified using trigonometric identities shown in [3, 55], which yields

$$\begin{aligned}\dot{y}_e =& -c(\psi) \cdot s(\xi_p) \cdot (u \cdot c(\theta) + w \cdot s(\theta)) \\ &+ s(\psi) \cdot c(\xi_p) \cdot (u \cdot c(\theta) + w \cdot s(\theta))\end{aligned} \tag{4.12}$$

Eq. 4.12 is then further simplified by representing the trigonometric equations in *phase-shift format* as proposed in [3, 55]

$$\dot{y}_e = U \cdot cos(\theta - \alpha) \cdot sin(\psi - \xi_p) \tag{4.13}$$

Where $U = \sqrt{u^2 + w^2}$ and $\alpha = atan2(w, u)$. Following assumption 12 the heading is perfectly tracked, such that we substitute ψ with ψ_{LOS} from eq. 4.6, yielding

$$\begin{aligned}\dot{y}_e &= U \cdot cos(\theta - \alpha) \cdot sin(\psi_{LOS} - \xi_p) \\ \dot{y}_e &= U \cdot cos(\theta - \alpha) \cdot sin(\xi_p + tan^{-1}(\frac{-y_e}{\Lambda} - \xi_p))\end{aligned} \tag{4.14}$$

The term $sin(tan^{-1}(-y_e/\Lambda))$ is rewritten using the trigonometric property $sin(arctan(x)) = x \cdot \sqrt{1+x^2}/1+x^2$, such that

$$\dot{y}_e = U \cdot cos(\theta - \alpha) \cdot \frac{-y_e \cdot \sqrt{\Lambda^2 + y_e^2}}{\Lambda^2 + y_e^2} \tag{4.15}$$

Finally the Lyapunov Function Candidate (LFC) is given by

$$V = \frac{1}{2} \cdot y_e^2 \tag{4.16}$$

in which the time-derivative is defined following [3, 55] as

$$\dot{V} = \sqrt{U^2 \cdot cos^2(\theta - \alpha)} \cdot \frac{-y_e^2}{\sqrt{\Lambda^2 + y_e^2}} \tag{4.17}$$

The LFC candidate is negative, which implies universal global asymptotic stability (UGAS) following the stability theory in [54]. [3, 55] also show that the LCF candidate have universal local exponential stability (ULES) and thereby κ-exponential stability.

Remark. *Note that the stability discussed in this section only considers kinematic models which do not introduce any dynamic parameters. The reader may see [9, 16, 103] for extensive stability proofs including vehicle dynamics for the LOS and ILOS guidance laws.*

4.5.2 ILOS Guidance

In the latter section there was no ocean current present for the LOS path-following problem. With Integral Line-of-Sight (ILOS) however, the ocean current vector and relative velocity model is reused when representing the kinematics. In this regard, we rewrite the cross-track error following the work in [9, 16] such that

$$\dot{y}_e = U_r \cdot cos(\theta - \alpha) \cdot sin(\psi) + V_y^n \tag{4.18}$$

where $U_r = \sqrt{u_r^2 + w_r^2}$. Substituting ψ with ψ_{ILOS} in eq. 4.8 gives the subsystem

$$\begin{aligned} \dot{y}_e &= \frac{-U_r \cdot cos(\theta - \alpha) \cdot (y_e + k_i \cdot \sigma_{int})}{\sqrt{(y_e + k_i \cdot \sigma_{int})^2 + \Lambda^2}} + V_y^n \\ \dot{\sigma}_{int} &= \frac{y_e \cdot \Lambda}{\Lambda^2 + (y_e + \kappa \cdot \sigma_{int})^2} \end{aligned} \tag{4.19}$$

The subsystem 4.19 have the following equilibrium points

$$\sigma_{int}^{eq} = \frac{\Lambda \cdot V_c^n}{k_i \cdot (U_r \cdot cos(\theta - \alpha) - V_c^n)}, \;\; y_e^{eq} = 0 \tag{4.20}$$

It's necessary to move the equilibrium point to the origin. Following [54] and [16] we have

$$\zeta_1 = \sigma_{int} - \sigma_{int}^{eq}, \;\; \zeta_2 = y_e + k_i \cdot \zeta_1 \tag{4.21}$$

where ζ_1 and ζ_2 are differentiated as

$$\dot{\zeta}_1 = \frac{\Lambda \cdot \zeta_2}{(\zeta_2 + k_i \cdot \sigma_{int})^2 + \Lambda^2} - \frac{\Lambda \cdot k_i \cdot \zeta_1}{(\zeta_2 + k_i \cdot \sigma_{int})^2 + \Lambda^2}$$

$$\begin{aligned} \dot{\zeta}_2 = &\frac{-U_r \cdot cos(\theta - \alpha) \cdot \sqrt{(\zeta_2 + k_i \cdot \sigma_{int})^2 + \Lambda^2} - k_i \cdot \Lambda \cdot \zeta_2}{(\zeta_2 + k_i \cdot \sigma_{int})^2 + \Lambda^2)} \\ &- \frac{\Lambda \cdot k_i^2 \cdot \zeta_1}{(\zeta_2 + k_i \cdot \sigma_{int})^2 + \Lambda^2)} - V_c^n \cdot \frac{\sqrt{(k_i \cdot \sigma_{int})^2 + \Lambda^2)}}{\sqrt{(\zeta_2 + k_i \cdot \sigma_{int})^2 + \Lambda^2}} \end{aligned} \tag{4.22}$$

The Lyapunov function candidate (LFC) is defined following [16,103], which is quadratic,

$$V = \frac{k_i^2}{2} \cdot \zeta_1^2 + \frac{1}{2} \cdot \zeta_2^2 \tag{4.23}$$

and have the time derivative

$$\begin{aligned}\dot{V} = &-(-k_i \cdot \Lambda + U_r \cdot cos(\theta - \alpha) \cdot \sqrt{(\zeta_2 + k_i \cdot \sigma_{int})^2 + \Lambda^2}) \\ &\cdot \frac{\zeta_2^2}{(\zeta_2 + k_i \cdot \sigma_{int})^2) + \Lambda^2} - \frac{k_i^3 \cdot \Lambda}{(\zeta_2 + k_i \cdot \sigma_{int})^2 + \Lambda^2} \cdot \zeta_1 \\ &- V_c^n \cdot \frac{\sqrt{(k_i \cdot \sigma_{int})^2 + \Lambda^2)}}{\sqrt{(\zeta_2 + k_i \cdot \sigma_{int})^2 + \Lambda^2}} + V_c^n\end{aligned} \tag{4.24}$$

Following [16] the LCF candidate is bounded by

$$\dot{V} \leq -k_i^3 \cdot \Lambda |\zeta_1|^2 - \Lambda \cdot (U_r - k_i) \cdot |\zeta_2|^2 = W \tag{4.25}$$

which yields uniformly global asymptotic stability (UGAS) as W is positive definite. It is further proved in [16] that the equilibrium point is uniformly exponentially stable locally (ULES).

Remark. *The stability considerations in [16] are based on a kinematic model of a surface vessel. We modify this model by adding the term $cos(\theta - \alpha)$ to suit the underwater glider in a steady-state glide with non-zero angle of attack. As the kinematic models do not include dynamics they can be applied to different types of vehicles. Stability considerations involving vehicle dynamics for the ILOS guidance law is further detailed in [9, 16, 103] for thruster based AUVs and surface vessels.*

Chapter 5

Tracking Underwater Gliders Using an Unmanned Surface Vessel (USV)

This chapter propose a methodology for target tracking of an underwater glider using an *unmanned surface vessel* (USV). The topside USV is assumed to have knowledge about the position of the underwater glider from an acoustic positioning system, which is exploited to track the planar motions of the submerged vehicle from the surface. We propose a target tracking method for the purpose of glider localization using unmanned systems to reduce the operational costs and potential hazards. A guidance law is implemented in the topside vehicle to pursuit and intercept the underwater glider while it's performing generic saw-tooth and spiral maneuvers. A numerical simulation environment of the two vehicles is presented to validate the target-tracking scheme.

The theory and results from this chapter is the origin for the conference paper draft:

[85] *Saksvik, I. B., Alcocer, A., Hassani, V & Pascoal, A. (2022). Tracking Underwater Gliders Using Small Unmanned Surface Vessel (USV). Draft submitted to the 14th IFAC CAMS: Kgs. Lyngby, Denmark* (Paper is attached in **Appendix D**)

Navigation systems onboard underwater gliders are often prone to estimation errors due to limited sensor payloads. In practice, inertial measurement units (IMUs) and depth sensors are used to approximate the position of the glider trough simple kinematic equations, which frequently lead to navigation errors. Absence of accurate position estimates makes it challenging to evaluate guidance, navigation and control (GNC) systems. To obtain accurate estimates of glider trajectories, an acoustic baseline positioning system is typically employed as demonstrated in [42] and [5]. In practice, however, this requires cumbersome and costly deployment and calibration of a number of transponders in the seabed. This work proposes a strategy for obtaining such trajectories using an unmanned boat equipped with a low-power acoustic positioning system with limited calibration requirements.

Due to range limitations in low-power acoustics, it's convenient to bound the planar distance between the topside vessel and submerged vehicle. From a control perspective, we refer to this as *target-tracking*, that is, to pursuit a moving target whose future motions are not known. The objective in this paper is to let the topside vessel track the horizontal displacement of the submerged glider. This motion control problem has been introduced in several underwater target-tracking & localization schemes using one or more autonomous surface vessels (ASVs), see e.g., [47, 48, 77]. The maneuvering task related to tracking and localization is highly dependent upon the number of range-measurements available to the topside vehicle(s). For instance, single-beacon vehicles, limited to one acoustic range measurement, impose a challenge to represent the target on a sphere (3D case) or circle (2D case) surrounding the recipient. In [73] and [65] the latter issue is solved by continuously encircling around about the target to increase the range-information from the target. In this paper we assume that the topside vessel is equipped with a short baseline (SBL) acoustic positioning system and that the position of the target is known throughout the simulation experiments. Moreover, a vectorial guidance law is proposed for the USV to track generic motions of an underwater glider. The guidance system is derived based on the *helsman principle* as the vessel cannot

actuate the sway dynamics without changing it's course. Hence, the guidance law is decomposed to surge velocity and heading controllers to relax the dynamic and kinematic assignments of the target-tracking scheme respectively.

5.1 Target Tracking Guidance Law

The topics in airborne guidance systems have been extended to underactuated marine vessels in various research, see e.g. [12, 14, 77], and [87]. In this section we derive a constant bearing (CB) guidance law based on the theory presented in the latter works. Following the notation in [14], we now refer to the surface vessel as the *interceptor* and the underwater glider as the *target*. Before deriving the guidance law we introduce some assumptions:

Assumption 2.1: *The following vectorial definitions are defined with respect to a fixed local frame denoted* $\{n\}$ *with an origin located at an arbitrary point.*

Assumption 2.2: *The tracked target is assumed to be a moving target such that the vessel speed satisfies* $U_t^n(t) > 0 \, \forall \, t$

Assumption 2.3: *The proposed guidance law consider a target moving in a planar plane, where vertical motions are neglected.*

Remark 2.1: *Assumption 2.1 implies that the interceptor has no information about the target's motion in the body-fixed frame* $\{b\}$*. Secondly, the origin of the fixed local frame* $\{n\}$ *is chosen by the control operator, typically somewhere close to the operation [80]*

Guidance laws are typically derived at a kinematic level. Considering a horizontal plane, we define the planar distance between the target $\boldsymbol{P}_t^n \in \mathrm{R}^2$ and interceptor

$\boldsymbol{P}_u^n \in \mathrm{R}^2$ as

$$\hat{\boldsymbol{P}}^n = (\boldsymbol{P}_t^n - \boldsymbol{P}_u^n) = \begin{bmatrix} x_t^n - y_t^n \\ x_u^n - y_u^n \end{bmatrix} \tag{5.1}$$

Differentiate $\boldsymbol{P}_t^n$ and $\boldsymbol{P}_u^n$ with respect to time yields the inertial velocities $\boldsymbol{\nu}_t^n = [\dot{x}_t^n, \dot{y}_u^n]^T$ and $\boldsymbol{\nu}_u^n = [\dot{x}_u^n, \dot{y}_u^n]^T$. Following [14], the CB guidance law is presented as a velocity assignment

$$\boldsymbol{\nu_d^n} = (\boldsymbol{\nu_t^n} + \boldsymbol{\nu_a^n}) \in \mathrm{R}^2 \tag{5.2}$$

where $\boldsymbol{\nu_a} \in \mathrm{R}^2$ is the desired approach velocity vector. Given a maximum approach speed $\bar{U}_a$ and a transient control parameter Λ, the approach velocity is given by

$$\boldsymbol{\nu_a^n} = \bar{U}_a^n \cdot \frac{\hat{\boldsymbol{P}}_n}{\sqrt{\hat{\boldsymbol{P}}_n^T \cdot \hat{\boldsymbol{P}}_n + \Lambda^2}} \in \mathrm{R}^2 \tag{5.3}$$

The maximum approach speed $\bar{U}_a^n$ must be chosen carefully according to maneuverability considerations and physical limitations of the USV.

Most vessels have underactuated sway dynamics during nominal operations (< 1 m/s). Accordingly, we cannot directly apply the desired velocity vector $\boldsymbol{\nu}_u^n$ onto the vessel. However, we can decompose the CB guidance law into surge and heading references, where the surge controller controls the velocity size and a heading controller is able to control the direction of the velocity vector. From the velocity assignment in eq. 5.2, we have the following velocity control objective:

$$\lim_{t \to \infty} (U_d^n - U_u^n) = 0 \tag{5.4}$$

where $U_d^n = \sqrt{\dot{x}_u^2 + \dot{y}_u^2}$ is the speed of the vessel. It is convenient to assume that $\dot{x}_u^n >> \dot{y}_u^n$ and that we let U_d^n yield

$$u_d^b \approx U_d^n \tag{5.5}$$

This introduces a new control objective, given as

$$\lim_{t\to\infty}(u_d^b - u_u^b) = 0 \tag{5.6}$$

where u_u^b is the surge velocity of the vessel in the body-fixed frame $\{b\}$.

A *line-of-sight* (LOS) guidance law is used to compute heading references for the vessel. Following [87] and [13], the LOS guidance law is derived based on the relative position and orientation of the vessel with respect to the target position $\boldsymbol{P}_t \in \mathrm{R}^2$. The cross-track distance x_e and cross-track error y_e is given by

$$\begin{aligned} x_e^n &= \ (x_u^n - x_t^n)\cdot cos(\chi_t) + (y_u^n - y_t^n)\cdot sin(\chi_t) \\ y_e^n &= -(x_u - x_t)\cdot sin(\chi_t) + (y_u - y_t)\cdot cos(\chi_t) \end{aligned} \tag{5.7}$$

where $\chi_t = atan2(\dot{y}_t^n, \dot{x}_t^n) \in [-\pi, \pi]$ is the target course angle. The LOS guidance law is derived with a *look-a-head* distance parameter Λ which determines the convergence rate towards the desired path. Λ is given in meters and must be tuned carefully such that it does not exceed the maneuverability properties of the vessel. A common practice is to let $\lambda \in \{2, 5\} \cdot L_{usv}$. Where L_{usv} is the length of the vessel. Following [13] and [87] we have

$$\chi_{LOS} = tan^{-1}(\frac{-y_e^n}{\lambda}) \tag{5.8}$$

We can derive the desired heading reference by

$$\psi_d = (\chi_{LOS} + \chi_t) - \beta_u \tag{5.9}$$

where $\beta_u = atan(-\dot{y}, \dot{x})$ is the sideslip angle of the USV

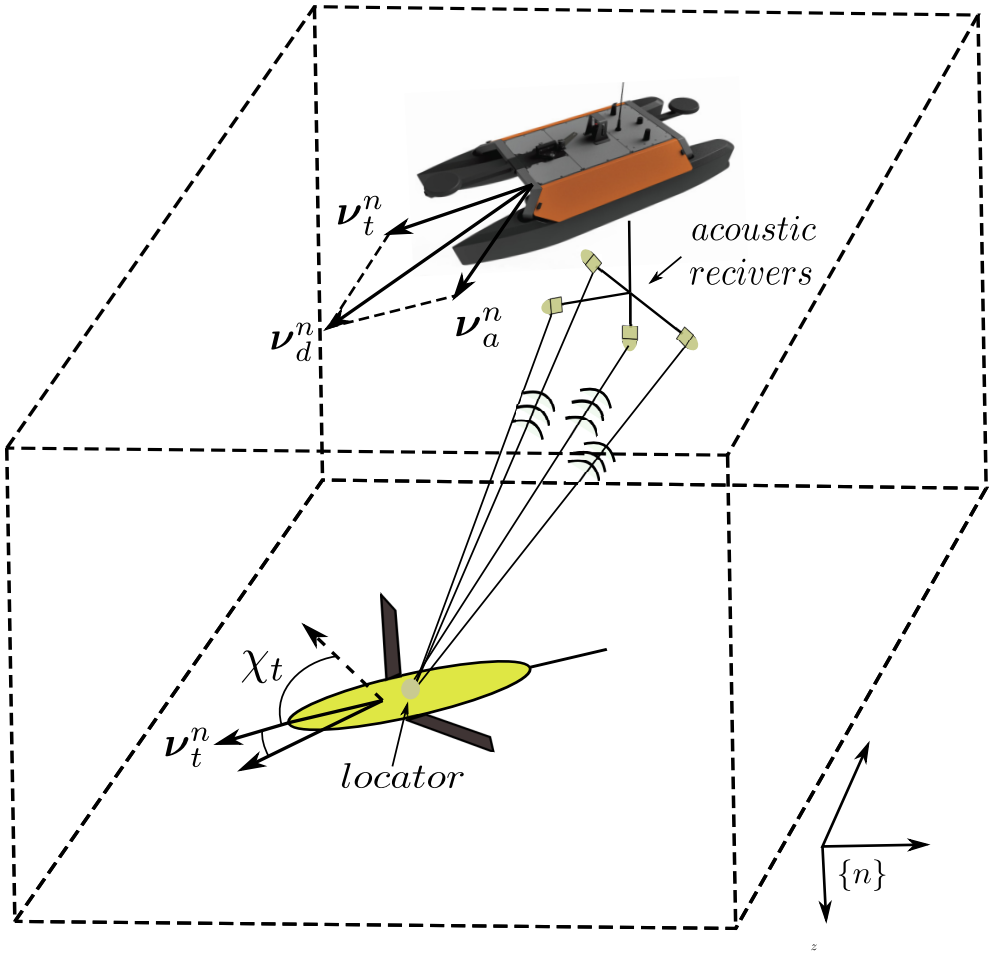

Figure 5.1: Target tracking of glider using an USV

5.2 USV Model

This section details the dynamics of the unmanned surface vessel. The vehicle simulated in this paper is the *Otter USV* developed by Maritime Robotics. The vehicle is characterized as a small unmanned catamaran as illustrated in figure 5.1. Before deriving the equations of motion, we introduce some basic assumptions about the system:

Assumption 3.1: *The vessel is actuated by differential thrust from two fixed stern propellers*

Assumption 3.2: *Environmental wind and wave loads acting on the vessel* $\boldsymbol{\tau}_{wind}, \boldsymbol{\tau}_{wave}$ *are neglected*

Assumption 3.3: *The payload (acoustic receiver antenna) hydrodynamic drag and added mass effects are neglected*

Assumption 3.4: *The vessel is influenced by an ocean current* $\boldsymbol{V}_c^n = [V_x, V_y, 0]^T$ *which is considered constant and irrotational in the inertial frame, hence* $\dot{\boldsymbol{V}}_c^n = 0$.

Assumption 3.5: *The hydrodynamic damping of the vessel is considered linear*

The marine craft kinematics and dynamics are derived using the following state vectors: $\boldsymbol{\eta} = [x, y, \psi]^T$ consists of the inertial position and the heading (yaw) ψ of the vessel. The dynamics is defined by $\boldsymbol{\nu} = [u, v, r]^T$. Due to constant irrotational ocean currents, we rewrite the latter vector into a relative velocity vector following [36]: $\boldsymbol{\nu}_r = [u_r, v_r, r]^T = [u - u_c^b, v - v_c^b, r]^T$. The kinematics are defined by a rotation matrix $\boldsymbol{R_b^n(\psi)}$ from the body-frame $\{b\}$ to the inertial NED frame $\{n\}$. Accordingly, we have

$$\boldsymbol{R}_b^n(\psi) \triangleq \begin{bmatrix} c(\psi) & -s(\psi) & 0 \\ s(\psi) & c(\psi) & 0 \\ 0 & 0 & 1 \end{bmatrix}, \in SO(3) \tag{5.10}$$

where $c = cos()$ and $s = sin()$. The marine craft dynamics and kinematics of an unmanned surface vessel is given by

$$\dot{\boldsymbol{\eta}} = \boldsymbol{R}(\psi)\boldsymbol{\nu}_r + \boldsymbol{V}_c^n \tag{5.11}$$

$$\boldsymbol{M}\dot{\boldsymbol{\nu}_r} + \boldsymbol{C}(\boldsymbol{\nu_r})\boldsymbol{\nu}_r + \boldsymbol{D}(\boldsymbol{\nu_r})\boldsymbol{\nu_r} = \boldsymbol{\tau}_c \tag{5.12}$$

where $\boldsymbol{M} = \boldsymbol{M}_{rb} + \boldsymbol{M}_A$ and $\boldsymbol{C}(\boldsymbol{\nu}) = \boldsymbol{C}_{rb}(\boldsymbol{\nu}) + \boldsymbol{C}_A(\boldsymbol{\nu})$ are the translational and rotational rigid-body dynamics with correlating added mass effects. Hydrodynamic forces and moments are included in the damping matrix $\boldsymbol{D}(\boldsymbol{\nu})$. Control forces and moments which acts on the vessel are defined by $\boldsymbol{\tau}_c = \boldsymbol{B}\boldsymbol{\mathcal{K}}\boldsymbol{f} = [\tau_u, 0, \tau_r]^T$, where $\boldsymbol{B} \in \mathrm{R}^{3\times 2}$ is the actuator configuration matrix which maps the control inputs (thruster revolutions) $\boldsymbol{f} = [T_u, 0, T_r]^T$ into surge forces and yaw moments. $\boldsymbol{\mathcal{K}} \in \mathrm{R}^{3\times 3}$ is the diagonal force coefficient matrix. We have the following modelling considerations for the matrices $\boldsymbol{M}, \boldsymbol{C}, \boldsymbol{B}, \boldsymbol{D}$:

$$
\begin{aligned}
\boldsymbol{M} &\triangleq \begin{bmatrix} m_{11} & 0 & 0 \\ 0 & m_{22} & m_{23} \\ 0 & m_{32} & m_{33} \end{bmatrix}, \; \boldsymbol{B} \triangleq \begin{bmatrix} b_{11} & b_{12} \\ 0 & 0 \\ b_{31} & b_{32} \end{bmatrix} \\
\boldsymbol{C} &\triangleq \begin{bmatrix} 0 & 0 & c_{13} \\ 0 & 0 & c_{23} \\ c_{31} & c_{32} & 0 \end{bmatrix}, \quad \boldsymbol{D} \triangleq \begin{bmatrix} d_{11} & 0 & 0 \\ 0 & d_{22} & d_{23} \\ 0 & d_{32} & d_{33} \end{bmatrix}
\end{aligned}
\tag{5.13}
$$

Following assumption 3.1 we have two *nonrotable* aft thrusters which imply that the control allocation problem is trivial and unconstrained. If we reduce $\boldsymbol{B}, \boldsymbol{\mathcal{K}}, \boldsymbol{\tau}_c$ to $\in \mathrm{R}^{2\times 2}$ we can compute the control inputs as

$$
\boldsymbol{f} = \boldsymbol{\mathcal{K}}^{-1} \, \boldsymbol{B}^{-1} \, \boldsymbol{\tau}_c = [T_u, T_r]^T \tag{5.14}
$$

Following [79] we can derive the kinematic and dynamic equations derived in eq. 5.2 into component form. Consequently, we have the following equations of motion:

$$\begin{aligned}
\dot{x} =& u_r \cdot c(\psi) - v_r \cdot s(\psi) + V_x \\
\dot{y} =& v_r \cdot s(\psi) - v_r \cdot c(\psi) + V_y \\
\dot{\psi} =& r \\
\dot{r} =& F_r(u_r, v_r, r) + \tau_r \\
\dot{u}_r =& F_{u_r}(v_r) + \tau_u \\
\dot{v}_r =& X(u_r) + Y(u_r) \cdot v_r
\end{aligned} \tag{5.15}$$

We have that $X(u_r) = -X_1 \cdot u_r + X_2$, $Y(u_r) = -Y_1 \cdot u_r - Y_2$. From assumption 3.5 we assume that $X(u_r)$ and $Y(u_r)$ are linear functions. The terms $F_{u_r}(u_r), X(u_r), Y(u_r), F_r(u_r, v_r, r)$ are defined in [79], yielding

$$\begin{aligned}
F_{u_r}(v_r, r) \triangleq& \frac{1}{m_{11}} \left(m_{22}\, v_r + m_{23}\, r\right) r - \frac{d_{11}}{m_{11}}\, u_r \\
X(u_r) \triangleq& - \frac{m_{11}\, m_{33} - m_{23}^2}{m_{22}\, m_{33} - m_{23}^2}\, u_r + \frac{d_{33}\, m_{23} - d_{23}\, m_{33}}{m_{22}\, m_{33} - m_{23}^2} \\
Y(u_r) \triangleq& - \frac{(m_{11} - m_{22})\, m_{23}}{m_{22}\, m_{33} - m_{23}^2}\, u_r - \frac{d_{22}\, m_{33} - d_{32}\, m_{23}}{m_{22}\, m_{33} - m_{23}^2} \\
F_r(u_r, v_r, r) \triangleq& \frac{m_{23}\, d_{22} - m_{22}(d_{32} + (m_{22} - m_{11})\, u_r)}{m_{22}\, m_{33} - m_{23}^2} \cdot v_r \\
&+ \frac{m_{23}(d_{23} + m_{11}\, u_r) - m_{22}(d_{33} + m_{23}\, u_r)}{m_{22}\, m_{33} - m_{23}^2}\, r
\end{aligned} \tag{5.16}$$

Remark 6.1 *The terms $Y(u_r)$ and $X(u_r)$ are assumed to be linear. Furthermore, $Y(u_r)$ have the following bounds:*

$$\frac{(m_{11} - m_{22})\, m_{23}}{m_{22}\, m_{33} - m_{23}^2}\, u_r > 0, \qquad \frac{d_{22}\, m_{33} - d_{32}\, m_{23}}{m_{22}\, m_{33} - m_{23}^2} > 0 \tag{5.17}$$

5.2.1 Control objective

The control objective for the USV is to track a moving vehicle whose future path is not known. The target tracking error is defined by $\boldsymbol{e}_d = [x_d, y_d, \psi_d, u_d]^T$, where $\boldsymbol{e}_d$ represents the desired planar position, heading and surge velocity. Furthermore, we want to relax the following conditions

$$\begin{aligned} &\lim_{t\to\infty}(x - x_t) = 0, \quad \lim_{t\to\infty}(y - y_t) = 0 \\ &\lim_{t\to\infty}(\psi - \psi_d) = 0, \quad \lim_{t\to\infty}(u - u_d) = 0 \end{aligned} \tag{5.18}$$

Remark 3.1 *The control objectives implies that the control problem is underactuated as we aim to control 4DOF with only two control inputs* $\boldsymbol{u} \in \mathrm{R}^2$. *Considering assumption 2.2, that the vessel is always tracking a moving target with a speed* $U_t^n(t) = \sqrt{\dot{x}_t^2(t) + \dot{y}_t^2(t)} > 0 \,\forall\, t$, *dynamic positioning scenarios are neglected.*

5.2.2 Control System

As described in section 2, the CB guidance law is decomposed into surge and heading controllers. We assume that the surge-sway dynamics are decoupled, such that two model-based feedforward PI and PID controllers for surge and the heading can be implemented. Following [36] we can linearize the maneuvering model in eq. 5.2 to 1DOF heading and surge subsystems (*Nomoto models*). Given the control errors $\hat{u} = (u - u_d)$ and $\hat{\psi} = (\psi - \psi_d)$, the surge PI controller and heading PID autopilot are given as

$$\begin{aligned} \tau_u =& (m - X_{\dot{u}})\,\dot{u} + X_u\, u_d - k_{p_u}\,\hat{u} - k_{i_u}\int_0^t \hat{u}(\tau)\,d\tau \\ \tau_r =& (I_z - N_{\dot{r}})\,\ddot{\psi}_d + N_r\,\dot{\psi} - k_{p_\psi}\,\hat{\psi} - k_{d_\psi}\,\dot{\hat{\psi}} - K_{i_\psi}\int_0^t \hat{\psi}(\tau)\,d\tau \end{aligned} \tag{5.19}$$

where $X_{\dot{u}}, X_u, N_{\dot{r}}, N_r$ are the hydrodynamic damping forces/moments and their derivatives (added mass) in surge and yaw and m and I_z are the vehicle mass and inertia

(vertical component) respectively.

5.3 Simulation & Results

5.3.1 Case 1

The first case study presents a scenario where the underwater glider is performing a vertical spiral, which in the horizontal plane results in a circle. The initial conditions of the Otter USV was $[x_0, y_0, \psi_0] = [-100\ m, 50\ m, 0\ rad]^T$ meters from the initial position of the underwater glider.

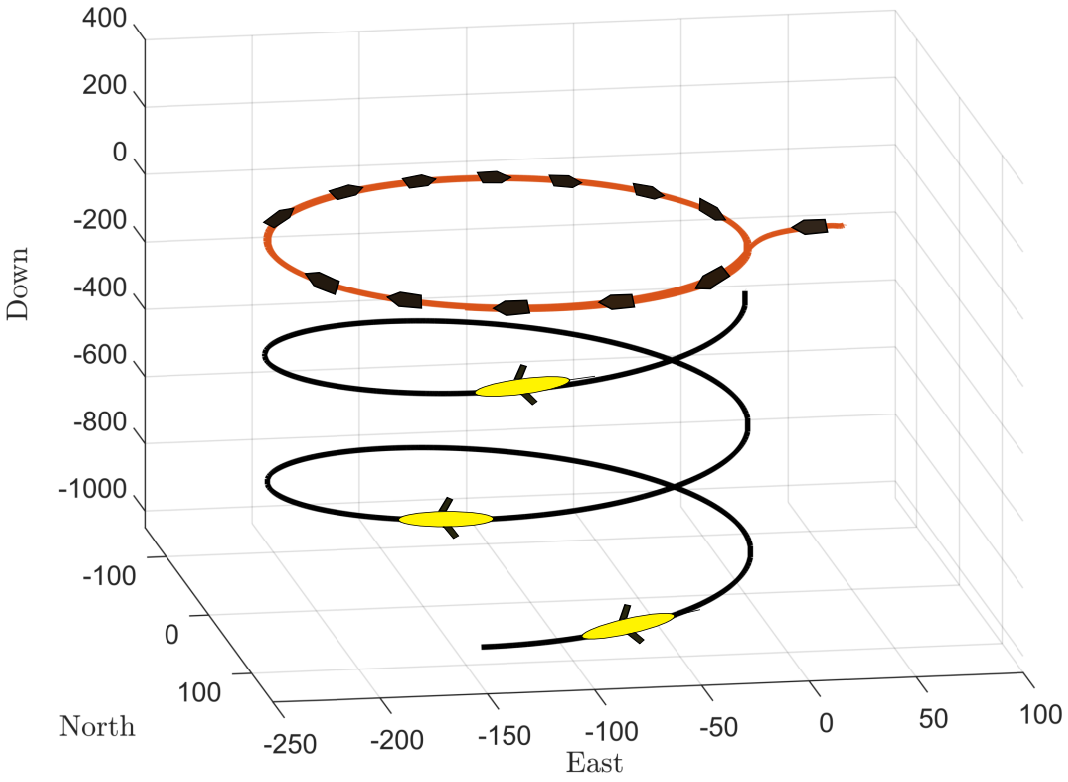

Figure 5.2: Target tracking - Vertical spiral

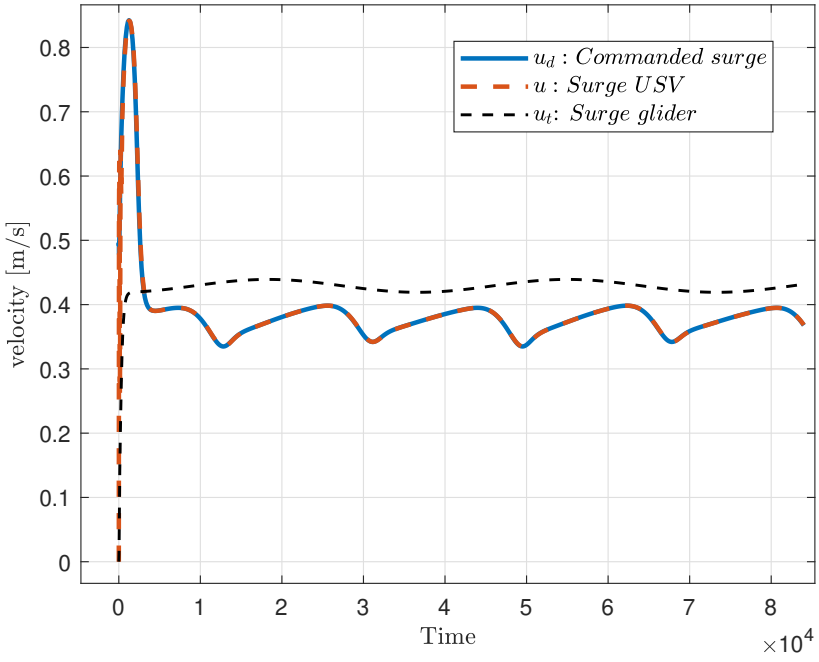

Figure 5.3: Case 1 - Surge control

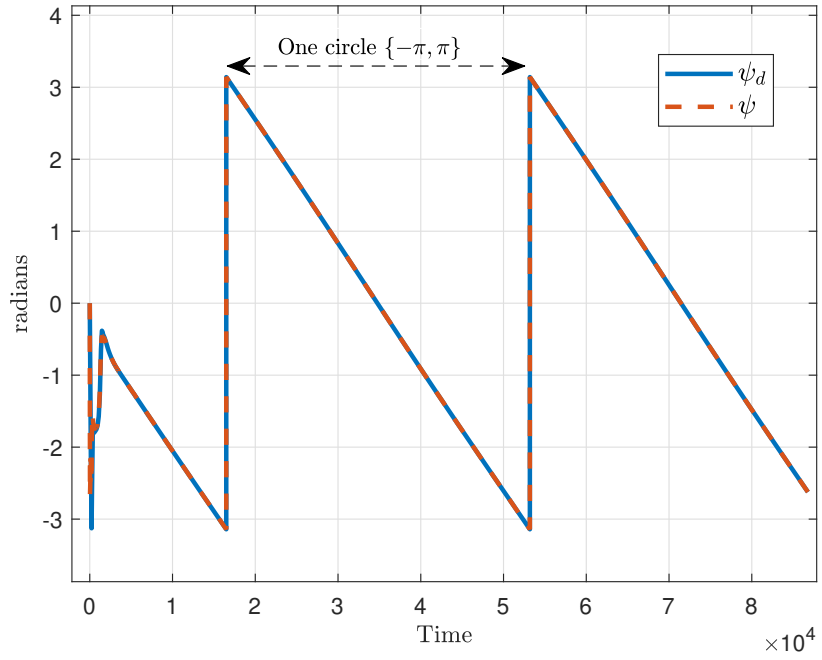

Figure 5.4: Case 1 - Surge control

5.3.2 Case 2

The second case study presents a scenario when the glider is conducting a classical saw-tooth motion. This is considered a *Wings-leveled* trajectory where there sway dynamics is relaxed. In the horizontal plane, the glider trajectory is a straight line. The initial conditions for the vessel were $[x_0, y_0, \psi_0] = [-100\ m, -35\ m, \pi/2\ rad]$

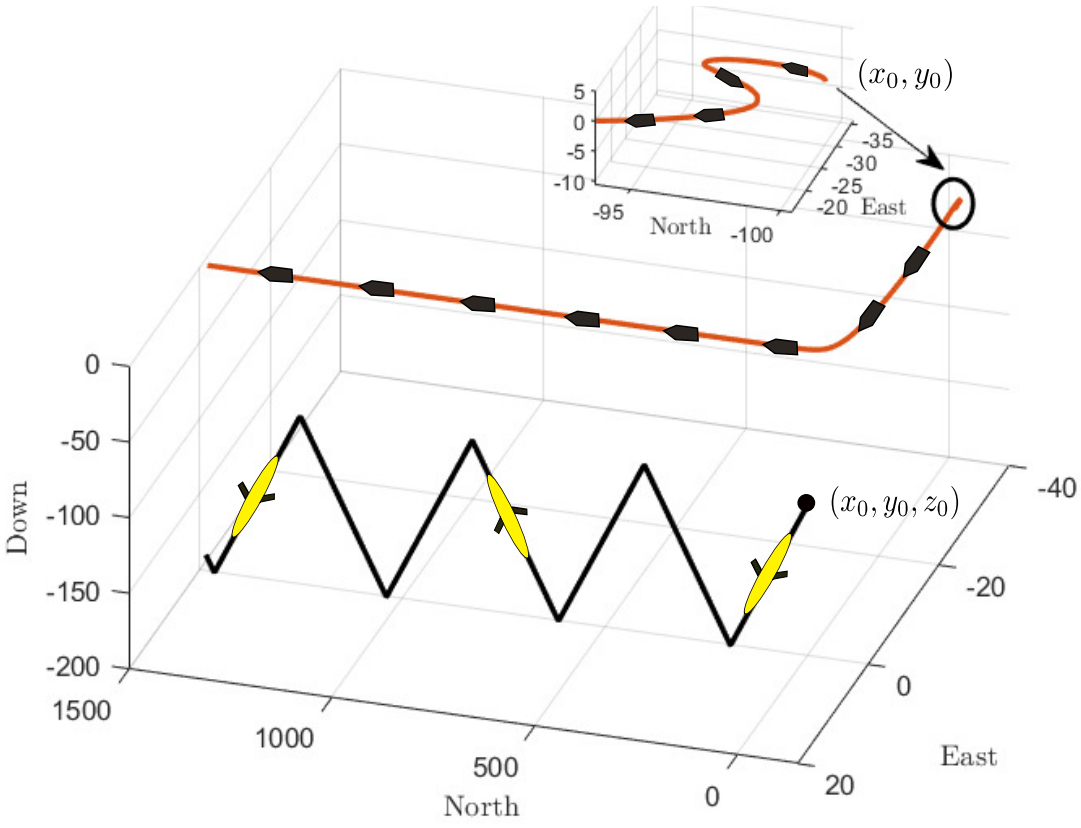

Figure 5.5: Target tracking - Saw-tooth motion

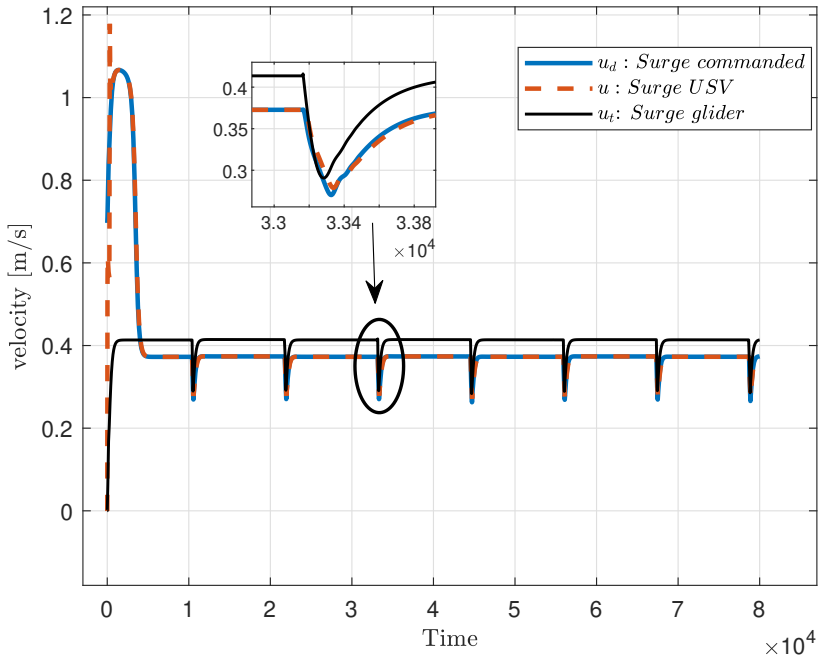

Figure 5.6: Velocity control

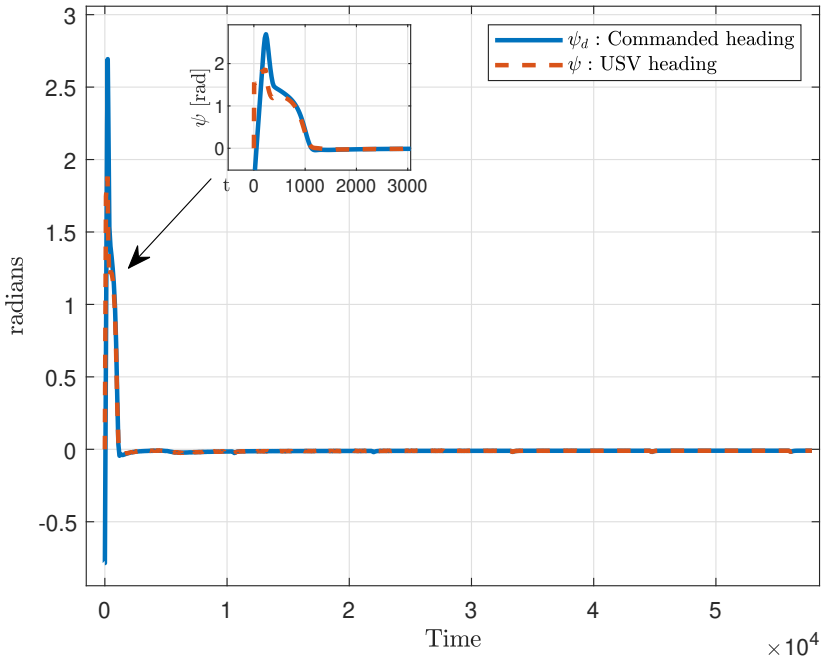

Figure 5.7: Velocity control

5.4 Further Work

The further steps are to validate the proposed target tracking scheme with experimental tests. The aim is to use an Otter USV owned by the ocean laboratory (Oceanlab) at Oslo Metropolitan University in Oslo, Norway. The vessel is complemented by a short baseline (SBL) acoustic positioning system from Waterlinked. An acoustic receiver antenna is mounted on the vessel and submerged approximately 0.5-1 meters. A small omnidirectional acoustic locator (32 x 121 mm) is mounted on the underwater vehicle to transmit range measurements to the topside vessel.

Figure 5.8: Oceanlab's Otter USV equipped with Waterlinked SBL (short baseline) acoustic positioning system, courtesy of OsloMet

5.5 Stability Considerations

This section presents a Lyapunov stability analysis target tracking objective $\hat{\boldsymbol{P}}_n = \boldsymbol{P}_u^n - \boldsymbol{P}_t^n \in \mathrm{R}^2$. Following [11,36] we define the Lyapunov function candidate (LFC) as:

$$V = \frac{1}{2} \cdot (\hat{\boldsymbol{P}}_n)^T \cdot \hat{\boldsymbol{P}}_n, \;\; \forall \, \hat{\boldsymbol{P}}_n \neq \boldsymbol{0} \tag{5.20}$$

We differentiate 5.20 with respect time yielding

$$\dot{V} = (\hat{\boldsymbol{P}}_n)^T \cdot \hat{\boldsymbol{\nu}}_n \tag{5.21}$$

where $\hat{\boldsymbol{\nu}}_n = \boldsymbol{\nu}_t^n - \boldsymbol{\nu}_u^n$ is the difference between the target and interceptor velocities respectively. Furthermore, we assume that the topside vessel velocity is perfectly tracked $\boldsymbol{\nu_u^n = \nu_d^n}$, such that $\hat{\boldsymbol{\nu}}_n$ is rewritten as

$$\hat{\boldsymbol{\nu}}_n = \boldsymbol{\nu}_t^t - \boldsymbol{\nu}_d^n + \tilde{\boldsymbol{\nu}}_n \tag{5.22}$$

where $\tilde{\boldsymbol{\nu}}_n = \boldsymbol{\nu}_d^n - \boldsymbol{\nu}_u^n$. Furthermore, we expand $\boldsymbol{\nu}_d^n$ which yields

$$\hat{\boldsymbol{\nu}}_n = -\bar{U}_a \cdot \frac{\hat{\boldsymbol{P}}}{\sqrt{(\hat{P}_n)^T \cdot \hat{\boldsymbol{P}}_n + \Lambda^2}} + \tilde{\boldsymbol{\nu}}_n \tag{5.23}$$

Assuming that the velocity objective $\tilde{\boldsymbol{\nu}}_n$ is perfectly tracked yields

$$\dot{V} = -\bar{U}_a \cdot \frac{(\hat{\boldsymbol{P}}_n)^T \cdot \hat{\boldsymbol{P}}_n}{\sqrt{(\hat{\boldsymbol{P}}_n)^T \cdot \hat{\boldsymbol{P}}_n + \Lambda^2}} \tag{5.24}$$

where the maximum approach speed $\bar{U}_a$ and transient parameter Λ are both larger than zero, which imply that eq. 5.24 is negative definite [11]. Hence, the origin of $\hat{\boldsymbol{P}}_n$ is uniformly globally asymptotically stable (UGAS) according to the nonlinear stability theory in [54].

Chapter 6

Discussion & Further Work

In this chapter we discuss the theory and results from the main topics in this thesis - Modelling, control, navigation, path-following, and target tracking. Finally, recommendations for further improvements are proposed.

6.1 Modelling and Control

The dynamic model of the buoyancy driven underwater glider and attitude and heading control was presented in chapter 2. The simulated model is used throughout the thesis to validate guidance, navigation and target tracking schemes. In some sections of the extensive model, there are rough simplifications, particularly related to actuator modelling that consists of simple saturation models to reflect the time-delayed dynamics of the VBS and moving mass systems. Additionally, the coupled dynamics between the glider body and moving mass is neglected, which in previous works have been included [42, 62, 106]. We argue that these effects are neglectable for the purpose of validating model-free control systems and observers. However, this is just an assumption that is not prior to any empirical observations/knowledge.

To reflect real ocean conditions, ocean current disturbances were introduced in the dynamic glider model. Following previous works [16, 36, 79, 103], the ocean current dis-

turbances were defined by planar current components that were considered irrotational and constant in the inertial reference frame. However, in slowly moving buoyancy propelled gliders, the ocean currents tend to change over time due to perpetual forces, e.g., tidals. To make the simulation more realistic, the planar ocean current components $\boldsymbol{V}_c^n = [V_x^n, V_y^n, 0]^T$ could be varying with respect to the depth of the glider, such that $\boldsymbol{V}_c^n(z) = [V_x^n(z), V_y^n(z), 0]^T$

For further development of the glider model, investigating the performance of the dynamic model versus experimental data may be convenient to ensure merit in control, path-following and navigation systems. Additionally, for longer simulation experiments, tidal models could be added to the ocean current model (e.g., harmonic sine equation).

6.2 Navigation

A data-driven approach to dead-reckoning navigation was proposed in chapter 3 for the simulated glider and the Tethys hybrid AUV/glider. Ground truth simulated velocities and measured bottom-lock DVL velocities were used as a reference in sequential learning. As the experiments with the Tethys AUV were conducted with a LinkQuest DVL attached to the vehicle, which have a weight and impose hydrodynamic drag, the proposed velocity observers were not tested without the DVL. Accordingly, we do not have any empirical evidence of the neural network observers when the DVL is detached from the vehicle, which would assumably cause some deviation in the velocity estimation. One solution to this issue could be to create a *Dummy* DVL which contains the same weight and hydrodynamic shape of the actual sensor.

Further work may investigate the performance of the neural networks when the DVL is removed from the vehicle. To improve the neural network performance, an analysis of the selected input variables could be proposed. In [88] a mutual information analysis of the network inputs are considered to find the inputs that are most dependent on the

output, and thereby improving network generalization.

6.3 Guidance

Chapter 4 presents planar motion LOS and ILOS path-following controllers for the buoyancy driven underwater glider. The performance of the two guidance laws are highly dependent of the accuracy of the navigation system. We show that the glider path is relatively close to the desired path when using the DL navigation system from chapter 3. Surprisingly, the difference between ILOS and LOS guidance is very small when the DL navigation system is used, while significant when the ground truth north and east positions are used as feedback. The mean cross-track error $\bar{y}_e$ is almost uniform when applying different ocean current magnitudes and directions, implying that the guidance laws are adaptable to different ocean current scenarios.

Further work may investigate more closely the relationship between the navigation errors and path convergence. Improvements of the planar-motion guidance system is mostly dependent upon the navigation system, but tuning the path-following control parameters Λ and σ_{int} may give better control responses.

6.4 Target tracking

The final topic in this thesis is target-tracking of underwater gliders. A topside vessel is assumed to be equipped with an acoustic positioning system to bound the planar distance to the target (underwater glider). The proposed constant bearing guidance law originates from airborne missile systems, in which the objective is to intercept a target. The need to intercept the planar distance of the glider is not our end goal, but simply keeps the topside vessel within range such that the acoustic positioning system is able to get sufficient measurements. However, the waterlinked SBL system, that is recommended to use in sea-trials, claims to have an operating radius of 300

meters, where interception is not necessary. It may be more convenient to create a target-tracking control system that is more power-efficient where its objective is to stay within the 300 meter radius. Further work may look into optimal control strategies e.g., MPC (model predictive control), LQR (linear quadratic control) etc. For example, when the glider is performing a vertical spiral, the topside vessel could rather perform a station-keeping mode instead of following the circular motion of the target. In this way, the topside vessel reduces its net power consumption.

Bibliography

[1] I. Abraham and J. Yi. Model predictive control of buoyancy propelled autonomous underwater glider. In *2015 American Control Conference (ACC)*, pages 1181–1186. IEEE, 2015.

[2] E. Alpaydin. *Introduction to machine learning*. MIT press, 2020.

[3] M. L. Anastasios. Guidance and path-planning systems for autonomous vehicles. *PhD thesis*, 2014.

[4] D. Aragon, S. Glenn, T. Miles, and R. Curry. Glider performance during hurricane gonzalo. In *OCEANS 2015-MTS/IEEE Washington*, pages 1–5. IEEE, 2015.

[5] A. Bahr, J. J. Leonard, and M. F. Fallon. Cooperative localization for autonomous underwater vehicles. *The International Journal of Robotics Research*, 28(6):714–728, 2009.

[6] P. Baldi and P. J. Sadowski. Understanding dropout. *Advances in neural information processing systems*, 26, 2013.

[7] E. BELGE, K. Hızır, A. PARLAK, A. ALTAN, and R. HACIOĞLU. Estimation of small unmanned aerial vehicle lateral dynamic model with system identification approaches. *Balkan Journal of Electrical and Computer Engineering*, 8(2):121–126, 2020.

[8] J. G. Bellingham, Y. Zhang, J. E. Kerwin, J. Erikson, B. Hobson, B. Kieft, M. Godin, R. McEwen, T. Hoover, J. Paul, et al. Efficient propulsion for the tethys

long-range autonomous underwater vehicle. In *2010 IEEE/OES Autonomous Underwater Vehicles*, pages 1–7. IEEE, 2010.

[9] E. Borhaug, A. Pavlov, and K. Y. Pettersen. Integral los control for path following of underactuated marine surface vessels in the presence of constant ocean currents. In *2008 47th IEEE Conference on Decision and Control*, pages 4984–4991. IEEE, 2008.

[10] I.-L. G. Borlaug, K. Y. Pettersen, and J. T. Gravdahl. Tracking control of an articulated intervention autonomous underwater vehicle in 6dof using generalized super-twisting: Theory and experiments. *IEEE Transactions on Control Systems Technology*, 29(1):353–369, 2020.

[11] M. Breivik. Topics in guided motion control of marine vehicles. 2010.

[12] M. Breivik and T. I. Fossen. Applying missile guidance concepts to motion control of marine craft. *IFAC Proceedings Volumes*, 40(17):349–354, 2007.

[13] M. Breivik and T. I. Fossen. Guidance laws for autonomous underwater vehicles. *Underwater vehicles*, 4:51–76, 2009.

[14] M. Breivik, V. E. Hovstein, and T. I. Fossen. Straight-line target tracking for unmanned surface vehicles. 2008.

[15] M. Breivik and J.-E. Loberg. A virtual target-based underway docking procedure for unmanned surface vehicles. *IFAC Proceedings Volumes*, 44(1):13630–13635, 2011.

[16] W. Caharija, K. Y. Pettersen, M. Bibuli, P. Calado, E. Zereik, J. Braga, J. T. Gravdahl, A. J. Sørensen, M. Milovanović, and G. Bruzzone. Integral line-of-sight guidance and control of underactuated marine vehicles: Theory, simulations, and experiments. *IEEE Transactions on Control Systems Technology*, 24(5):1623–1642, 2016.

[17] J. Cao, J. Cao, Z. Zeng, and L. Lian. Nonlinear multiple-input-multiple-output adaptive backstepping control of underwater glider systems. *International Journal of Advanced Robotic Systems*, 13(6):1729881416669484, 2016.

[18] J.-l. Cao, B.-h. Yao, and L. Lian. Nonlinear pitch control of an underwater glider based on adaptive backstepping approach. *Journal of Shanghai Jiaotong University (Science)*, 20(6):729–734, 2015.

[19] D. Chang, F. Zhang, and C. R. Edwards. Real-time guidance of underwater gliders assisted by predictive ocean models. *Journal of Atmospheric and Oceanic Technology*, 32(3):562–578, 2015.

[20] J. E. da Silva, B. Terra, R. Martins, and J. B. de Sousa. Modeling and simulation of the lauv autonomous underwater vehicle. In *13th IEEE IFAC international conference on methods and models in automation and robotics*, volume 1. Szczecin, Poland Szczecin, Poland, 2007.

[21] O. de Fommervault, F. Besson, L. Beguery, Y. Le Page, and P. Lattes. seaexplorer underwater glider: A new tool to measure depth-resolved water currents profiles. In *OCEANS 2019-Marseille*, pages 1–6. IEEE, 2019.

[22] J. Diebel. Representing attitude: Euler angles, unit quaternions, and rotation vectors. *Matrix*, 58(15-16):1–35, 2006.

[23] R. Domingues, G. Goni, F. Bringas, S.-K. Lee, H.-S. Kim, G. Halliwell, J. Dong, J. Morell, and L. Pomales. Upper ocean response to hurricane gonzalo (2014): Salinity effects revealed by targeted and sustained underwater glider observations. *Geophysical Research Letters*, 42(17):7131–7138, 2015.

[24] Y. Duan, L. Yisheng, and F.-Y. Wang. Travel time prediction with lstm neural network. In *2016 IEEE 19th international conference on intelligent transportation systems (ITSC)*, pages 1053–1058. IEEE, 2016.

[25] Z. Duguid and R. Camilli. Improving resource management for unattended observation of the marginal ice zone using autonomous underwater gliders. *Frontiers in Robotics and AI*, 7:184, 2021.

[26] Efunda. Properties of solids. https://www.efunda.com/math/solids/solids_display.cfm?SolidName=HalfCircularCylinder, 2021. Online; accessed 02 June 2021.

[27] M. Eichhorn, H. C. Woithe, and U. Kremer. Comparison of guidance modes for the auv "slocum glider" in time-varying ocean flows. In *OCEANS 2014-TAIPEI*, pages 1–9. IEEE, 2014.

[28] M. Elkolali, A. Al-Tawil, and A. Alcocer. Design and testing of a miniature variable buoyancy system for underwater vehicles. *IEEE Access*, 2022.

[29] T. Elmokadem, M. Zribi, and K. Youcef-Toumi. Trajectory tracking sliding mode control of underactuated auvs. *Nonlinear Dynamics*, 84(2):1079–1091, 2016.

[30] P. Encarnaçao and A. Pascoal. Combined trajectory tracking and path following: an application to the coordinated control of autonomous marine craft. In *Proceedings of the 40th IEEE Conference on Decision and Control (Cat. No. 01CH37228)*, volume 1, pages 964–969. IEEE, 2001.

[31] C. C. Eriksen, T. J. Osse, R. D. Light, T. Wen, T. W. Lehman, P. L. Sabin, J. W. Ballard, and A. M. Chiodi. Seaglider: A long-range autonomous underwater vehicle for oceanographic research. *IEEE Journal of oceanic Engineering*, 26(4):424–436, 2001.

[32] T. Fossen and A. Ross. Nonlinear modelling, identification and control of uuvs. *IEE Control Engineering Series*, 69:13, 2006.

[33] T. I. Fossen. *Nonlinear modelling and control of underwater vehicles*. Fakultet for informasjonsteknologi, matematikk og elektroteknikk, 1991.

[34] T. I. Fossen. Guidance and control of ocean vehicles. *University of Trondheim, Norway, Printed by John Wiley & Sons, Chichester, England, ISBN: 0 471 94113 1, Doctors Thesis*, 1999.

[35] T. I. Fossen. Marine control systems–guidance. navigation, and control of ships, rigs and underwater vehicles. *Marine Cybernetics, Trondheim, Norway, Org. Number NO 985 195 005 MVA, www. marinecybernetics. com, ISBN: 82 92356 00 2*, 2002.

[36] T. I. Fossen. *Handbook of marine craft hydrodynamics and motion control*. John Wiley & Sons, 2011.

[37] T. I. Fossen. Mathematical models of ships and underwater vehicles. In *Encyclopedia of systems and control*, pages 1–1. Springer, 2015.

[38] T. I. Fossen, M. Breivik, and R. Skjetne. Line-of-sight path following of underactuated marine craft. *IFAC proceedings volumes*, 36(21):211–216, 2003.

[39] T. I. Fossen and O.-E. Fjellstad. Nonlinear modelling of marine vehicles in 6 degrees of freedom. *Mathematical Modelling of Systems*, 1(1):17–27, 1995.

[40] S. Glenn, O. Schofield, J. Kohut, J. McDonnell, R. Ludescher, D. Seidel, D. Aragon, T. Haskins, E. Handel, C. Haldeman, et al. The trans-atlantic slocum glider expeditions: A catalyst for undergraduate participation in ocean science and technology. *Marine Technology Society Journal*, 45(1):52–67, 2011.

[41] J. G. Graver. Underwater gliders: Dynamics, control and design. 2005.

[42] J. G. Graver, R. Bachmayer, N. E. Leonard, and D. M. Fratantoni. Underwater glider model parameter identification. In *Proc. 13th Int. Symp. on Unmanned Untethered Submersible Technology (UUST)*, volume 1, pages 12–13, 2003.

[43] J. G. Graver and N. E. Leonard. Underwater glider dynamics and control. In *12th international symposium on unmanned untethered submersible technology*, pages 1742–1710. Citeseer, 2001.

[44] N. Gupta. Artificial neural network. *Network and Complex Systems*, 3(1):24–28, 2013.

[45] E. G. Hemingway and O. M. O'Reilly. Perspectives on euler angle singularities, gimbal lock, and the orthogonality of applied forces and applied moments. *Multibody System Dynamics*, 44(1):31–56, 2018.

[46] B. W. Hobson, J. G. Bellingham, B. Kieft, R. McEwen, M. Godin, and Y. Zhang. Tethys-class long range auvs-extending the endurance of propeller-driven cruising auvs from days to weeks. In *2012 IEEE/OES autonomous underwater vehicles (AUV)*, pages 1–8. IEEE, 2012.

[47] N. T. Hung, N. Crasta, D. Moreno-Salinas, A. M. Pascoal, and T. A. Johansen. Range-based target localization and pursuit with autonomous vehicles: An approach using posterior crlb and model predictive control. *Robotics and Autonomous Systems*, 132:103608, 2020.

[48] N. T. Hung, F. F. Rego, and A. M. Pascoal. Cooperative distributed estimation and control of multiple autonomous vehicles for range-based underwater target localization and pursuit. *IEEE Transactions on Control Systems Technology*, 2021.

[49] I.B Saksvik. A machine learning approach to dead-reckoning navigation for autonomus underwater vehicles. https://www.dropbox.com/s/ia45ya4m3c89c1z/A%20Machine%20Learning%20Approach%20To%20Dead-Reckoning%20Navigation%20of%20Autonomus%20Underwater%20Vehicles.pdf?dl=0, 2021. Online; accessed 02 June 2021.

[50] I.B Saksvik, S.Blomdal, E. Kirkvik. A ROS Gazebo simulator framework fo an underwater glider. https://www.dropbox.com/s/k82dyjhqr3ane2s/A_ROS_Gazebo_Simulator_Framework_for_an_Underwater_Glider.pdf?dl=0, 2021. Online; accessed 02 June 2021.

[51] K. Isa and M. R. Arshad. Neural networks control of hybrid-driven underwater glider. In *2012 Oceans-Yeosu*, pages 1–7. IEEE, 2012.

[52] K. Isa and M. R. Arshad. An analysis of homeostatic motion control system for a hybrid-driven underwater glider. In *2013 IEEE/ASME International Conference on Advanced Intelligent Mechatronics*, pages 1570–1575. IEEE, 2013.

[53] A. Jing, Z. Tang, J. Gao, and G. Pan. An improved ddpg reinforcement learning control of underwater gliders for energy optimization. In *2020 3rd International Conference on Unmanned Systems (ICUS)*, pages 621–626. IEEE, 2020.

[54] H. K. Khalil. Nonlinear systems. 2002.

[55] A. M. Lekkas and T. I. Fossen. Line-of-sight guidance for path following of marine vehicles. *Advanced in marine robotics*, pages 63–92, 2013.

[56] A. M. Lekkas and T. I. Fossen. Line-of-sight guidance for path following of marine vehicles. *Advanced in marine robotics*, pages 63–92, 2013.

[57] W. Li, M. Chen, C. Zhang, L. Zhang, and R. Chen. A novel neural network-based sins/dvl integrated navigation approach to deal with dvl malfunction for underwater vehicles. *Mathematical Problems in Engineering*, 2020, 2020.

[58] L. Ljung. System identification. In *Signal analysis and prediction*, pages 163–173. Springer, 1998.

[59] L. Ljung, C. Andersson, K. Tiels, and T. B. Schön. Deep learning and system identification. *IFAC-PapersOnLine*, 53(2):1175–1181, 2020.

[60] N. Mahmoudian. *Efficient motion planning and control for underwater gliders*. PhD thesis, Virginia Tech, 2009.

[61] N. Mahmoudian and C. Woolsey. Underwater glider motion control. In *2008 47th IEEE Conference on Decision and Control*, pages 552–557. IEEE, 2008.

[62] N. Mahmoudian and C. Woolsey. Underwater glider motion control. In *2008 47th IEEE Conference on Decision and Control*, pages 552–557. IEEE, 2008.

[63] M. M. M. Manhães, S. A. Scherer, M. Voss, L. R. Douat, and T. Rauschenbach. Uuv simulator: A gazebo-based package for underwater intervention and multi-robot simulation. In *OCEANS 2016 MTS/IEEE Monterey*, pages 1–8. IEEE, 2016.

[64] A. B. Martinsen and A. M. Lekkas. Straight-path following for underactuated marine vessels using deep reinforcement learning. *IFAC-PapersOnLine*, 51(29):329–334, 2018.

[65] I. Masmitja, S. Gomariz, J. Del-Rio, B. Kieft, T. O'Reilly, P.-J. Bouvet, and J. Aguzzi. Optimal path shape for range-only underwater target localization using a wave glider. *The International Journal of Robotics Research*, 37(12):1447–1462, 2018.

[66] M. Mat-Noh, M. Arshad, and R. Mohd-Mokhtar. Nonlinear control of autonomous underwater glider based on super-twisting sliding mode control (stsmc). In *2017 7th IEEE International Conference on System Engineering and Technology (ICSET)*, pages 71–76. IEEE, 2017.

[67] MATLAB. *Deep Learning Toolbox*. The MathWorks Inc., Natick, Massachusetts, 2019.

[68] MATLAB. *MATLAB Control System Toolbox*. The MathWorks Inc., Natick, Massachusetts, 2019.

[69] MATLAB. *MATLAB System Identification Toolbox*. The MathWorks Inc., Natick, Massachusetts, 2019.

[70] L. Merckelbach, A. Berger, G. Krahmann, M. Dengler, and J. R. Carpenter. A dynamic flight model for slocum gliders and implications for turbulence microstructure measurements. *Journal of Atmospheric and Oceanic Technology*, 36(2):281–296, 2019.

[71] T. Miles, S. H. Lee, A. Wåhlin, H. K. Ha, T. W. Kim, K. M. Assmann, and O. Schofield. Glider observations of the dotson ice shelf outflow. *Deep Sea Research Part II: Topical Studies in Oceanography*, 123:16–29, 2016.

[72] T. Miles, G. Seroka, J. Kohut, O. Schofield, and S. Glenn. Glider observations and modeling of sediment transport in hurricane sandy. *Journal of Geophysical Research: Oceans*, 120(3):1771–1791, 2015.

[73] D. Moreno-Salinas, N. Crasta, M. Ribeiro, B. Bayat, A. Pascoal, and J. Aranda. Integrated motion planning, control, and estimation for range-based marine vehicle positioning and target localization. *IFAC-PapersOnLine*, 49(23):34–40, 2016.

[74] X. Mu, B. He, X. Zhang, Y. Song, Y. Shen, and C. Feng. End-to-end navigation for autonomous underwater vehicle with hybrid recurrent neural networks. *Ocean Engineering*, 194:106602, 2019.

[75] M. J. Nelson, B. Y. Queste, I. J. Smith, G. H. Leonard, B. G. Webber, and K. G. Hughes. Measurements of ice shelf water beneath the front of the ross ice shelf using gliders. *Annals of Glaciology*, 58(74):41–50, 2017.

[76] M. M. Noh, M. R. Arshad, and R. M. Mokhtar. Depth and pitch control of usm underwater glider: performance comparison pid vs. lqr. 2011.

[77] P. Norgren, M. Ludvigsen, T. Ingebretsen, and V. E. Hovstein. Tracking and remote monitoring of an autonomous underwater vehicle using an unmanned sur-

face vehicle in the trondheim fjord. In *OCEANS 2015-MTS/IEEE Washington*, pages 1–6. IEEE, 2015.

[78] C. E. Ordoñez, H. Wang, E. Curtiss, A. Nesheim, T. Thoresen, S. Lampoudi, and R. Craig. Oceanscout-developing a compact, affordable, fleet-capable autonomous glider. In *Global Oceans 2020: Singapore–US Gulf Coast*, pages 1–6. IEEE, 2020.

[79] C. Paliotta, E. Lefeber, K. Y. Pettersen, J. Pinto, M. Costa, et al. Trajectory tracking and path following for underactuated marine vehicles. *IEEE Transactions on Control Systems Technology*, 27(4):1423–1437, 2018.

[80] A. A. Penas. Positioning and navigation systems for robotic underwater vehicles. *Doctor thesis, Instituto Superior Tcnico*, 2009.

[81] T. Prestero. Development of a six-degree of freedom simulation model for the remus autonomous underwater vehicle. In *MTS/IEEE Oceans 2001. An Ocean Odyssey. Conference Proceedings (IEEE Cat. No. 01CH37295)*, volume 1, pages 450–455. IEEE, 2001.

[82] C. Qiu, H. Mao, J. Yu, Q. Xie, J. Wu, S. Lian, and Q. Liu. Sea surface cooling in the northern south china sea observed using chinese sea-wing underwater glider measurements. *Deep Sea Research Part I: Oceanographic Research Papers*, 105:111–118, 2015.

[83] I. B. Saksvik, A. Alcocer, and V. Hassani. A deep learning approach to dead-reckoning navigation for autonomous underwater vehicles with limited sensor payloads. *arXiv preprint arXiv:2110.00661*, 2021.

[84] I. B. Saksvik, A. Alcocer, and V. Hassani. Integral line-of-sight guidance of underactuated underwater gliders. unpublished, 2022.

[85] I. B. Saksvik, A. Alcocer, and V. Hassani. Trajectory tracking & localization of underwater gliders using small unmanned surface vessels (usvs). unpublished, 2022.

[86] J. Sherman, R. E. Davis, W. Owens, and J. Valdes. The autonomous underwater glider" spray". *IEEE Journal of Oceanic Engineering*, 26(4):437–446, 2001.

[87] R. Skejic, M. Breivik, T. I. Fossen, and O. M. Faltinsen. Modeling and control of underway replenishment operations in calm water. *IFAC Proceedings Volumes*, 42(18):78–85, 2009.

[88] R. Skulstad, G. Li, T. I. Fossen, B. Vik, and H. Zhang. Dead reckoning of dynamically positioned ships: Using an efficient recurrent neural network. *IEEE Robotics & Automation Magazine*, 26(3):39–51, 2019.

[89] J. Sliwka, B. Clement, and I. Probst. Sea glider guidance around a circle using distance measurements to a drifting acoustic source. In *2012 IEEE/RSJ International Conference on Intelligent Robots and Systems*, pages 94–99. IEEE, 2012.

[90] T. SNAME. Nomenclature for treating the motion of a submerged body through a fluid. *The Society of Naval Architects and Marine Engineers, Technical and Research Bulletin No*, pages 1–5, 1950.

[91] W. Snyder, L. Van Uffelen, and M. Renken. Effects of incorporating inertial measurements on the localization accuracy of the seaglider auv. In *OCEANS 2019-Marseille*, pages 1–6. IEEE, 2019.

[92] E. Sollesnes, O. M. Brokstad, B. Vågen, A. Carella, A. Alcocer, A. P. Zolich, T. A. Johansen, et al. Towards autonomous ocean observing systems using miniature underwater gliders with uav deployment and recovery capabilities. In *2018 IEEE/OES Autonomous Underwater Vehicle Workshop (AUV)*, pages 1–5. IEEE, 2018.

[93] Z.-q. Su, M. Zhou, F.-f. Han, Y.-w. Zhu, D.-l. Song, and T.-t. Guo. Attitude control of underwater glider combined reinforcement learning with active disturbance rejection control. *Journal of Marine Science and Technology*, 24(3):686–704, 2019.

[94] M. Sundermeyer, R. Schlüter, and H. Ney. Lstm neural networks for language modeling. In *Thirteenth annual conference of the international speech communication association*, 2012.

[95] P. Švec, A. Thakur, E. Raboin, B. C. Shah, and S. K. Gupta. Target following with motion prediction for unmanned surface vehicle operating in cluttered environments. *Autonomous Robots*, 36(4):383–405, 2014.

[96] L. Techy, K. A. Morganseny, and C. A. Woolseyz. Long-baseline acoustic localization of the seaglider underwater glider. In *Proceedings of the 2011 American Control Conference*, pages 3990–3995. IEEE, 2011.

[97] R. E. Todd, D. L. Rudnick, J. T. Sherman, W. B. Owens, and L. George. Absolute velocity estimates from autonomous underwater gliders equipped with doppler current profilers. *Journal of Atmospheric and Oceanic Technology*, 34(2):309–333, 2017.

[98] B. Ullah, M. Ovinis, M. Baharom, S. Ali, and M. Javaid. Pitch and depth control of underwater glider using lqg and lqr via kalman filter. *International Journal of Vehicle Structures & Systems (IJVSS)*, 10(2), 2018.

[99] B. Ullah, M. Ovinis, M. B. Baharom, S. S. A. Ali, B. Khan, and M. Y. Javaid. Effect of waves and current on motion control of underwater gliders. *Journal of Marine Science and Technology*, 25(2):549–562, 2020.

[100] P. Wang, P. K. Singh, and J. Yi. Dynamic model-aided localization of underwater autonomous gliders. In *2013 IEEE International Conference on Robotics and Automation*, pages 5565–5570. IEEE, 2013.

[101] S. E. Webster, C. M. Lee, and J. I. Gobat. Preliminary results in under-ice acoustic navigation for seagliders in davis strait. In *2014 Oceans-St. John's*, pages 1–5. IEEE, 2014.

[102] M. S. Wiig, W. Caharija, T. R. Krogstad, and K. Y. Pettersen. Integral line-of-sight guidance of underwater vehicles without neutral buoyancy. *IFAC-PapersOnLine*, 49(23):590–597, 2016.

[103] M. S. Wiig, W. Caharija, T. R. Krogstad, and K. Y. Pettersen. Integral line-of-sight guidance of underwater vehicles without neutral buoyancy. *IFAC-PapersOnLine*, 49(23):590–597, 2016.

[104] H. C. Woithe, D. Boehm, and U. Kremer. Improving slocum glider dead reckoning using a doppler velocity log. In *OCEANS'11 MTS/IEEE KONA*, pages 1–5. IEEE, 2011.

[105] H. C. Woithe, M. Eichhorn, O. Schofield, and U. Kremer. Assessing automated and human path planning for the slocum glider. In *18th International Symposium on Unmanned Untethered Submersible Technology (UUST 2013)*, 2013.

[106] C. Woolsey and N. E. Leonard. Moving mass control for underwater vehicles. In *Proceedings of the 2002 American Control Conference (IEEE Cat. No. CH37301)*, volume 4, pages 2824–2829. IEEE, 2002.

[107] H. Yang and J. Ma. Sliding mode tracking control of an autonomous underwater glider. In *2010 International Conference on Computer Application and System Modeling (ICCASM 2010)*, volume 4, pages V4–555. IEEE, 2010.

[108] J. Yu, F. Zhang, A. Zhang, W. Jin, and Y. Tian. Motion parameter optimization and sensor scheduling for the sea-wing underwater glider. *IEEE journal of oceanic engineering*, 38(2):243–254, 2013.

[109] J. Yu, F. Zhang, A. Zhang, W. Jin, and Y. Tian. Motion parameter optimization and sensor scheduling for the sea-wing underwater glider. *IEEE journal of oceanic engineering*, 38(2):243–254, 2013.

[110] J.-c. Yu, A.-q. Zhang, W.-m. Jin, Q. Chen, Y. Tian, and C.-j. Liu. Development and experiments of the sea-wing underwater glider. *China Ocean Engineering*, 25(4):721–736, 2011.

[111] Y. Yu, X. Si, C. Hu, and J. Zhang. A review of recurrent neural networks: Lstm cells and network architectures. *Neural computation*, 31(7):1235–1270, 2019.

[112] F.-b. ZHANG, W. Gang, C. Yu-hang, and B. Hong-jie. Modeling and pid control of underwater glider motion. *Torpedo Technology*, 19(2):114–119, 2011.

[113] S. Zhang, J. Yu, A. Zhang, and F. Zhang. Spiraling motion of underwater gliders: Modeling, analysis, and experimental results. *Ocean Engineering*, 60:1–13, 2013.

[114] X. Zhang, B. He, G. Li, X. Mu, Y. Zhou, and T. Mang. Navnet: Auv navigation through deep sequential learning. *IEEE Access*, 8:59845–59861, 2020.

[115] H. Zhou, Z. Wei, Z. Zeng, C. Yu, B. Yao, and L. Lian. Adaptive robust sliding mode control of autonomous underwater glider with input constraints for persistent virtual mooring. *Applied Ocean Research*, 95:102027, 2020.

[116] J. Zhou, D. Ye, J. Zhao, and D. He. Three-dimensional trajectory tracking for underactuated auvs with bio-inspired velocity regulation. *International Journal of Naval Architecture and Ocean Engineering*, 10(3):282–293, 2018.

[117] M. Zhou, R. Bachmayer, and B. deYoung. Towards autonomous underwater iceberg profiling using a mechanical scanning sonar on a underwater slocum glider. In *2016 Ieee/Oes Autonomous Underwater Vehicles (Auv)*, pages 101–107. IEEE, 2016.

**

Appendix A

Seawing Underwater Glider

The following table details the mechanical properties of the Seawing glider that was used in the numerical simulation of the dynamics in MATLAB. The position of the static mass $\boldsymbol{r}_{m_s} \in \mathbb{R}^3$ and net buoyancy $\boldsymbol{r}_{m_b} \in \mathbb{R}^3$ are offset from the center of origin which coincides with the center of buoyancy $\boldsymbol{r}_{cb} = [0, 0, 0]^T \in \mathbb{R}^3$. The latter assumption is convenient as CB is always located at the center of the displaced volume of the glider [41].

Static mass m_s	54.28 kg
Moving/rolling mass m_p	11 kg
Net buoyancy m_b	-0.5 kg $< m_b <$ 0.5 kg
Position of static mass	$\boldsymbol{r}_{m_s}$ = [-0.0814 0 0.0032] m
Position of net buoyancy	$\boldsymbol{r}_{m_b}$ = [0 0 0] m
Inertia of static mass	$\boldsymbol{I}_s$ = diag[0.60 15.27 15.32] kg m^2
Inertia of moving/rolling mass	$\boldsymbol{I}_{m_p}$ = diag[0.02 10.16 0.17] kg m^2

The hydrodynamic forces and moments of the Seawing glider were simulated in a CFD analysis using Reynolds Averaged Navier-Stokes (RANS) equations [113]. Accordingly, the coefficients for the different forces and moments of the glider was estimated. The

following table details the estimated hydrodynamic coefficients of the Seawing glider [113]

$\boldsymbol{D}$	K_{D_0} = 7.19 kg/m	K_D = 386.29 kg/m/rad^2
$\boldsymbol{L}$	K_{L_0} = -0.36 kg/m	K_α = 440.99 kg/m/rad
$\boldsymbol{SF}$	K_β = -115.65 kg/m/rad	
$\boldsymbol{K}$	K_{MR} = -58.27 kg/rad	K_p = -19.83 kg s/rad
$\boldsymbol{M}$	K_{M0} = 0.28 kg	K_q = -205.64 kg s/rad^2
$\boldsymbol{N}$	K_{MY} = 34.10 kg/rad	K_r = -389.30 kg s/rad^2

Addition to the coefficient based hydrodynamic model the added mass coefficients for the seawing glider is presented in [113] as

$$\boldsymbol{M}_A = -diag[1.48,\ 49.58,\ 65.92,\ 0.53,\ 7.88,\ 10.18] \tag{A.1}$$

Appendix B

Paper 1

Path-Following for Underwater Gliders With Limited Navigation Payloads

Ivar Bjørgo Saksvik, Alex Alcocer, Vahid Hassani

Accepted and to be published at the 14th IFAC Conference on Control Applications in Marine Systems, Robotics, and Vehicles (CAMS2022), Kgs. Lyngby, Denmark

Path-Following for Underwater Gliders With Limited Navigation Payloads

Ivar Bjørgo Saksvik * **Alex Alcocer** * **Vahid Hassani** *

* *Department of Mechanical, Electronics and Chemical Engineering, Oslo Metropolitan University, Oslo, Norway (e-mail: s309664@oslomet.no, alepen@oslomet.no, vahid.hassani@oslomet.no).*

Abstract: This paper investigates the performance of *path-following* controllers in underwater gliders that have limited sensor suites. We consider two planar motion guidance laws for the path-following control problem: I) A *line-of-sight* controller, and II) an *integral line-of-sight* controller, where an integral action corrects drifts from unknown ocean current disturbances. The on-board navigation system, which is the main feedback component to the planar motion guidance laws, is aided by two recurrent neural networks (RNN) velocity observers to better approximate the planar position of the glider, using inputs from the limited navigation suite (IMU, pressure sensor, control actions). The performance of the proposed path-following controllers is analysed in a glider simulation with varying ocean current conditions.

Keywords: LOS guidance, Underwater glider, Path-following, Waypoint Guidance.

1. INTRODUCTION

Underwater gliders are fixed-wing autonomous underwater vehicles (AUVs) driven by buoyancy engines. To travel from place to place, gliders change depth continuously by adjusting it's net buoyancy. The combination of vertical profiling and a power-efficient propulsion system have made these vehicles attractive in oceanographic research and monitoring as highlighted in various expeditions Dong et al. (2017), Glenn et al. (2011). Underwater gliders exploits hydrostatic forces (gravity and buoyancy) for locomotion. A set of fixed wings translates the vertical motion into a forward motion. Likewise to many other marine vehicles, gliders are underactuated, that is, the inability to instantly move along it's lateral axis.

Due to the large operating ranges of gliders, a pilot monitors the travel record and determines waypoints in which the vehicle should travel to. The general guidance application is to travel along straight-lines between the predefined waypoints, also referred to as *path-following*. Due to underactuation, the path-following problem is formulated by the *helsman principle*. The vehicle must change it's course while moving forward to follow an arbitrary planar path. From a mathematical perspective, this consists of computing the heading necessary to converge on the path, while maintaining a steady cruising speed. Furthermore, a *low-level* control system (heading controller) is cascaded with the guidance law to bound the heading control error. Note that the path-following problem does not impose any temporal constraints in the control objective, conversely to *trajectory-tracking* which needs to arrive on a path at a specific time.

⋆ This work was supported by the OASYS project funded by the Research Council of Norway (RCN), the German Federal Ministry of Economic Affairs and Energy (BMWi) and the European Commission under the framework of the ERA-NET Cofund MarTERA.

There have been presented many approaches to the path-following control problem for underactuated marine vehicles, mostly by deriving kinematic guidance laws, see Breivik and Fossen (2009), Lekkas and Fossen (2013), Borhaug et al. (2008), Zhou et al. (2016), Wiig et al. (2016), Caharija et al. (2016), but also reinforcement learning methods has been proposed Martinsen and Lekkas (2018). *Legacy gliders* such as Slocum use a velocity vector assignment to compute the heading references for the planar motion case Woithe et al. (2013). This consists of exploiting the velocity vector of the vehicle with respect to the path and optionally using the ocean current vector to compensate for trajectory drifts.

In recent time, *line-of-sight* (LOS) guidance laws have received popularity in various underactuated marine vehicles Lekkas and Fossen (2013), Breivik and Fossen (2009), Zhou et al. (2016). To compensate for environmental loads, e.g, ocean currents, an integral term can be added to the LOS guidance law as presented in Borhaug et al. (2008), Caharija et al. (2016), Wiig et al. (2016). The purpose of the integral action is to bound the drift between the vehicle and the path, usually manifested by a parallel path due to constant or *slowly-changing* ocean currents.

Based on the latter works in line-of-sight and integral line-of-sight based path-following for AUVs and surface vessels, we aim to extend this for underactuated underwater gliders in presence of unknown ocean current disturbances. And, also, investigate the performance of the path-following controllers considering a limited navigation suite with significant dead-reckoning errors.

The remaining parts of this paper are organized as follows:

Manuscript 28 submitted to 14th IFAC Conference on Control Applications in Marine Systems, Robotics, and Vehicles. Received April 21, 2022.

Section 2 presents the planar motion guidance laws for the underactuated underwater glider, *Section 3* and *Section 4* describe a mathematical model of the glider dynamics and control & navigation systems respectively, followed by the simulation results in *section 5*.

2. PLANAR MOTION PATH-FOLLOWING

In this section we derive the *line-of-sight (LOS)* and *integral line-of-sight (ILOS)* guidance laws for the planar motion path-following problem.
The majority of glider missions consists of travelling between geodetic waypoints. The vehicle must occasionally turn when transitioning to a new set of waypoint coordinates. We consider that the path $\mathcal{P}$ is parameterized as a straight line between the predefined waypoints. We can parametarize the straight-line path assuming a scalar $\zeta \in R$ is given so that

$$\mathcal{P} = \begin{bmatrix} x_p \\ y_p \end{bmatrix} = \begin{bmatrix} x_k + \zeta \cdot cos(\xi_p) \\ y_k + \zeta \cdot sin(\xi_p) \end{bmatrix} \tag{1}$$

Where (x_k, y_k) is a fixed location on the path and ξ_p is the angle between the path and the x-axis along the stationary reference frame Breivik and Fossen (2009). Most underwater gliders use internal rotating masses to create a yaw moment by rolling the glider body. The roll motion will force the wings to be non-collinear in the z-axis, causing the glider to enter a vertical spiral/turn. Due to active roll motions, the kinematic equations of the vehicle is derived by all euler angles $\mathbf{\Theta} = [\phi, \theta, \psi]^T$. Note that some gliders (e.g., Slocum) are stable in roll where ϕ can be neglected when describing the kinematics. Following Fossen (2011) the position of the vehicle in the inertial NED (north-east-down) frame is defined as

$$\begin{bmatrix} \dot{x} \\ \dot{y} \end{bmatrix} = \begin{bmatrix} u_r \cdot c(\psi)c(\theta) + v_r \cdot [c(\psi)s(\theta)s(\phi) - s(\psi)c(\phi)] \\ \quad +w_r \cdot [s(\psi)s(\phi) + c(\psi)c(\phi)s(\theta))] + V_x^n \\ \\ u_r \cdot s(\psi)c(\theta) + v \cdot (c(\psi)c(\phi) + s(\phi)s(\theta)s(\psi)) \\ \quad +w \cdot (s(\theta)s(\psi)c(\phi).c(\psi)s(\phi) + V_y^n \end{bmatrix} \tag{2}$$

where $c() = cos()$ and $s() = sin()$. The relative linear velocities are defined as $\boldsymbol{v}_r = [u_r, v_r, w_r]^T = [u - u_c^b, v - v_c^b, w - w_c^b]^T$. Where the ocean current ν_c^b is considered constant and irrotational in the inertial frame.

We start deriving the guidance law by representing the position of the vehicle with respect to the path $\mathcal{P}$. The path is defined by the initial waypoints $(x_k, y_k) \in R^2$ and the consecutive waypoints $(x_{k+1}, y_{k+1}) \in R^2$. The straight-line represented by the two waypoints have a *path-tangential angle* defined as

$$\xi_p = atan2(y_{k+1} - y_k, x_{k+1} - x_k) \tag{3}$$

where *atan2(x,y)* represents the fourth-quadrant of $tan^{-1}(\frac{y}{x}) \in (-\pi/2, \pi/2)$. Following Lekkas and Fossen (2013) we can derive the position of the glider with respect to the fixed path, denoted by the cross-track distance x_e and cross-track error y_e:

$$\begin{aligned} x_e &= (x - x_k) \cdot cos(\xi_p) + (y - y_k) \cdot sin(\xi_p) \\ y_e &= -(x - x_k) \cdot sin(\xi_p) + (y - y_k) \cdot cos(\xi_p) \end{aligned} \tag{4}$$

The time-derivative of the cross-track error y_e is given by

$$\begin{aligned} \dot{y}_e =& - \dot{x} \cdot s(\xi_p) + \dot{y} \cdot c(\xi_p) \\ =& u_r \cdot c(\psi) \cdot c(\theta) \cdot s(\xi_p) + v_r \cdot (c(\psi) \cdot s(\theta) \cdot s(\phi) \\ & - s(\psi) \cdot c(\phi)) \cdot s(\xi_p) + w_r \cdot (s(\psi) \cdot s(\phi) \\ & + c(\psi) \cdot c(\phi) \cdot s(\theta)) \cdot s(\xi_p) + V_x^n + u_r \cdot s(\psi)c(\theta) \cdot c(\xi_p) \\ & + v_r \cdot (c(\psi) \cdot c(\phi) + s(\phi) \cdot s(\theta) \cdot s(\psi)) \cdot c(\xi_p) \\ & + w_r \cdot (s(\theta) \cdot s(\psi) \cdot c(\phi) - c(\phi) \cdot s(\phi)) \cdot c(\xi_p) + V_y^n \end{aligned} \tag{5}$$

Stability proofs of eq. 5 at the equilibrium $y_e = 0$ have been derived for planar LOS and ILOS guidance laws in various literature, see Borhaug et al. (2008), Lekkas and Fossen (2013), Caharija et al. (2016), Breivik and Fossen (2009). We now derive the LOS guidance law which is defined by the kinematic properties previously defined in this section. Given a path-tangential angle ξ_p, cross-track error y_e and a *look-a-head distance* denoted Λ, we derive the planar motion guidance law as

$$\psi_{LOS} = \xi_p + tan^{-1}(\frac{-y_e}{\Lambda}) \tag{6}$$

where $\Lambda > 0$ determines the convergence rate towards the desired path. This is a design parameter (given in meters) that must be tuned correctly. If Λ is too large, the convergence time will be long. If Λ is too small, the convergence rate may be faster than the response of the underactuated vehicle, resulting in oscillating trajectories. The ILOS guidance law is derived as an extension of eq. 6. Following Caharija et al. (2016) and Borhaug et al. (2008), we get

$$\psi_{ILOS} = \xi_p + tan^{-1}(\frac{-y_e}{\Lambda} + k_i \cdot \int_0^t y_e \, dt) \tag{7}$$

In Borhaug et al. (2008) eq. 7 is rewritten to avoid anti-windup effects due to the integral term:

$$\begin{aligned} \psi_{ILOS} &= \xi_p - tan^{-1}(\frac{y_e + k_i \cdot \sigma_{int}}{\Lambda}) \\ \\ \dot{\sigma}_{int} &= \frac{y_e \cdot \Lambda}{\Lambda^2 + (y_e + k_i \cdot \sigma_{int})^2} \end{aligned} \tag{8}$$

where k_i is a design parameter. Equations 8 satisfies the property $\{\dot{\sigma}_{int} \to 0\}$ when $\{y_e \to \infty\}$ Borhaug et al. (2008). Thus, the integration rate is slowed down for large values of y_e, for example when $\psi << \psi_{ILOS}$ which can occur when transitioning between waypoints where $\xi_{p+1} >> \xi_p$.

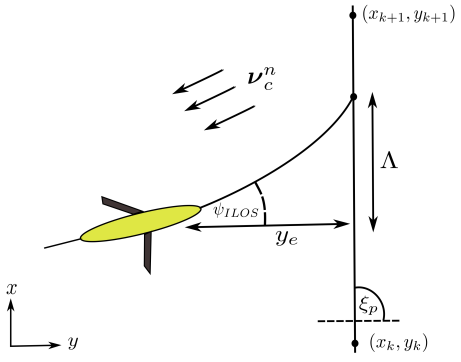

Figure 1. ILOS guidance - 2D view

3. GLIDER DYNAMICS

An underwater glider is characterized as a rigid body (usually torpedo shaped) with fixed wings. A variable buoyancy system (VBS) is exploited to expand and contract the volume that the vehicle is displacing trough an external bladder. This allows the vehicle to sink and rise in the water column, and is the main source of locomotion. The hydrodynamic lift forces acting on the wings ensures that the vertical motion is translated into a forward motion. Due to low dynamic pressure (a result of slow cruising speeds), conventional control surfaces such as rudders and dive planes are replaced by internal translating and rotating masses - often a custom shaped battery-pack located inside the glider housing. This allows the vehicle to create pitch and yaw moments by manipulating the center of gravity CG vector, where the glider body and moving mass system is considered coupled. Before deriving a mathematical model of the glider dynamics, we define some assumptions about the vehicle:

Assumption 4.1: *The center of buoyancy CB* $\in R^3$ *is chosen as origin and is located at the center of the displaced fluid, hence CB* $= [x_{cb}, y_{cb}, z_{cb}]^T = [0, 0, 0]^T$

Assumption 4.2: *The position of the internal buoyancy mass (internal oil-tank/bladder)* $\boldsymbol{r}_{m_b} \in R^3$ *coincides with CB*

Assumption 4.3: *The transnational and angular acceleration of the internal point mass actuator are considered neglectable:* $\dot{v}_{m_p} = \dot{\omega}_{m_p} \approx 0$. *Thus the applied moving mass forces and moments are considered as constraint forces.*

Remark 4.1 *Assumption 4.3 is convenient as the internal moving mass actuators are in practice translated and rotated at low velocities. These effects are neglected in order to avoid modelling the complex coupled dynamics between the rigid glider body and internal moving masses*

A mathematical model of the glider is derived using the 6DOF vectorial marine craft dynamics presented in Fossen (2011). The state variables can be divided into two vectors - The position in the inertial frame $\{n\}$ defined as $\boldsymbol{\eta} = [x, y, z, \phi, \theta, \psi]^T$ and the relative velocity in the body frame $\{b\}$ $\boldsymbol{\nu}_r = [u_r, v_r, w_r, p, q, r]^T$. Ocean current disturbances are considered irrotational and constant in the inertial frame $\{n\}$. The ocean current model is assumed two-dimensional, where vertical currents w_c are neglected, from Fossen (2011) we have

$$\boldsymbol{\nu}_c^b = \begin{bmatrix} V_c^n \cdot cos(\beta_c - \psi) \\ V_c^n \cdot sin(\beta_c - \psi) \\ 0 \end{bmatrix}, \; V_c^n = \sqrt{u_c^n + v_c^n} \tag{9}$$

The 6DOF dynamics of an underwater glider is derived as

$$\boldsymbol{M}\dot{\boldsymbol{\nu_r}} + \boldsymbol{C}(\boldsymbol{\nu_r})\boldsymbol{\nu}_r + \boldsymbol{D}(\boldsymbol{\nu_r})\boldsymbol{\nu_r} + \boldsymbol{g}(\boldsymbol{\eta}) = \boldsymbol{\tau}_c \tag{10}$$

Where $\boldsymbol{M} \in \mathrm{R}^{6\times6} = \boldsymbol{M}_{rb} + \boldsymbol{M}_A$ and $\boldsymbol{C}(\boldsymbol{\nu}) \in \mathrm{R}^{6\times6} = \boldsymbol{C}_{rb}(\boldsymbol{\nu}) + \boldsymbol{C}_A(\boldsymbol{\nu})$ are the transnational and rotational rigid-body dynamics with correlating added mass effects. Hydrodynamic forces and moments are described in the damping matrix $\boldsymbol{D}(\boldsymbol{\nu}_3) \in \mathrm{R}^{6\times6}$ and the restoring forces are defined by $\boldsymbol{g}(\boldsymbol{\eta}) \in \mathrm{R}^{6\times1}$. $\boldsymbol{\tau}_c$ is the vector describing the control forces and moments which acts on the vehicle. Following assumption 4.3, we consider the applied control moments to be constraint forces, thus $\boldsymbol{\tau}_c = \boldsymbol{0}^{6\times1}$. The marine craft dynamics is defined by skew-symmetric properties which satisfies $\boldsymbol{S}(\boldsymbol{x})\cdot\boldsymbol{y} = \boldsymbol{x}\times\boldsymbol{y}$, where $\boldsymbol{S} \in \mathrm{R}^{3\times3}$ and $\boldsymbol{x} \in \mathrm{R}^{3\times1}$. Furthermore, we can derive the inertia matrix of the system as

$$\boldsymbol{M} = \begin{bmatrix} m\boldsymbol{I_{3\times3}} & -m\boldsymbol{S}(\boldsymbol{r}_{cg}) \\ m\boldsymbol{S}(\boldsymbol{r}_{cg}) & \boldsymbol{I}_{cg} - m\boldsymbol{S}^2(\boldsymbol{r}_{cg}) \end{bmatrix} - \begin{bmatrix} \boldsymbol{M}_{A_1} & \boldsymbol{0_{3\times3}} \\ \boldsymbol{0_{3\times3}} & \boldsymbol{M}_{A_2} \end{bmatrix} \tag{11}$$

where $\{\boldsymbol{M_{A_1}}, \boldsymbol{M_{A_2}}\} \in \mathrm{R}^{3\times3}$ are diagonal hydrodynamic derivatives (added mass) - $\boldsymbol{M_{A_1}} = diag([X_{\dot{u}}, Y_{\dot{v}}, Z_{\dot{w}}])$ and $\boldsymbol{M_{A_2}} = diag([K_{\dot{p}}, M_{\dot{q}}, N_{\dot{r}}])$. The center of gravity vector $\boldsymbol{r}_{cg}$ is not fixed in time due to the internal moving mass actuators, thus $\dot{\boldsymbol{r}}_{cg} \neq 0$. Following Graver (2005) we can derive the center of gravity vector as

$$\boldsymbol{r}_{cg} = \sum \frac{m_i \boldsymbol{r}_{mi}}{m_t} = \frac{m_s \boldsymbol{r}_{m_s} + m_p \boldsymbol{r}_{m_p} + m_b \boldsymbol{r}_b}{m_p + m_s + m_b + m_h} \in R^3 \tag{12}$$

For simplicity we assume that the position of the buoyancy mass $\boldsymbol{r}_b$ is fixed. Given a servo angle (angular position) of the rotating actuator γ, the position of the moving mass $\boldsymbol{r}_{m_p}$ with respect to the origin (CB) is given by Mahmoudian and Woolsey (2008) as

$$\boldsymbol{r}_{m_p} = \begin{bmatrix} r_{x_p} \\ r_{y_p} \\ r_{z_p} \end{bmatrix} = \begin{bmatrix} r_{x_p} \\ r_c \cdot cos(\gamma + \pi/2) \\ r_c \cdot sin(\gamma + \pi/2) \end{bmatrix} \tag{13}$$

where r_c is the radius of the semi-cylindrical mass (battery-pack). To model ocean currents in the 6DOF manoeuvring model, the rotational dynamics detailing Coriolis and centripetal forces is derived using *velocity-independent parametrizations* Fossen (2011). Given the body-fixed angular velocities $\boldsymbol{\omega_b} = [p, q, r]^T$ the rotational rigid-body dynamics is derived as

$$\begin{aligned} \boldsymbol{C}(\boldsymbol{\nu}) = &\begin{bmatrix} m \cdot \boldsymbol{S}(\boldsymbol{\omega_b}) & -m \cdot \boldsymbol{S}(\boldsymbol{\omega_b}) \cdot \boldsymbol{S}(\boldsymbol{r}_{cg}) \\ m \cdot \boldsymbol{S}(\boldsymbol{r_{cg}}) \cdot \boldsymbol{S}(\boldsymbol{\omega_b}) & -\boldsymbol{S}(\boldsymbol{I}_b \cdot \boldsymbol{\omega_b}) \end{bmatrix} \\ &- \begin{bmatrix} \boldsymbol{0_{3\times3}} & -\boldsymbol{S}(\boldsymbol{\nu} \cdot \boldsymbol{M}_{A_1}) \\ -\boldsymbol{S}(\boldsymbol{\nu} \cdot \boldsymbol{M}_{A_1}) & -\boldsymbol{S}(\boldsymbol{\omega}_b \cdot \boldsymbol{M}_{A_2}) \end{bmatrix} \end{aligned} \tag{14}$$

where $\boldsymbol{I}_b$ and m is the vehicle inertia and total mass respectively.

The restoring forces is the result of gravitational and buoyant forces acting on the vehicle. The buoyancy is defined by $B = \rho g \Delta$, which depends of the water density ρ and displaced fluid volume Δ. The gravity force and bouyant force can be defined in the inertial frame as $\boldsymbol{f}_g^n = [0, 0, -mg]$ and $\boldsymbol{f}_b^n = [0, 0, \rho g \Delta]$ respectively. Accordingly, the hydro static matrix is defined by

$$\boldsymbol{g}(\boldsymbol{\eta}) = -\begin{bmatrix} \boldsymbol{R}_b^n(\boldsymbol{\Theta})^{-1}(\boldsymbol{f}_g^n + \boldsymbol{f}_b^n) \\ \boldsymbol{S}(\boldsymbol{r}_{cg}) \cdot \boldsymbol{R}_b^n(\boldsymbol{\Theta})^{-1}\boldsymbol{f}_g^n + \boldsymbol{S}(\boldsymbol{r}_{cb}) \cdot \boldsymbol{R}_b^n(\boldsymbol{\Theta})^{-1}\boldsymbol{f}_b^n \end{bmatrix} \tag{15}$$

where $\boldsymbol{R}_b^n(\boldsymbol{\Theta}) \in SO(3)$ is the rotation matrix from the inertial frame $\{n\}$ to the body frame $\{b\}$, defined by the euler angles $\boldsymbol{\Theta} = [\phi, \theta, \psi]^T$. Note: information about the displaced fluid volume Δ is not always available, hence we replace this by the displaced fluid mass Δ_m which is altered by the net buoyancy mass m_b.

Lastly we derive the damping matrix $\boldsymbol{D}(\boldsymbol{\nu}_r)$. As fixed wing gliders shares similarities with fixed wing aerial vehicles,

Manuscript 28 submitted to 14th IFAC Conference on Control Applications in Marine Systems, Robotics, and Vehicles. Received April 21, 2022.

the damping terms are derived using standard aerodynamic coefficient based models, where control surface deflections are neglected. Due to low operating speeds, the damping is considered quadratic and diagonal, accordingly we have the matrix shape

$$\boldsymbol{D}(\boldsymbol{\nu}_r) = -diag([D, SF, L, K, M, N]) \tag{16}$$

where D, SF, L are drag, sideforce and lift force respectively, and K, M, N are moments about each axis (roll, pitch, yaw). Given a relative speed $U_r = \sqrt{u_r^2 + v_r^2 + w_r^2}$, angle-of-attack (AOA) $\alpha = asin(w/u)$ and sideslip angle (SSA) $\beta = atan(v/U)$ we can derive the hydrodynamic forces and moments in component form following the theory presented in Graver (2005) and Zhang et al. (2013)

$$\begin{aligned} D &= (K_{D_0} + K_D \cdot \alpha^2) \cdot U_r^2 \\ L &= (K_{L_0} + K_\alpha \cdot \alpha) \cdot U_r^2 \\ SF &= K_\beta \cdot \beta \cdot U_r^2 \\ K &= (K_{MR} \cdot \beta + K_p \cdot p) \cdot U_r^2 \\ M &= (K_{M0} + K_M \cdot \alpha + K_q \cdot q) \cdot U_r^2 \\ N &= (K_{MY} \cdot \beta + K_r \cdot r) \cdot U_r^2 \end{aligned} \tag{17}$$

where K_{D0}, K_D etc. are damping coefficients, ususally mapped in towing-tank facilities or using computational fluid dynamics (CFD) analysis, see Javaid et al. (2017), Zhang et al. (2013), Singh et al. (2017).

4. CONTROL & DEAD-RECKONING NAVIGATION

This section presents the low-level controllers for the underwater glider and dead-reckoning approaches with a limited navigation suite.

4.1 Control Objective

First we introduce an overview of the control objectives, both for path-following and low-level control. To follow an arbitrary planar path $\mathcal{P} \in \mathrm{R}^2$, the glider must satisfy the following conditions:

$$\begin{aligned} &\lim_{t\to\infty} (y - y_{LOS}) = 0 \\ &\lim_{t\to\infty} (\psi - \psi_{ILOS}) = 0, \quad \psi \in (-\pi, \pi) \\ &\lim_{t\to\infty} (\theta - \theta_d) = 0, \quad \theta \in (-\pi/4, \pi/4) \end{aligned} \tag{18}$$

The two first conditions satisfies convergence of the path following problem, while the latter condition ensures that the vehicle will move forward.

4.2 Pitch & Heading Control

Glider dynamics behaves in a slow and linear fashion. PID controllers are typically employed for attitude and heading control of gliders as presented in Eriksen et al. (2001), Graver (2005), Mahmoudian and Woolsey (2008). In this paper two PD controllers are implemented for the heading autopilot and pitch controller. A simple bang-bang controller is applied for the variable buoyancy system. A block diagram of the control system is illustrated in figure 2.
During downward glides, the control error $e(t)$ does converge towards zero as the pitch reference is negative. Hence, we introduce gain scheduling for the proportional terms. The procedure is simple, when the glider dives, the p-term is negative, and positive while ascending. We derive the PD controllers as

$$\begin{aligned} r_\gamma(t) &= k_{p_\psi} \cdot e_\psi(t) + k_{d_\psi} \cdot \dot{e_\psi} \\ r_x(t) &= k_{p_\theta} \cdot e_\theta(t) + k_{d_\theta} \cdot \dot{e_\theta} \end{aligned} \tag{19}$$

The PD terms used in this paper are defined as:

$$k_{p_\psi} = \pm 0.8 \quad k_{d_\psi} = 0.01 \quad k_{p_\theta} = \pm 3 \quad k_{d_\theta} = 0.05$$

4.3 DR Navigation: A Machine Learning Approach

A notorious challenge for underwater gliders is to navigate while submerged. Due to absence of GNSS systems, they rely on *dead-reckoning (DR)* to predict the position of the vehicle. DR relies on time-integration of the velocities wrt to it's inertial frame (see equation 2) to compute the vehicle displacement. As gliders rarely have access to acoustic navigational instruments such as doppler velocity loggers (DVLs), computing the relative surge and sway velocities are typically approximated using IMUs and depth sensors Woithe et al. (2013), which frequently leads to estimation errors. In this paper we propose a machine learning approach to approximating the relative surge and sway velocities based on the work in Saksvik et al. (2021). As illustrated in figure 2, an LSTM (Long-term-short-term memory) recurrent neural network is proposed to compute the velocities, using inputs from control actions (moving mass actuators, oil displacement), IMU data and depth sensor measurements. To train the neural network we need *ground truth* velocity measurements from a few sea-trials/simulations. After the network is trained, it approximates the relative velocities using only a limited sensor suite. To avoid large dead-reckoning errors, the glider frequently surfaces to get a GPS fix to reinitialize the algorithm.

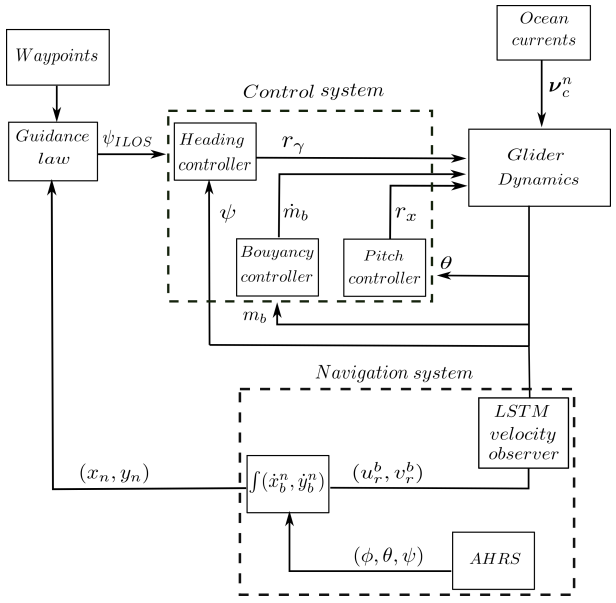

Figure 2. Guidance, Navigation & Control (GNC) systems - Block diagram

5. SIMULATIONS & RESULTS

A simulation enviroment based on the glider dynamics derived in section 3 was implemented in MATLAB/Simulink. The simulated glider object is the *Seawing* glider Zhang et al. (2013), which is 1.99 m long and have a net weight of 64.28 kg. Firstly, we investigate the performance of the path-following controllers in presence of a constant irrotational ocean current.

The first two experiment considers a straight-line trajectory and zig-zag trajectory while following the path between the predefined waypoints. The ILOS guidance law was implemeted in the simulation with a look-a-head distance of $\Lambda = 15$ m and $k_i = 0.05$. The ocean current mangitude and direction is given as $V_c^n = 0.25$ m/s and $\beta_c = 4.7$ rad (270°). The maximum operating depth of the glider is 60 meters in the simulation.
The first simulation (figure 3) have an initial position of $(x_0, y_0) = (0, 100)$ m.

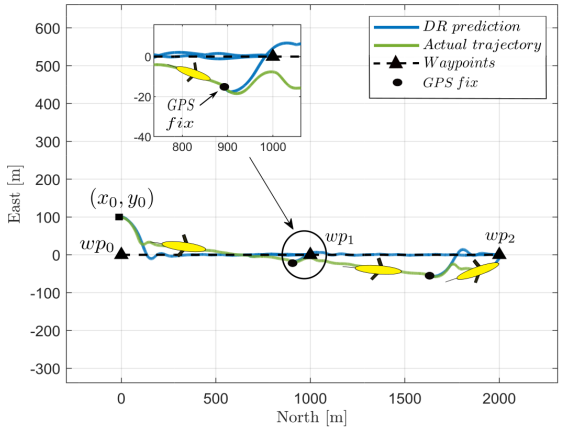

Figure 3. Path-following - Straight line trajectory

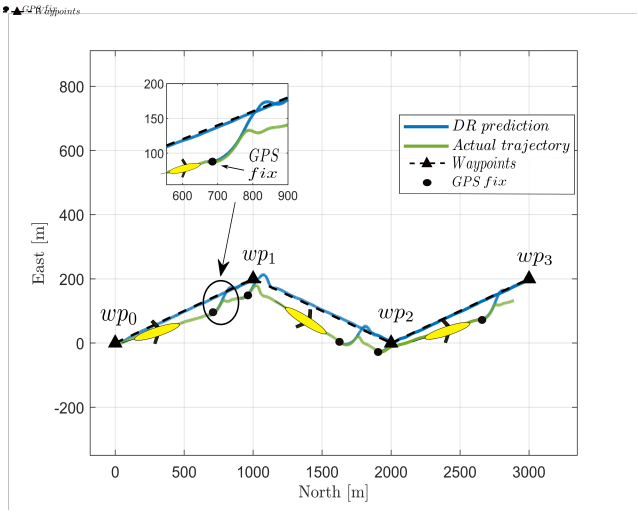

Figure 4. Path-following - Zigzag trajectory

The second experiment reconsiders the straight-line trajectory scenario illustrated in figure 3, but with varying ocean current magnitude and direction. This was done to investigate the performance of the path-following controller and the reliability of the dead-reckoning navigation system. The evaluation parameter in the following table is the mean cross-track error $\bar{y}_e$ derived as

$$\bar{y}_e = \frac{\sum_{i=1}^{N} y_e}{N} \tag{20}$$

The mean cross-track error was evaluated for different combinations of ocean current magnitude $V_c^n \in \{0.1, 0.2, 0.4\}$ m/s and ocean current direction $\beta_c \in \{0°, 30°, 90°, 150°, 210°, 270°, 330°\}$

$V_c^n = 0.1m/s$ (β_c, $\bar{y}_e$)	$V_c^n = 0.2m/s$ (β_c, $\bar{y}_e$)	$V_c^n = 0.4m/s$ (β_c, $\bar{y}_e$)
	ILOS	
(0°, 21.0 m)	(0°, 21.2 m)	(0°, 21.1 m)
(30°, 21.6 m)	(30°, 22.4 m)	(30°, 24.0 m)
(90°, 32.5 m)	(90°, 34.6 m)	(90°, 32.5 m)
(150°, 25.0 m)	(150°, 25.9 m)	(150°, 26.6 m)
(210°, 22.2 m)	(210°, 21.8 m)	(210°, 23.0 m)
(270°, 22.1 m)	(270°, 20.1 m)	(270°, 23.8 m)
(330°, 21.9 m)	(330°, 21.4 m)	(330°, 20.7 m)
	LOS	
(0°, 21.5 m)	(0°, 21.3 m)	(0°, 21.4 m)
(30°, 22.8 m)	(30°, 22.1 m)	(30°, 23.9 m)
(90°, 25.7 m)	(90°, 30.9 m)	(90°, 31.1 m)
(150°, 24.9 m)	(150°, 25.8 m)	(150°, 26.32 m)
(210°, 22.9 m)	(210°, 21.5 m)	(210°, 22.6 m)
(270°, 21.6 m)	(270°, 21.4 m)	(270°, 20.7 m)
(330°, 22.6 m)	(330°, 22.0 m)	(330°, 21.0 m)

Table 1. Path-following with different ocean current conditions

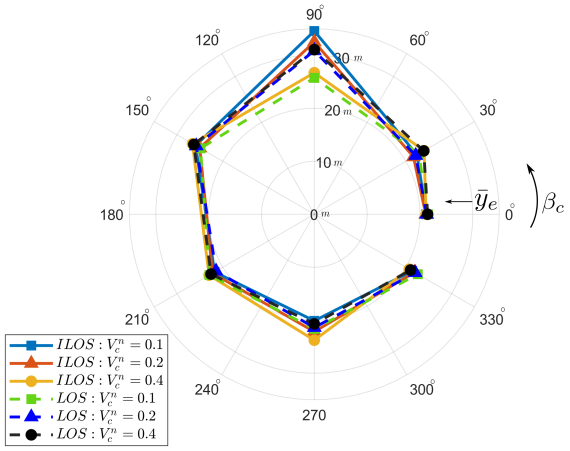

Figure 5. Mean cross-track error $\bar{y}_e$ vs ocean current magnitude and direction, V_c^n, β_c. Polar plot of table 1

6. CONCLUDING REMARKS

This work has addressed the path-following problem for underactuated underwater gliders with limited sensor payloads. Two planar motion line-of-sight guidance laws were implemented and compared. To improve dead-reckoning navigation, an LSTM recurrent neural network velocity observer was used. The simulation results, with significant dead-reckoning errors, shows that the mean error for straight line path-following problems for 2km displacements is between 20-40 meters.

REFERENCES

Borhaug, E., Pavlov, A., and Pettersen, K.Y. (2008). Integral los control for path following of underactuated marine surface vessels in the presence of constant ocean currents. In *2008 47th IEEE Conference on Decision and Control*, 4984–4991. IEEE.

Breivik, M. and Fossen, T.I. (2009). Guidance laws for autonomous underwater vehicles. *Underwater vehicles*, 4, 51–76.

Caharija, W., Pettersen, K.Y., Bibuli, M., Calado, P., Zereik, E., Braga, J., Gravdahl, J.T., Sørensen, A.J., Milovanović, M., and Bruzzone, G. (2016). Integral line-of-sight guidance and control of underactuated marine vehicles: Theory, simulations, and experiments. *IEEE Transactions on Control Systems Technology*, 24(5), 1623–1642.

Dong, J., Domingues, R., Goni, G., Halliwell, G., Kim, H.S., Lee, S.K., Mehari, M., Bringas, F., Morell, J., and Pomales, L. (2017). Impact of assimilating underwater glider data on hurricane gonzalo (2014) forecasts. *Weather and Forecasting*, 32(3), 1143–1159.

Eriksen, C.C., Osse, T.J., Light, R.D., Wen, T., Lehman, T.W., Sabin, P.L., Ballard, J.W., and Chiodi, A.M. (2001). Seaglider: A long-range autonomous underwater vehicle for oceanographic research. *IEEE Journal of oceanic Engineering*, 26(4), 424–436.

Fossen, T.I. (2011). *Handbook of marine craft hydrodynamics and motion control*. John Wiley & Sons.

Glenn, S., Schofield, O., Kohut, J., McDonnell, J., Ludescher, R., Seidel, D., Aragon, D., Haskins, T., Handel, E., Haldeman, C., et al. (2011). The trans-atlantic slocum glider expeditions: A catalyst for undergraduate participation in ocean science and technology. *Marine Technology Society Journal*, 45(1), 52–67.

Graver, J.G. (2005). Underwater gliders: Dynamics, control and design.

Javaid, M.Y., Ovinis, M., Hashim, F.B., Maimun, A., Ahmed, Y.M., and Ullah, B. (2017). Effect of wing form on the hydrodynamic characteristics and dynamic stability of an underwater glider. *International Journal of Naval Architecture and Ocean Engineering*, 9(4), 382–389.

Lekkas, A.M. and Fossen, T.I. (2013). Line-of-sight guidance for path following of marine vehicles. *Advanced in marine robotics*, 63–92.

Mahmoudian, N. and Woolsey, C. (2008). Underwater glider motion control. In *2008 47th IEEE Conference on Decision and Control*, 552–557. IEEE.

Martinsen, A.B. and Lekkas, A.M. (2018). Straight-path following for underactuated marine vessels using deep reinforcement learning. *IFAC-PapersOnLine*, 51(29), 329–334.

Saksvik, I.B., Alcocer, A., and Hassani, V. (2021). A deep learning approach to dead-reckoning navigation for autonomous underwater vehicles with limited sensor payloads. *arXiv preprint arXiv:2110.00661*.

Singh, Y., Bhattacharyya, S., and Idichandy, V. (2017). Cfd approach to modelling, hydrodynamic analysis and motion characteristics of a laboratory underwater glider with experimental results. *Journal of Ocean Engineering and Science*, 2(2), 90–119.

Wiig, M.S., Caharija, W., Krogstad, T.R., and Pettersen, K.Y. (2016). Integral line-of-sight guidance of underwater vehicles without neutral buoyancy. *IFAC-PapersOnLine*, 49(23), 590–597.

Woithe, H.C., Eichhorn, M., Schofield, O., and Kremer, U. (2013). Assessing automated and human path planning for the slocum glider. In *18th International Symposium on Unmanned Untethered Submersible Technology (UUST 2013)*.

Zhang, S., Yu, J., Zhang, A., and Zhang, F. (2013). Spiraling motion of underwater gliders: Modeling, analysis, and experimental results. *Ocean Engineering*, 60, 1–13.

Zhou, M., Bachmayer, R., and deYoung, B. (2016). Towards autonomous underwater iceberg profiling using a mechanical scanning sonar on a underwater slocum glider. In *2016 Ieee/Oes Autonomous Underwater Vehicles (Auv)*, 101–107. IEEE.

Manuscript 28 submitted to 14th IFAC Conference on Control Applications in Marine Systems, Robotics, and Vehicles. Received April 21, 2022.

Appendix C

Paper 2

Target Tracking Of an Underwater Glider using an Unmanned Surface Vessel (USV)

Ivar Bjørgo Saksvik, Alex Alcocer, Vahid Hassani, Antonio Pascoal

Accepted and to be published at the 14th IFAC Conference on Control Applications in Marine Systems, Robotics, and Vehicles (CAMS2022), Kgs. Lyngby, Denmark

Target Tracking of an Underwater Glider Using a Small Unmanned Surface Vessel

Ivar Bjørgo Saksvik * **Alex Alcocer** * **Vahid Hassani** *
Antonio Pascoal **

* *Department of Mechanical, Electronics and Chemical Engineering, Oslo Metropolitan University, Oslo, Norway (e-mail: s309664@oslomet.no, alepen@oslomet.no, vahid.hassani@oslomet.no).*
** *Laboratory of Robotics and Systems in Engineering and Science (LARSyS), ISR/IST, University of Lisbon, Lisbon, Portugal antonio@tecnico.ulisboa.pt*

Abstract: This paper propose a methodology for target tracking of an underwater glider using an *unmanned surface vessel* (USV). The topside USV is assumed to have knowledge about the position of the underwater glider from an acoustic positioning system, which is exploited to track the planar motions of the submerged vehicle from the surface. We propose a target tracking method for the purpose of glider localization using unmanned systems to reduce the operational costs and potential hazards. A guidance law is implemented in the topside vehicle to pursuit and intercept the underwater glider while it's performing generic saw-tooth and spiral maneuvers. A numerical simulation environment of the two vehicles is presented to validate the target-tracking scheme.

Keywords: Target tracking, Underwater Glider, Unmanned Surface Vehicle (USV).

1. INTRODUCTION

Navigation systems onboard underwater gliders are often prone to estimation errors due to limited sensor payloads. In practice, inertial measurement units (IMUs) and depth sensors are used to approximate the position of the glider trough simple kinematic equations, which frequently leads to navigation errors. Absence of accurate position estimates makes it challenging to evaluate guidance, navigation and control (GNC) systems. To obtain accurate estimates of glider trajectories, an acoustic baseline positioning system is typically employed as demonstrated in Graver et al. (2003) and Bahr et al. (2009). In practice, however, this requires cumbersome and costly deployment and calibration of a number of transponders in the seabed. This paper proposes a strategy for obtaining such trajectories using an unmanned boat equipped with a low-power acoustic positioning system with limited calibration requirements.

Due to range limitations in low-power acoustics, it's convenient to bound the planar distance between the topside vessel and submerged vehicle. From a control perspective, we refer to this as *target-tracking*, that is, to pursuit a moving target whose future motions are not known. The objective in this paper is to let the topside vessel track the horizontal displacement of the submerged glider. This motion control problem have been introduced in several underwater target-tracking & localization schemes using one or more autonomous surface vessels (ASVs), see e.g., Hung et al. (2021), Hung et al. (2020), Norgren et al. (2015). The maneuvering task related to tracking and localization is highly depended upon the number of range-measurements available to the topside vehicle(s). For instance, single-beacon vehicles, limited to one acoustic range measurement, impose a challenge to represent the target on a sphere (3D case) or circle (2D case) surrounding the recipient. In Moreno-Salinas et al. (2016) and Masmitja et al. (2018) the latter issue is solved by continuously encircling around about the target to increase the range-information from the target. In this paper we assume that the topside vessel is equipped with a short baseline (SBL) acoustic positioning system and that the position of the target is known throughout the simulation experiments. Moreover, a vectorial guidance law is proposed for the USV to track generic motions of an underwater glider. The guidance system is derived based on the *helsman principle* as the vessel cannot actuate the sway dynamics without changing it's course. Hence, the guidance law is decomposed to surge velocity and heading controllers to relax the dynamic and kinematic assignments of the target-tracking scheme respectively.

The remaining parts of this paper are organized as follows: The target-tracking guidance law and maneuvering model of the topside vessel is derived in section 2 and 3 respectively. The target, an underwater glider, is detailed in section 4. Simulation results are presented in section 5 and recommendations for further work are presented in the last section. Finally, an appendix with the complete equations of the USV is given.

⋆ This work was supported by the OASYS project funded by the Research Council of Norway (RCN), the German Federal Ministry of Economic Affairs and Energy (BMWi) and the European Commission under the framework of the ERA-NET Cofund MarTERA.

Manuscript 30 submitted to 14th IFAC Conference on Control Applications in Marine Systems, Robotics, and Vehicles. Received April 21, 2022.

2. TARGET TRACKING GUIDANCE LAW

The topics in airborne guidance systems have been extended to underactuated marine vessels in various research, see e.g. Breivik and Fossen (2007), Breivik et al. (2008), Norgren et al. (2015), and Skejic et al. (2009). In this section we derive a constant bearing (CB) guidance law based on the theory presented in the latter works. Following the notation in Breivik et al. (2008), we now refer to the surface vessel as the *interceptor* and the underwater glider as the *target*. Before deriving the guidance law we introduce some assumptions:

Assumption 2.1: *The following vectorial definitions are defined with respect to a fixed local frame denoted* $\{n\}$ *with an origin located at an arbitrary point.*

Assumption 2.2: *The tracked target is assumed to be a moving target such that the vessel speed satisfies* $U_t^n(t) > 0 \; \forall \; t$

Assumption 2.3: *The proposed guidance law consider a target moving in a planar plane, where vertical motions are neglected.*

Remark 2.1: *Assumption 2.1 imply the interceptor have no information about target's motion in the body-fixed frame* $\{b\}$*. Secondly, the origin of the fixed local frame* $\{n\}$ *is chosen by the control operator, typically somewhere close the operation Penas (2009)*

Guidance laws are typically derived at a kinematic level. Considering a horizontal plane, we define the planar distance between the target $\boldsymbol{P}_t^n \in \mathrm{R}^2$ and interceptor $\boldsymbol{P}_u^n \in \mathrm{R}^2$ as

$$\hat{\boldsymbol{P}}^n = (\boldsymbol{P}_t^n - \boldsymbol{P}_u^n) = \begin{bmatrix} x_t^n - y_t^n \\ x_u^n - y_u^n \end{bmatrix} \tag{1}$$

Differentiate $\boldsymbol{P}_t^n$ and $\boldsymbol{P}_u^n$ with respect to time yields the inertial velocities $\boldsymbol{\nu}_t^n = [\dot{x}_t^n, \dot{y}_u^n]^T$ and $\boldsymbol{\nu}_u^n = [\dot{x}_u^n, \dot{y}_u^n]^T$. Following Breivik et al. (2008), the CB guidance law is presented as a velocity assignment

$$\boldsymbol{\nu_d^n} = (\boldsymbol{\nu_t^n} + \boldsymbol{\nu_a^n}) \in \mathrm{R}^2 \tag{2}$$

where $\boldsymbol{\nu_a} \in \mathrm{R}^2$ is the desired approach velocity vector. Given a maximum approach speed $\bar{U}_a$ and a transient control parameter Λ, the approach velocity is given by

$$\boldsymbol{\nu_a^n} = \bar{U}_a^n \cdot \frac{\hat{\boldsymbol{P}}_n}{\sqrt{\hat{\boldsymbol{P}}_n^T \cdot \hat{\boldsymbol{P}}_n + \Lambda^2}} \in \mathrm{R}^2 \tag{3}$$

The maximum approach speed $\bar{U}_a^n$ must be chosen carefully according to maneuverability considerations and physical limitations of the USV.
Most vessels have underactuated sway dynamics during nominal operations (< 1 m/s). Accordingly, we cannot directly apply the desired velocity vector $\boldsymbol{\nu}_u^n$ onto the vessel. However, we can decompose the CB guidance law into surge and heading references, where the surge controller controls the velocity size and a heading controller is able to control the direction of the velocity vector. From the velocity assignment in eq. 2, we have the following velocity control objective:

$$\lim_{t\to\infty} (U_d^n - U_u^n) = 0 \tag{4}$$

where $U_d^n = \sqrt{\dot{x}_u^2 + \dot{y}_u^2}$ is the speed of the vessel. It is convenient to assume that $\dot{x}_u^n >> \dot{y}_u^n$ and that we let U_d^n yield

$$u_d^b \approx U_d^n \tag{5}$$

This introduces a new control objective, given as

$$\lim_{t\to\infty} (u_d^b - u_u^b) = 0 \tag{6}$$

where u_u^b is the surge velocity of the vessel in the body-fixed frame $\{b\}$.

A *line-of-sight* (LOS) steering law is used to compute heading references for the vessel. Following Skejic et al. (2009) and Breivik and Fossen (2009), the LOS steering law is derived based on the relative position and orientation of the vessel with respect to the target position $\boldsymbol{P}_t \in \mathrm{R}^2$. The cross-track distance x_e and cross-track error y_e is given by

$$\begin{aligned} x_e^n &= \; (x_u^n - x_t^n) \cdot cos(\chi_t) + (y_u^n - y_t^n) \cdot sin(\chi_t) \\ y_e^n &= -(x_u - x_t) \cdot sin(\chi_t) + (y_u - y_t) \cdot cos(\chi_t) \end{aligned} \tag{7}$$

where $\chi_t = atan2(\dot{y}_t^n, \dot{x}_t^n) \in [-\pi, \pi]$ is the target course angle. The LOS guidance law is derived with a *look-a-head* distance parameter Λ which determines the convergence rate towards the desired path. Λ is given in meters and must be tuned carefully such that it does not exceeds the maneuverability properties of the vessel. A common practice is to let $\lambda \in \{2, 5\} \cdot L_{usv}$. Where L_{usv} is the length of the vessel. Following Breivik and Fossen (2009) and Skejic et al. (2009) we have

$$\chi_{LOS} = tan^{-1}(\frac{-y_e^n}{\lambda}) \tag{8}$$

We can derive the desired heading reference by

$$\psi_d = (\chi_{LOS} + \chi_t) - \beta_u \tag{9}$$

where $\beta_u = atan(-\dot{y}, \dot{x})$ is the sideslip angle of the USV

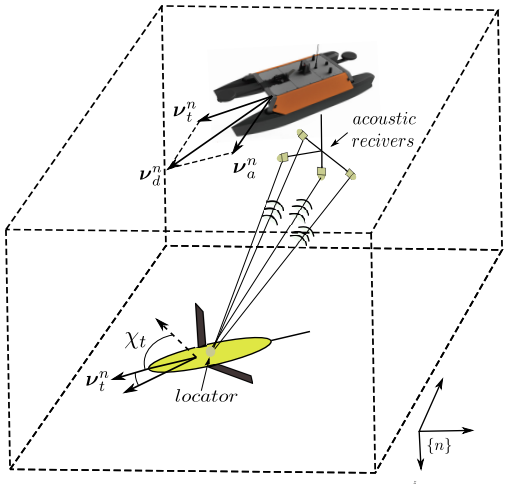

Figure 1. Target tracking of glider using an USV

3. USV MODEL

This section details the dynamics of the unmanned surface vessel. The vehicle simulated in this paper is the *Otter USV* developed by Maritime Robotics. The vehicle is characterized as a small unmanned catamaran as illustrated

Manuscript 30 submitted to 14th IFAC Conference on Control Applications in Marine Systems, Robotics, and Vehicles. Received April 21, 2022.

in figure 1. Before deriving the equations of motion, we introduce some basic assumptions about the system:

Assumption 3.1: *The vessel is actuated by differential thrust from two fixed stern propellers*

Assumption 3.2: *Environmental wind and wave loads acting on the vessel* $\boldsymbol{\tau}_{wind}, \boldsymbol{\tau}_{wave}$ *are neglected*

Assumption 3.3: *The payload (acoustic receiver antenna) hydrodynamic drag and added mass effects are neglected*

Assumption 3.4: *The vessel is influenced by an ocean current* $\boldsymbol{V}_c^n = [V_x, V_y, 0]^T$ *which is considered constant and irrotational in the inertial frame, hence* $\dot{\boldsymbol{V}}_c^n = 0$.

Assumption 3.5: *The hydrodynamic damping of the vessel is considered linear*

Figure 2. Maritime Robotics Otter USV with Waterlinked short-baseline (SBL) acoustic antenna/receivers, courtesy of OsloMet

The marine craft kinematics and dynamics are derived using the following state vectors: $\boldsymbol{\eta} = [x, y, \psi]^T$ consists of the inertial position and the heading (yaw) ψ of the vessel. The dynamics is defined by $\boldsymbol{\nu} = [u, v, r]^T$. Due to constant irrotational ocean currents, we rewrite the latter vector into a relative velocity vector following Fossen (2011): $\boldsymbol{\nu}_r = [u_r, v_r, r]^T = [u - u_c^b, v - v_c^b, r]^T$. The kinematics are defined by a rotation matrix $\boldsymbol{R_b^n(\psi)}$ from the body-frame $\{b\}$ to the inertial NED frame $\{n\}$. Accordingly, we have

$$\boldsymbol{R}_b^n(\psi) \triangleq \begin{bmatrix} c(\psi) & -s(\psi) & 0 \\ s(\psi) & c(\psi) & 0 \\ 0 & 0 & 1 \end{bmatrix}, \in SO(3) \tag{10}$$

where $c = cos()$ and $s = sin()$. The marine craft dynamics and kinematics of an unmanned surface vessel is given by

$$\dot{\boldsymbol{\eta}} = \boldsymbol{R}(\psi)\boldsymbol{\nu}_r + \boldsymbol{V}_c^n \tag{11}$$

$$\boldsymbol{M}\dot{\boldsymbol{\nu}_r} + \boldsymbol{C}(\boldsymbol{\nu_r})\boldsymbol{\nu}_r + \boldsymbol{D}(\boldsymbol{\nu_r})\boldsymbol{\nu_r} = \boldsymbol{\tau}_c \tag{12}$$

where $\boldsymbol{M} = \boldsymbol{M}_{rb} + \boldsymbol{M}_A$ and $\boldsymbol{C}(\boldsymbol{\nu}) = \boldsymbol{C}_{rb}(\boldsymbol{\nu}) + \boldsymbol{C}_A(\boldsymbol{\nu})$ are the translational and rotational rigid-body dynamics with correlating added mass effects. Hydrodynamic forces and moments are included in the damping matrix $\boldsymbol{D}(\boldsymbol{\nu})$. Control forces and moments which acts on the vessel are defined by $\boldsymbol{\tau}_c = \boldsymbol{B}\boldsymbol{\mathcal{K}}\boldsymbol{f} = [\tau_u, 0, \tau_r]^T$, where $\boldsymbol{B} \in \mathrm{R}^{3\times2}$ is the actuator configuration matrix which maps the control inputs (thruster revolutions) $\boldsymbol{f} = [T_u, 0, T_r]^T$ into surge forces and yaw moments. $\boldsymbol{\mathcal{K}} \in \mathrm{R}^{3\times3}$ is the diagonal force coefficient matrix. We have the following modelling considerations for the matrices $\boldsymbol{M}, \boldsymbol{C}, \boldsymbol{B}, \boldsymbol{D}$:

$$\begin{aligned} \boldsymbol{M} &\triangleq \begin{bmatrix} m_{11} & 0 & 0 \\ 0 & m_{22} & m_{23} \\ 0 & m_{32} & m_{33} \end{bmatrix}, \ \boldsymbol{B} \triangleq \begin{bmatrix} b_{11} & b_{12} \\ 0 & 0 \\ b_{31} & b_{32} \end{bmatrix} \\ \boldsymbol{C} &\triangleq \begin{bmatrix} 0 & 0 & c_{13} \\ 0 & 0 & c_{23} \\ c_{31} & c_{32} & 0 \end{bmatrix}, \quad \boldsymbol{D} \triangleq \begin{bmatrix} d_{11} & 0 & 0 \\ 0 & d_{22} & d_{23} \\ 0 & d_{32} & d_{33} \end{bmatrix} \end{aligned} \tag{13}$$

Following assumption 3.1 we have two *nonrotable* aft thrusters which imply that the control allocation problem is trivial and unconstrained. If we reduce $\boldsymbol{B}, \boldsymbol{\mathcal{K}}, \boldsymbol{\tau}_c$ to $\in \mathrm{R}^{2\times2}$ we can compute the control inputs as

$$\boldsymbol{f} = \boldsymbol{\mathcal{K}}^{-1}\ \boldsymbol{B}^{-1}\ \boldsymbol{\tau}_c = [T_u, T_r]^T \tag{14}$$

Following Paliotta et al. (2018) we can derive the kinematic and dynamic equations derived in eq. 3 into component form. Consequently, we have the following equations of motion:

$$\begin{aligned} \dot{x} &= u_r \cdot c(\psi) - v_r \cdot s(\psi) + V_x \\ \dot{y} &= v_r \cdot s(\psi) - v_r \cdot c(\psi) + V_y \\ \dot{\psi} &= r \\ \dot{r} &= F_r(u_r, v_r, r) + \tau_r \\ \dot{u}_r &= F_{u_r}(v_r) + \tau_u \\ \dot{v}_r &= X(u_r) + Y(u_r) \cdot v_r \end{aligned} \tag{15}$$

where $F_r(u_r, v_r, r), F_{u_r}(u_r)$ are defined in the Appendix. From Paliotta et al. (2018) we have that $X(u_r) = -X_1 \cdot u_r + X_2$, $Y(u_r) = -Y_1 \cdot u_r - Y_2$. From assumption 3.5 we assume that $X(u_r)$ and $Y(u_r)$ are linear functions.

3.1 Control objective

The control objective for the USV is to track a moving vehicle whose future path is not known. The target tracking error is defined by $\boldsymbol{e}_d = [x_d, y_d, \psi_d, u_d]^T$, where $\boldsymbol{e}_d$ represents the desired planar position, heading and surge velocity. Furthermore, we want to relax the following conditions

$$\begin{aligned} &\lim_{t\to\infty}(x - x_t) = 0, \quad \lim_{t\to\infty}(y - y_t) = 0 \\ &\lim_{t\to\infty}(\psi - \psi_d) = 0, \quad \lim_{t\to\infty}(u - u_d) = 0 \end{aligned} \tag{16}$$

Remark 3.1 *The control objectives imply that the control problem is underactuated as we aim to control 4DOF with only two control inputs* $\boldsymbol{u} \in \mathrm{R}^2$. *Considering assumption 2.2 we have that the vessel is always tracking a moving target with a speed* $U_t^n(t) = \sqrt{\dot{x}_t^2(t) + \dot{y}_t^2(t)} > 0 \ \forall\, t$, *thus dynamic positioning scenarios are neglected.*

3.2 Control System

As described in section 2, the CB guidance law is decomposed into surge and heading controllers. We assume that the surge-sway dynamics are decoupled, such that two model-based feedforward PI and PID controllers for surge and the heading can be implemented. Following Fossen (2011) we can linearize the maneuvering model in eq. 3

to 1DOF heading and surge subsystems (*Nomoto models*). Given the control errors $\hat{u} = (u - u_d)$ and $\hat{\psi} = (\psi - \psi_d)$, the surge PI controller and heading PID autopilot are given as

$$\begin{aligned}\tau_u =& (m - X_{\dot{u}})\,\dot{u} + X_u\,u_d - k_{p_u}\,\hat{u} - k_{i_u}\int_0^t \hat{u}(\tau)\,d\tau \\ \tau_r =& (I_z - N_{\dot{r}})\,\ddot{\psi}_d + N_r\,\dot{\psi} - k_{p_\psi}\,\hat{\psi} - k_{d_\psi}\,\dot{\hat{\psi}} - K_{i_\psi}\int_0^t \hat{\psi}(\tau)\,d\tau\end{aligned} \tag{17}$$

where $X_{\dot{u}}, X_u, N_{\dot{r}}, N_r$ are the hydrodynamic damping forces/moments and their derivatives (added mass) in surge and yaw and m and I_z are the vehicle mass and inertia (vertical component) respectively.

4. TARGET - UNDERWATER GLIDER

The target, an autonomous underwater glider (illustrated in figure 1), is a special class of autonomous underwater vehicles (AUVs). The glider's main source of locomotion is a variable buoyancy system (VBS), which allows the vehicle to move up and down in the water column. Variable buoyancy is often achieved by pumping oil between an external bladder exposed to the surrounding water and an internal reservoir. A minor volume change occurs when the oil is pumped between the two receptacles, resulting in a vertical movement (sink/rise). A set of fixed-wings attached to the glider body transform the vertical motion into forward movement from the horizontal component of the hydrodynamic lift force (vertical force). The absence of aft thrusters ensures longevity in glider missions as documented in various field experiments Glenn et al. (2011), Webb et al. (2001). Due to slow cruising speeds, conventional control surfaces are often replaced by an internal moving mass system. This typically consists of a custom shaped battery-pack that can be translated and rotated inside the glider housing, see Zhang et al. (2013), Mahmoudian and Woolsey (2008). The moving mass actuators are used in attitude and heading control, where they create control moments which amend the center of gravity vector. A detailed mathematical glider model (6DOF) is found in Saksvik et al. (2021). The steady-state flight characteristics of underwater gliders are twofold. If the vehicle is stable in roll (wings-levelled), it performs repeating saw-tooth maneuvers with non-zero pitch angles and a steady heading. Seen from the surface (2D), the trajectory is viewed as a straight-line. The latter can be parametarized by a scalar $\zeta \in R$ to yield

$$\mathcal{P} = \begin{bmatrix} x_p(\zeta) \\ y_p(\zeta) \end{bmatrix} = \begin{bmatrix} x_k + \zeta \cdot cos(\xi_p) \\ y_k + \zeta \cdot sin(\xi_p) \end{bmatrix} \tag{18}$$

where (x_k, y_k) is a fixed location on the path and ξ_p is the angle between the path and the x-axis along the stationary reference frame Breivik and Fossen (2009). The second flight is a vertical spiral. This happens if the rotating mass actuator is shifted. Accordingly, a roll moment is applied such that the wings are no longer aligned in the vertical plane. Assuming the vehicle is in steady-state, the spiral maneuver results in a circle seen from the surface.

$$\mathcal{P} = \begin{bmatrix} x_p(\zeta) \\ y_p(\zeta) \end{bmatrix} = \begin{bmatrix} x_c + r_c \cdot cos(\zeta / r_c) \\ y_c + \cdot\lambda \cdot r_c \cdot sin(\zeta / r_c) \end{bmatrix}, \quad \lambda \in \{-1, 1\} \tag{19}$$

where r_c is the radius of the circle, (x_c, y_c) is the center of the circle and λ represents the motion of direction - $\lambda = 1$ is clockwise.

5. SIMULATION & RESULTS

To validate the proposed target tracking scheme, a dual simulation environment of the target (underwater glider) and interceptor (USV) was developed. The dynamic model of the Otter USV was implemented using the MSS (Marine System Simulator) toolbox Perez et al. (2006) developed based on the topics in Fossen (2011). The simulated glider object is the *Seawing glider* presented in Zhang et al. (2013). This is a research glider with a length of 1.99 m and net weight of 64.2 kg. It's actuator configuration is similar to commercial legacy gliders with an oil based variable buoyancy system. The attitude and heading is controlled using internal moving and rotating mass actuators. This consists of a cylindrical battery-pack which can be translated and rotated inside the vehicle housing.

The dynamics of the USV and underwater glider were implemented in Simulink for simultaneous simulation, together with the constant bearing guidance law and control system presented in section 2 and 3 respectively. Two PD-controllers were implemented for pitch and heading control of the underwater glider, and a simple bang-bang controller adjusted the buoyancy of the vehicle.

5.1 Simulation parameters

Due to the slow cruising speeds in underwater gliders, we set the max approach speed in the CB guidance law as $\bar{U}_a^n = 0.5\ m/s$. Accordingly, we let $\Lambda = 10$. For the planar motion LOS guidance law we have let the look ahead distance be $\lambda = 5$ meters.

We present two general simulation cases for the target tracking application. These consists of a vertical spiral where the USV follows a circle from the surface, and a saw-tooth trajectory which results in a straight-line target tracking problem for the topside vehicle. During these simulations, there exists an ocean current with magnitude $V_c^n = \sqrt{u_c^n + v_c^n} = 0.15\ m/s$ and direction $\beta_c = \frac{\pi}{2}\ rad$. In the first simulation case the initial position and heading of the USV is given as $[x_0, y_0, \psi_0] = [0, -30, 0]^T$. The initial state for the underwater glider is $[x_0, y_0, \psi_0]^T = [0, 0, 0]^T$. Seen from the surface, the USV is initially located 30 meters off east with respect to the underwater glider, which is located at the origin of the inertial frame. The initial heading of the two vehicles coincides.

In the second case study we investigate the straight-line path following problem. In this scenario, the USV is initialized with an offset planar position and heading with respect to the glider. The following initial conditions are considered for the USV $[x_0, y_0, \psi_0] = [-100, -35, -\frac{\pi}{2}]^T$. Moreover, the initial conditions of the glider is the same as case 1: $[x_0, y_0, \psi_0]^T = [0, 0, 0]^T$.

5.2 Case 1 - Curved target tracking

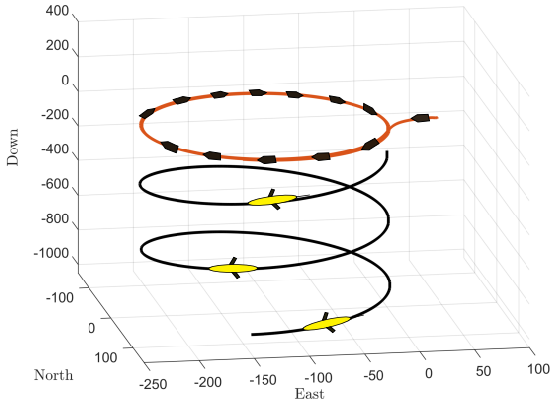

Figure 3. Circular target tracking

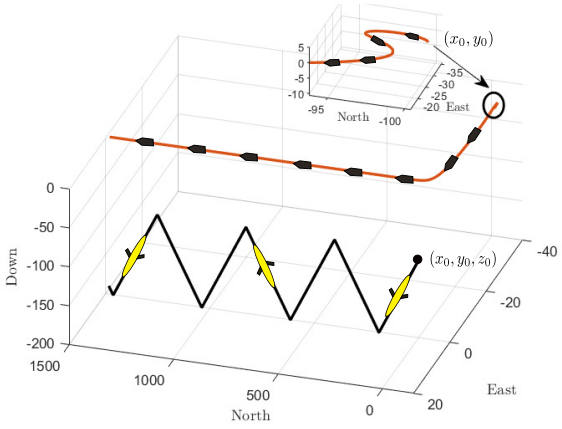

Figure 6. Straight-line target tracking

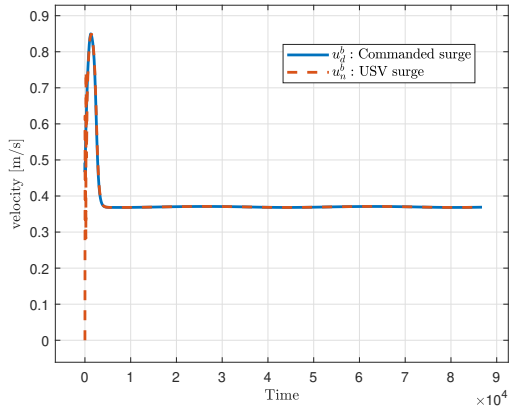

Figure 4. Surge control - Case 1

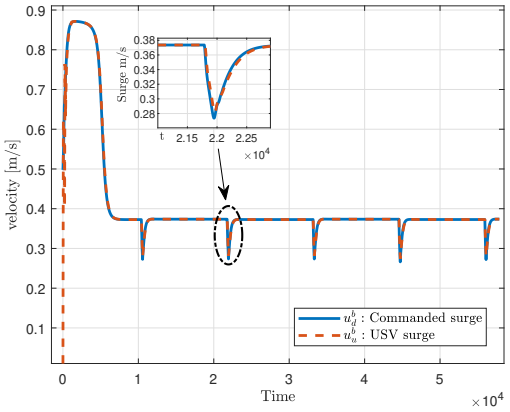

Figure 7. Surge control - Case 2

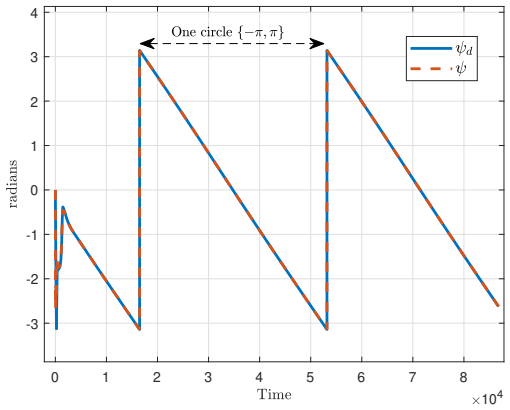

Figure 5. Heading autopilot - Case 1

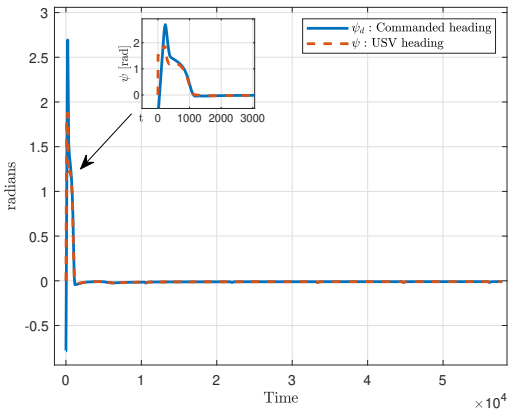

Figure 8. Heading autopilot - Case 2

6. FURTHER WORK

The extension of this work is to validate the proposed target tracking scheme with experimental tests. The aim is to use an Otter USV owned by the ocean laboratory (Oceanlab) at Oslo Metropolitan University in Oslo, Norway. The vessel is complemented by a short baseline (SBL) acoustic positioning system from Waterlinked. An acoustic receiver antenna is mounted on the vessel and submerged approximately 1-2 meters. A small omnidirectional acoustic locator (32 x 121 mm) is mounted on the underwater vehicle to transmit range measurements to the topside vessel.

7. APPENDIX

The terms $F_{u_r}(u_r), X(u_r), Y(u_r), F_r(u_r, v_r, r)$ are defined in this appendix. From Paliotta et al. (2018) we have the following definitions

$$\begin{aligned} F_{u_r}(v_r, r) &\triangleq \frac{1}{m_{11}} \left(m_{22}\, v_r + m_{23}\, r\right) r - \frac{d_{11}}{m_{11}}\, u_r \\ X(u_r) &\triangleq - \frac{m_{11}\, m_{33} - m_{23}^2}{m_{22}\, m_{33} - m_{23}^2}\, u_r + \frac{d_{33}\, m_{23} - d_{23}\, m_{33}}{m_{22}\, m_{33} - m_{23}^2} \\ Y(u_r) &\triangleq - \frac{(m_{11} - m_{22})\, m_{23}}{m_{22}\, m_{33} - m_{23}^2}\, u_r - \frac{d_{22}\, m_{33} - d_{32}\, m_{23}}{m_{22}\, m_{33} - m_{23}^2} \\ F_r(u_r, v_r, r) &\triangleq \frac{m_{23}\, d_{22} - m_{22}(d_{32} + (m_{22} - m_{11})\, u_r)}{m_{22}\, m_{33} - m_{23}^2} \cdot v_r \\ &\quad + \frac{m_{23}(d_{23} + m_{11}\, u_r) - m_{22}(d_{33} + m_{23}\, u_r)}{m_{22}\, m_{33} - m_{23}^2}\, r \end{aligned} \tag{20}$$

Remark 6.1 *The terms $Y(u_r)$ and $X(u_r)$ are assumed to be linear. Furthermore, $Y(u_r)$ have the following bounds:*

$$\frac{(m_{11} - m_{22})\, m_{23}}{m_{22}\, m_{33} - m_{23}^2}\, u_r > 0, \qquad \frac{d_{22}\, m_{33} - d_{32}\, m_{23}}{m_{22}\, m_{33} - m_{23}^2} > 0 \tag{21}$$

REFERENCES

Bahr, A., Leonard, J.J., and Fallon, M.F. (2009). Cooperative localization for autonomous underwater vehicles. *The International Journal of Robotics Research*, 28(6), 714–728.

Breivik, M. and Fossen, T.I. (2007). Applying missile guidance concepts to motion control of marine craft. *IFAC Proceedings Volumes*, 40(17), 349–354.

Breivik, M. and Fossen, T.I. (2009). Guidance laws for autonomous underwater vehicles. *Underwater vehicles*, 4, 51–76.

Breivik, M., Hovstein, V.E., and Fossen, T.I. (2008). Straight-line target tracking for unmanned surface vehicles.

Fossen, T.I. (2011). *Handbook of marine craft hydrodynamics and motion control*. John Wiley & Sons.

Glenn, S., Schofield, O., Kohut, J., McDonnell, J., Ludescher, R., Seidel, D., Aragon, D., Haskins, T., Handel, E., Haldeman, C., et al. (2011). The trans-atlantic slocum glider expeditions: A catalyst for undergraduate participation in ocean science and technology. *Marine Technology Society Journal*, 45(1), 52–67.

Graver, J.G., Bachmayer, R., Leonard, N.E., and Fratantoni, D.M. (2003). Underwater glider model parameter identification. In *Proc. 13th Int. Symp. on Unmanned Untethered Submersible Technology (UUST)*, volume 1, 12–13.

Hung, N.T., Crasta, N., Moreno-Salinas, D., Pascoal, A.M., and Johansen, T.A. (2020). Range-based target localization and pursuit with autonomous vehicles: An approach using posterior crlb and model predictive control. *Robotics and Autonomous Systems*, 132, 103608.

Hung, N.T., Rego, F.F., and Pascoal, A.M. (2021). Cooperative distributed estimation and control of multiple autonomous vehicles for range-based underwater target localization and pursuit. *IEEE Transactions on Control Systems Technology*.

Mahmoudian, N. and Woolsey, C. (2008). Underwater glider motion control. In *2008 47th IEEE Conference on Decision and Control*, 552–557. IEEE.

Masmitja, I., Gomariz, S., Del-Rio, J., Kieft, B., O'Reilly, T., Bouvet, P.J., and Aguzzi, J. (2018). Optimal path shape for range-only underwater target localization using a wave glider. *The International Journal of Robotics Research*, 37(12), 1447–1462.

Moreno-Salinas, D., Crasta, N., Ribeiro, M., Bayat, B., Pascoal, A., and Aranda, J. (2016). Integrated motion planning, control, and estimation for range-based marine vehicle positioning and target localization. *IFAC-PapersOnLine*, 49(23), 34–40.

Norgren, P., Ludvigsen, M., Ingebretsen, T., and Hovstein, V.E. (2015). Tracking and remote monitoring of an autonomous underwater vehicle using an unmanned surface vehicle in the trondheim fjord. In *OCEANS 2015-MTS/IEEE Washington*, 1–6. IEEE.

Paliotta, C., Lefeber, E., Pettersen, K.Y., Pinto, J., Costa, M., et al. (2018). Trajectory tracking and path following for underactuated marine vehicles. *IEEE Transactions on Control Systems Technology*, 27(4), 1423–1437.

Penas, A.A. (2009). Positioning and navigation systems for robotic underwater vehicles. *Doctor thesis, Instituto Superior Tcnico*.

Perez, T., Smogeli, O., Fossen, T., and Sorensen, A. (2006). An overview of the marine systems simulator (mss): A simulink toolbox for marine control systems. *Modeling, identification and Control*, 27(4), 259–275.

Saksvik, I.B., Alcocer, A., and Hassani, V. (2021). A deep learning approach to dead-reckoning navigation for autonomous underwater vehicles with limited sensor payloads. *arXiv preprint arXiv:2110.00661*.

Skejic, R., Breivik, M., Fossen, T.I., and Faltinsen, O.M. (2009). Modeling and control of underway replenishment operations in calm water. *IFAC Proceedings Volumes*, 42(18), 78–85.

Webb, D.C., Simonetti, P.J., and Jones, C.P. (2001). Slocum: An underwater glider propelled by environmental energy. *IEEE Journal of oceanic engineering*, 26(4), 447–452.

Zhang, S., Yu, J., Zhang, A., and Zhang, F. (2013). Spiraling motion of underwater gliders: Modeling, analysis, and experimental results. *Ocean Engineering*, 60, 1–13.

Appendix D

Paper 3

A Deep Learning Approach To Dead-Reckoning Navigation For Autonomous Underwater Vehicles With Limited Sensor Payloads

Ivar Bjørgo Saksvik, Alex Alcocer, Vahid Hassani

Submitted and Presented at the global IEEE Oceans 2021 Conference, Porto, Portugal

A Deep Learning Approach To Dead-Reckoning Navigation For Autonomous Underwater Vehicles With Limited Sensor Payloads

Ivar Bjørgo Saksvik
Department of Mechanical, Electronic and Chemical Engineering
Oslo Metropolitan University
Oslo, Norway
s309664@oslomet.no

Alex Alcocer
Department of Mechanical, Electronic and Chemical Engineering
Oslo Metropolitan University
Oslo, Norway
alepen@oslomet.no

Vahid Hassani
Department of Mechanical, Electronic and Chemical Engineering
Oslo Metropolitan University
Oslo, Norway
vahidhas@oslomet.no

***Abstract*—This paper presents a deep learning approach to aid dead-reckoning (DR) navigation using a limited sensor suite. A Recurrent Neural Network (RNN) was developed to predict the relative horizontal velocities of an Autonomous Underwater Vehicle (AUV) using data from an IMU, pressure sensor, and control inputs. The RNN network is trained using experimental data, where a doppler velocity logger (DVL) provided ground truth velocities. The predictions of the relative velocities were implemented in a dead-reckoning algorithm to approximate north and east positions. The studies in this paper were twofold I) Experimental data from a Long-Range AUV was investigated. Datasets from a series of surveys in Monterey Bay, California (U.S) were used to train and test the RNN network. II) The second study explore datasets generated by a simulated autonomous underwater glider. Environmental variables e.g ocean currents were implemented in the simulation to reflect real ocean conditions. The proposed neural network approach to DR navigation was compared to the on-board navigation system and ground truth simulated positions.**

***Index Terms*—Underwater Navigation, Deep learning, Dead-reckoning, Autonomous Underwater Vehicles (AUV)**

I. Introduction

Autonomous underwater vehicles (AUVs) have in the last decades become important tools in ocean research. Untethered from umbilical cables, these vehicles are suitable for a high variety of applications including bathymetric mapping, water sampling and environmental monitoring. A notorious challenge for AUVs is to navigate and *georeference* acquired sensor data during operations as GPS signals can't propagate trough water. Conventional solutions to this issue involve adding acoustic navigational or/and positioning instruments to the AUV payload. Due to the good propagation of sound in water, doppler velocity loggers and acoustic baseline systems are considered the backbone in AUV navigation and underwater positioning [10], [25]. However, these traditional sensors are often expensive and consumes large amounts of power. In AUV fleets, the cost of adding acoustic instruments is compounded with the number of vehicles. In this paper we consider a limited sensor suite consisting of an IMU sensor and a pressure transducer, where acoustic instruments are partially available to collect experimental training data. Collected DVL velocity measurements from only a few missions are used as a reference in supervised neural network training. The aim for the trained network is to complement DR navigation when the DVL sensor is inaccessible, for example in AUV fleets with budget limitations.

The absence of acoustic navigational and positioning instruments has traditionally been compensated by model-based observers like Extended Kalman Filters (EKFs). These are derived from AUV dynamics to form an estimation model [8], [9], [21], [22]. Unfortunately, model-based observers rely on parameters that are difficult to obtain in practice. The dynamics of an AUV is derived based on intricate hydrodynamic models. Experiments must be carried out in a towing-tank facility or using expensive CFD (Computational Fluid Dynamics) software to obtain hydrodynamic damping coefficients [28], [3]. If the external geometry of the AUV changes, i.e. when making small modifications to payload sections, the coefficients need to be updated.

To avoid deriving complex AUV models and conducting time consuming towing-tank or CFD experiments, this paper presents a data-driven approach to dead-reckoning navigation. Using experimental data from AUV missions and simulations, a neural network is trained to learn and generalize relative AUV motions. Data-driven neural network regression abolishes the need for knowledge of a dynamic model, and avoids modelling and estimation errors related to classical state observers [4], [5]. A recurrent neural network (RNN) is developed to relax time-delayed effects in the AUV dynamics which occurs due to vehicle inertia, under actuation and added mass effects [1], [6]. With an input layer composed of standard sensory measurements (pressure sensor, inertial measurement unit) and control actions, the RNN network aims to predict relative surge u_r and sway v_r velocities. These are further implemented in a dead-reckoning algorithm

to approximate North and East positions during operations.

A. Related Work

Several articles have addressed artificial neural network state estimation for marine crafts. In Zhang *et al.* [4] a Short-Term Long-Term-Memory (LSTM) recurrent neural network is proposed to estimate the relative position of an AUV. The LSTM network used data from a pressure sensor, an inertial measurement unit (IMU), and an acoustic doppler velocity logger (DVL) to predict the horizontal north and east positions. Training and validation data were collected from a series of surface trajectories while logging GPS locations, which were projected as ground truth measurements. A similar study with the same AUV is presented in Mu *et al.* [5], where a bi-directional LSTM network was used. A neural network approach to dead-reckoning navigation of dynamically positioned ships is presented in Skulestad *et al.* [6]. Control actions and commands from vessel thrusters combined with heading measurements was used as input data in a RNN network to aid navigation during GNSS outages. Experiments were conducted in a vessel simulator with time-varying environmental disturbances such as wind forces, sea waves and ocean currents. In Chen *et al.* [13] a neural network is presented to assist navigation during DVL malfunction. A nonlinear autoregressive network with exogenous SINS (Strapdown Inertial Navigation System) inputs was used. The network was tested and validated on a ship with a DVL mounted on the vessel hull to provide training and validation data.

The remaining parts of this paper are detailing the following segments - Section II and III addresses the concept of dead-reckoning navigation and the neural network velocity observer respectively. Section IV presents the AUV platforms and datasets used to train and test the neural networks. The results are detailed in section V and the conclusion and recommendations for further work are presented in VI.

II. Dead-Reckoning Navigation

In the absence of GNSS (Global Navigation Satellite Systems) systems, AUVs enters a dead-reckoning mode while under water. The DR algorithm predicts the position of the AUV based on estimates at the previous time-step. With a reference of the heading and attitude combined with relative velocity measurements, the position is determined by numerical integration. To compute the relative position of the AUV, the measured/estimated relative velocities must be rotated with respect to the inertial reference frame of the vehicle. Following [1] the inertial frame of underwater vehicles is defined by North-East-Down (NED) local tangent plane coordinates. The NED velocities $\dot{\boldsymbol{\chi}} = [\dot{N}, \dot{E}, \dot{D}]^T$ of an AUV are derived by an rotation matrix from the body frame $\{b\}$ to the inertial frame $\{n\}$ [1]. An AUV influenced by ocean currents $\boldsymbol{v}_c$ will have a relative velocity $\boldsymbol{v}_r$. Assuming that the ocean currents are irrotational they are derived following [1] as $\boldsymbol{v}_r = [u_r, v_r, w_r]^T = [u - u_c, v - v_c, w - w_c]^T$. Accordingly, the relationship between the relative body-fixed and inertial velocities are given as

$$\dot{\boldsymbol{\chi}} = \boldsymbol{R}_b^n(\boldsymbol{\Theta}) \cdot \boldsymbol{v}_r \tag{1}$$

Where $\boldsymbol{\Theta} = [\phi, \theta, \psi]^T$ is the attitude and heading of the AUV provided by an inertial measurement unit (IMU). Equation 1 can be written in expanded form as

$$\begin{bmatrix} \dot{N} \\ \dot{E} \\ \dot{D} \end{bmatrix} = \begin{bmatrix} u_r \cdot c(\psi)c(\theta) + v_r \cdot [c(\psi)s(\theta)s(\phi) - s(\psi)c(\phi)] \\ +w_r \cdot [s(\psi)s(\phi) + c(\psi)c(\phi)s(\theta))] \\ u_r \cdot s(\psi)c(\theta) + v_r \cdot [c(\psi)c(\phi) + s(\phi)s(\theta)s(\psi)] \\ -u_r \cdot s(\theta) + v_r \cdot c(\theta)s(\phi) + w_r \cdot c(\theta)c(\phi) \end{bmatrix} \tag{2}$$

where $c() = cos()$ and $s() = sin()$.
For AUVs that typically operate with a zero angle of attack the attitude can be neglected in eq. 2. However, for other vehicles like underwater gliders which can perform spiraling motions with non-zero attitude $[\phi, \theta]^T \neq 0$, it persist. After rotating the relative velocities according to the inertial frame of the vehicle, numerical integration is performed to obtain the position. Given the previous predicted position $\boldsymbol{\chi}_t = [N_t, E_t, D_t]^T$ the DR algorithm is derived following [6]

$$\boldsymbol{\chi}(t+1) = \boldsymbol{\chi}(t) + \boldsymbol{R}_b^n(\boldsymbol{\Theta}) \cdot \boldsymbol{v_r}(t+1) \cdot \Delta t \tag{3}$$

Where Δt is the time step between the predictions.

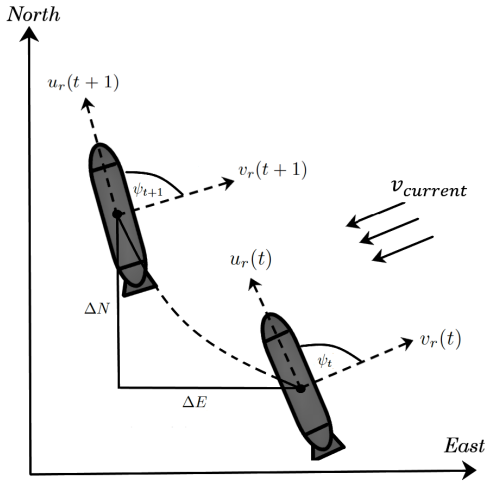

Fig. 1. DR navigation Illustration

III. Neural Network Aided Dead-Reckoning Navigation

A. Sensor Inputs

On-board sensors like IMUs and pressure transducers contains valuable in-situ information about an AUV. These are used as input variables in the RNN network to predict relative horizontal velocities $[u_r, v_r]^T$. The development of MEMS (Micro-Electrical-Mechanical-Systems) based IMUs have led

to more affordable inertial measurements. They consist of three-axis gyroscopes and accelerometers, typically confined in a silicon chip. The gyroscope, which give measurements of the angular rates $\boldsymbol{\omega^b_{IMU}} = [p_b, q_b, r_b]^T$ and the accelerometer which provide measurements of the rate-change of velocities $\dot{\boldsymbol{v}}^{\boldsymbol{b}}_{\boldsymbol{IMU}} = [\dot{u}_b, \dot{v}_b, \dot{w}_b]^T$ can be modelled as

$$\begin{aligned} \boldsymbol{\omega}^b_{IMU} &= \boldsymbol{\omega}^b_{gyro} + \boldsymbol{b}^b_{gyro} \\ \dot{\boldsymbol{v}}^b_{IMU} &= \dot{\boldsymbol{v}}^b_{acc} + \boldsymbol{b}^b_{acc} \end{aligned} \tag{4}$$

Where $\boldsymbol{b}^b_{gyro}$ and $\boldsymbol{b}^b_{acc}$ are sensor biases [33]. Combined with a three-axis compass, a Kalman Filter derived from a kinematic model impart the euler angles $\boldsymbol{\Theta} = [\phi, \theta, \psi]^T$. A key component in AUVs is the pressure transducer. The relationship between pressure and depth are assumed to be constant, thus the vertical position of the AUV can be approximated by the pressure measurements. Given a measured hydrostatic pressure Δp, water density ρ and gravitation g, the vertical position z and relative heave velocity w_r is derived as

$$z = \rho g \Delta p \implies w_r = \boldsymbol{R}^{-1}_{bn}(\boldsymbol{\Theta}) \cdot \dot{z} \tag{5}$$

Where z is assumed to be inertial $\{n\}$ and the relative heave velocity w_r is represented in the body-fixed frame $\{b\}$

B. AUV Control Actuators

To enforce the neural network state observer, control actions from the AUV actuators are used together with the sensor data. In this paper two AUVs with different actuator configurations are investigated. Conventional underactuated AUVs are normally equipped with an aft thurster and external control surfaces. The thruster is the propulsion system which generates a hydrodynamic force τ to induce surge transnational motions, while control surfaces consist of external airfoils that alter attitude and heading depending on their deflection angles. The control surfaces typically consist of a rudder and dive planes denoted δ_R and δ_D respectively. Control actions are determined from feedback controllers which in these studies are decoupled into vertical and horizontal manoeuvres. For thruster based AUVs, speed controllers are used to maintain a desired velocity and reject ocean current disturbances. In addition to the conventional AUV actuators, a variable buoyancy system and internal moving masses are introduced by the AUVs investigated in this paper. The simulated autonomous underwater glider uses buoyancy displacement to alter vertical motions, while a set of fixed wings generates hydrodynamic lift forces to induce forward motions. As gliders operates at low-speeds, control surfaces are ineffective due to low dynamic pressure. Control moments from internal moving masses are used to change the attitude and heading of the vehicle.

C. RNN Architecture

The RNN architecture is formed with feedback loops in the hidden layers of the network, providing internal *memory* to capture AUV dynamics with time-delays. To improve the estimation of the relative horizontal surge and sway velocities $[u_r, v_r]^T$, two independent neural networks are used for each velocity vector. This is convenient as surge and sway dynamics are often non-interacting or slightly interacting [1], [4]. Using input variables that holds low dependence to the predicted output variables reduces the generalization of the network and may lead to the notorious issue of *overfitting* [20], [15].

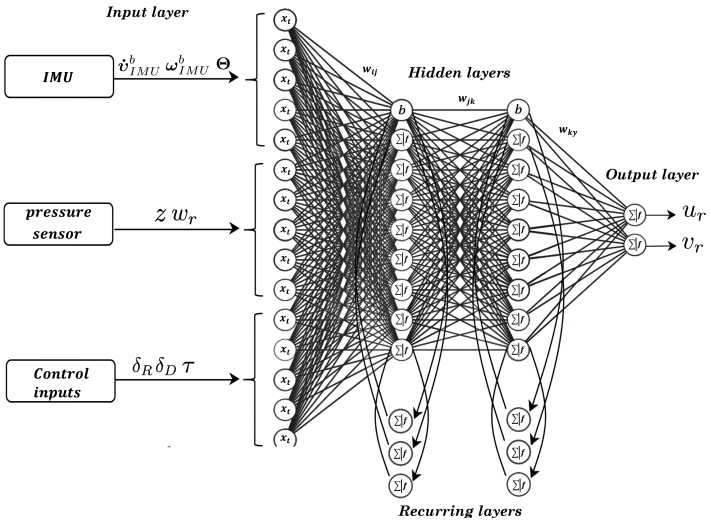

Fig. 2. Neural network illustration

RNN networks are generalized feedforward neural networks, but differs as recurring context layers are included in the hidden layers as illustrated in figure 2. The hidden nodes $\boldsymbol{h}(t)$ summarize the inputs $\boldsymbol{x}$ and weights w_{xh} from the previous layer combined with the recurring layer $\boldsymbol{h}(t-i)$. The hidden neurons $\boldsymbol{h(t)}$ and output neurons $\boldsymbol{y(t)}$ is derived mathematically as

$$\begin{aligned} \boldsymbol{h}(t) &= \sigma_h(\sum w_{xh} \cdot \boldsymbol{x} + \sum w_{hh} \cdot \boldsymbol{h}(t-i) + \boldsymbol{b}_n) \\ \boldsymbol{y}(t) &= lin(\sum w_{hy} \cdot \boldsymbol{h}(t) + \boldsymbol{b}_y) \end{aligned} \tag{6}$$

Trough sequential learning based on AUV datasets, the RNN network learns to predict the relative horizontal velocities. Activation functions σ_h in the hidden layers are the key to learning the nonlinearity between the selected inputs and predicted outputs. The network is trained based on the renowned concept of *backpropogation* introduced in [24] to tune the weights and biases. The goal of neural network training is to optimize the network parameters so that the error function E is minimized

$$E = \frac{1}{2} \sum_i (\hat{v}_r(i) - v_r(i))^2 \tag{7}$$

Where $\hat{v}_r(i) - v_r(i)$ is the difference between the actual and predicted relative velocities.

D. Navigational training data

In this work, experimental DVL data and simulated velocities are used as a reference for the supervised neural

network training. Alternative approaches may involve using acoustic positioning systems which are not prone to cumulative integration errors [10], thus providing more accurate ground truth measurements. However, a disadvantage with these approaches is that the DVL/acoustic modem must be replaced with "dummy" sensor to avoid changing the hydrodynamic properties and net weight of the AUV. Ideally, we want to have a reference of the AUV velocities/positions without changing the geometry and weight. A potential solution is to use visual based (machine vision) pose estimation relative to an assisting AUV/ROV. Machine vision has proven to be successful in autonomous docking operations for AUVs [29], [30] and may possibly be extended to tracking applications.

IV. AUV Platforms & Datasets

To train and validate the neural network approach to DR navigation, AUV datasets are needed. In this paper two AUV platforms are investigated. The first dataset originates from sea-trials of the Tethys Long-Range AUV (LRAUV), while the second dataset is from a MATLAB simulation of an underwater glider.

A. Tethys AUV

The Tethys Long-Range AUV [2], [14] was developed by the Monterey Bay Research Institute (MBARI) as a research AUV with long-range capabilities. It's characterized as a hybrid AUV as it shares similar control actuators to underwater gliders. This allows it to operate both in undulating glider-like trajectories and at fixed depths. Datasets from the constellation of underwater vehicles at MBARI is available through their public data repository [15].

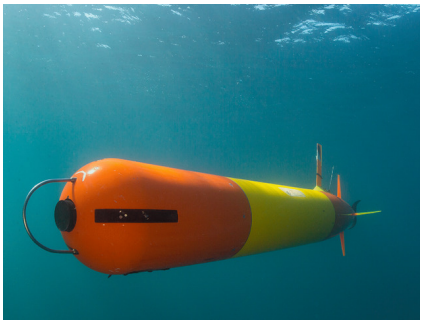

Fig. 3. Tethys AUV, courtesy of MBARI

A series of missions in Monterey bay, California (U.S) were used to train and validate the neural networks. In-situ measurements from a Microstrain 3DM-GX5-24 IMU, Neil Brown pressure sensor and the control actuators were used as inputs to the neural network. Ground truth relative surge and sway velocities $[u_r, v_r]^T$ were provided by a LinkQuest 600 KHz micro DVL. With periodic GPS fixes the overall navigation accuracy for DVL-aided inertial DR is 3-4 $\%$ [2]. The navigational errors arise initially from sensor noise and random walk errors from the inertial measurement sensor.
The parameters for the IMU and DVL sensors hosted on the Tethys is presented in table I and II respectively. The maximum operating altitude refer to *bottom lock* navigation, where the AUV measures it's velocities relative to the seafloor. When out of range the DVL can measure the velocities relative to the water (*water lock*). However, water is often considered as a moving reference frame due to ocean currents, which introduces estimation errors depending on the magnitude of the ocean current vector [10].

TABLE I
MICROSTRAIN 3DM-GX5-25 IMU PARAMETERS

Error	value
Accelerometer Bias Instability	$\pm$ 0.04 mg
Gyroscope Bias Instability	$\pm\ 8°/h$
Attitude Accuracy	EFK - $\pm$ 0.25° RMS
Heading Accuracy	EFK - $\pm$ 0.8° RMS

TABLE II
LINKQUEST 600 KHZ MICRO DVL PARAMETERS

Parameter	Value
Max Altitude	110 meters
Min Altitude	0.3 meters
Accuracy	1 $\%$ $\pm$ 1 mm/s
Ping rate	5 Hz

A minor part of the training dataset is presented in figure 4. Sensor noise has been filtered out with low-pass filters and Gaussian smoothing. We can observe that the AUV performs saw-tooth trajectories by using the dive plane control surface and internal moving mass actuator. The heading is mostly constant which indicates that the AUV is on a course keeping path governed by a heading controller.

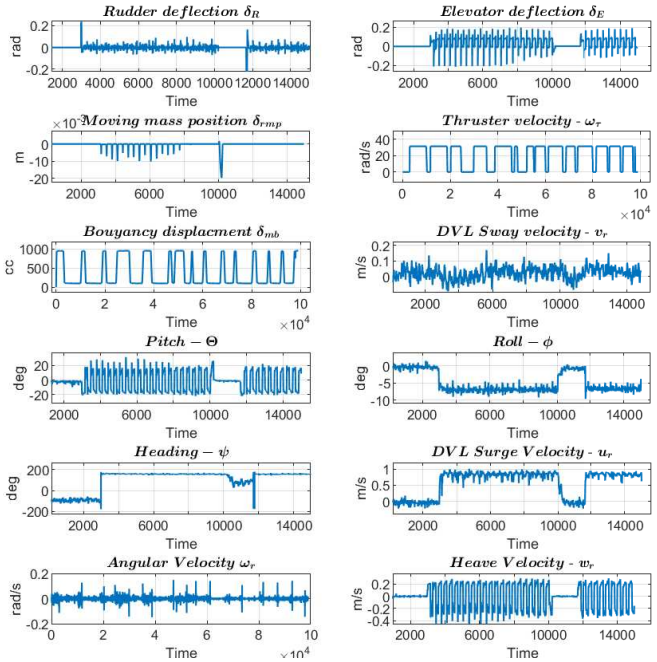

Fig. 4. Training data Tethys AUV

B. Underwater Glider

The second dataset is gathered from a MATLAB simulation of the Seawing underwater glider [3], [11]. An underwater glider is characterized as a slender body with fixed wings. A variable buoyancy system (VBS) is used to manipulate the volume that the vehicle is displacing to alter vertical motions in the water column. Underwater gliders exploit hydrodynamic properties using fixed wings to generate a forward motion. To control the attitude and heading of the vehicle, an internal moving mass system is used. This typically consists of a battery-pack that can be translated and rotated inside the vehicle housing. A mathematical model of the glider is derived using the 6DOF vectorial marine craft dynamics presented in Fossen [1]. State variables can be divided into two vectors following SNAME notation [17] - The position in the inertial frame $\{n\}$ defined as $\boldsymbol{\eta} = [x, y, z, \phi, \theta, \psi]^T$ and the relative velocity in the body frame $\{b\}$ $\boldsymbol{\nu_r} = [u_r, v_r, w_r, p, q, r]^T$. Accordingly, a 6DOF kinematic and maneuvering model of an AUV is derived by

$$\begin{aligned} \dot{\boldsymbol{\eta}} &= \boldsymbol{J_\theta}(\boldsymbol{\eta})\boldsymbol{\nu_r} \\ \boldsymbol{M}\dot{\boldsymbol{\nu_r}} + \boldsymbol{C}(\boldsymbol{\nu_r})\boldsymbol{\nu}_r + \boldsymbol{D}(\boldsymbol{\nu_r})\boldsymbol{\nu_r} + \boldsymbol{g}(\boldsymbol{\eta}) &= \boldsymbol{\tau} \end{aligned} \tag{8}$$

Where $\boldsymbol{M} = \boldsymbol{M}_{rb} + \boldsymbol{M}_A$ and $\boldsymbol{C}(\boldsymbol{\nu})$ = $\boldsymbol{C}_{rb}(\boldsymbol{\nu})$ + $\boldsymbol{C}_A(\boldsymbol{\nu})$ are the transnational and rotational rigid-body dynamics with correlating added mass effects. Hydrodynamic forces and moments are described in the damping matrix $\boldsymbol{D}(\boldsymbol{\nu})$ and the restoring forces are defined by $\boldsymbol{g}(\boldsymbol{\eta})$. $\boldsymbol{\tau}$ is the vector describing the control forces and moments which acts on the vehicle.

In presence of ocean currents, the ***relative velocity*** is defined by differentiating the body-fixed velocities to the ocean current vector $\boldsymbol{\nu_r} = \boldsymbol{\nu} - \boldsymbol{\nu}_c$. In the Matlab simulation we consider a two-dimensional irrotational ocean current model. Given an absolute velocity $V_c = \sqrt{u_c^2 + v_c^2}$ we can define the ocean currents in the body frame as

$$\boldsymbol{\nu}_c^b = \begin{bmatrix} V_c \cdot cos(\beta_c - \psi) \\ V_c \cdot sin(\beta_c - \psi) \\ 0 \end{bmatrix} \tag{9}$$

Many chose to simplify the ocean current model to be constant in the body-fixed frame $\{b\}$, thus $\dot{\boldsymbol{\upsilon}_c^b} = 0$ [18]. However, this only yields during course keeping. A more realistic approach is to assume that the ocean currents are time-varying with respect to rotational motions of the glider. Consider a skew-symmetric matrix $\boldsymbol{S}$ that satisfies $\boldsymbol{S}(\boldsymbol{x}) \cdot \boldsymbol{y} = \boldsymbol{x} \times \boldsymbol{y}$ and the angular velocities in the body frame $\boldsymbol{\omega_b}$, the ocean currents can be derived as

$$\dot{\boldsymbol{\nu}}_c^b = -\boldsymbol{S}(\boldsymbol{\omega_b}) \cdot \boldsymbol{\upsilon}_c^b \tag{10}$$

In order to model ocean currents in the 6DOF manoeuvring model, the rotational dynamics detailing Coriolis and centripetal forces must be derived using *velocity-independent parametrizations* [1]. Given a center of gravity vector relative to the center of origin $\boldsymbol{r}_{cg} = [x_{cg}, y_{cg}, z_{cg}]^T$ the Coriolis and centripetal matrix can be defined as

$$\boldsymbol{C}_{rb}(\boldsymbol{\nu}) = \begin{bmatrix} m \cdot \boldsymbol{S}(\boldsymbol{\omega_b}) & -m \cdot \boldsymbol{S}(\boldsymbol{\omega_b}) \cdot \boldsymbol{S}(\boldsymbol{r_{cg}}) \\ m \cdot \boldsymbol{S}(\boldsymbol{r_{cg}}) \cdot \boldsymbol{S}(\boldsymbol{\omega_b}) & -\boldsymbol{S}(\boldsymbol{I}_b \cdot \boldsymbol{\omega_b}) \end{bmatrix} \tag{11}$$

Where $\boldsymbol{I}_b$ and m is the vehicle inertia and total mass respectively. As demonstrated in eq.11 the rotational dynamics is derived only using angular velocities $\boldsymbol{\omega_b} = [p, q, r]^T$, which satisfies the following property [1]

$$\boldsymbol{M}_{rb}\boldsymbol{\nu} + \boldsymbol{C}_{rb}(\boldsymbol{\nu})\boldsymbol{\nu} = \boldsymbol{M}_{rb}\boldsymbol{\nu}_r + \boldsymbol{C}_{rb}(\boldsymbol{\nu}_r)\boldsymbol{\nu}_r \tag{12}$$

Glider dynamics was simulated in Simulink for a 10-hour interval. Time-varying control inputs and ocean currents were present during the simulation to provide variance in the training dataset. The simulated trajectories of the glider were a combination of undulating wings-levelled motions and turning/spiral manoeuvres. To control the attitude and heading of the glider, two decoupled PID controllers was implemented. The measured state variables were logged and saved to workspace during the simulation. Each training variable holds 81 000 samples, while the validation dataset resulted in 20 000 samples per variable. The test dataset is a combination of wings-levelled manoeuvres and spiral trajectories which differed from the trajectories used in the training data. Hence, we can validate how well the network is generalized to untrained glider motions.

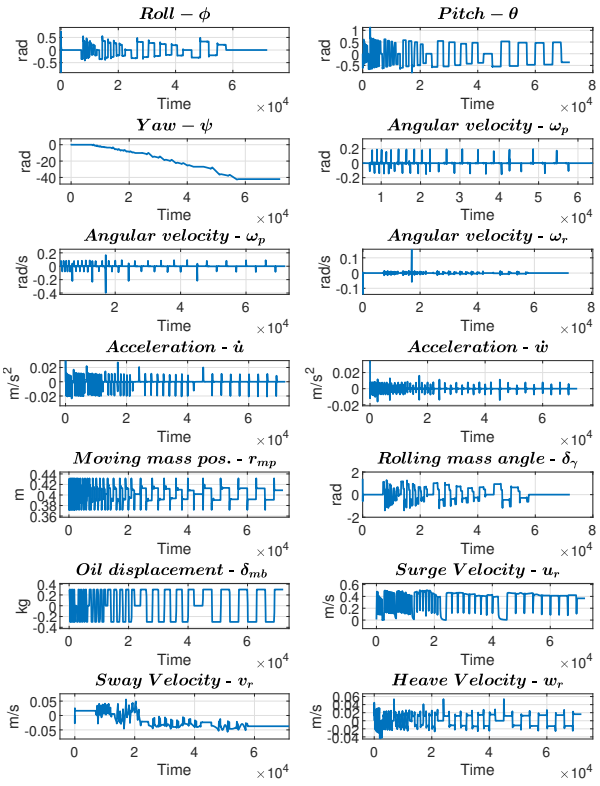

Fig. 5. Simulated glider training data

V. Experimental and Simulation Results

This paper presents a two-folded study which consists of simulated and experimental datasets. Collected AUV data was allocated into Matlab and further used to develop, train, and test the neural networks. The predicted outputs was fed into the dead-reckoning algorithm derived in eq. 3.
The Deep Learning Toolbox was used to design network architectures and perform backpropogation training. A Scaled Conjugate Gradient (SCG) algorithm was chosen as the training function to deal with the large AUV datasets effectively. The SCG algorithm [24] abolish the need for line-searches as presented in its predecessor [25] which reduces the computational load. To improve the generalization of the neural networks, *early-stopping* was introduced. Early-stopping divides the AUV dataset into training and validation batches. The training dataset is fed into the SCG algorithm to tune the weights and biases, while the validation data is used to monitor and detect if occurrences of overfitting is evident [32]. If the network starts to overfit the dataset, the training is aborted, hence the name early-stopping.

A. Case Study 1 - Tethys AUV

Experimental data from the Tethys AUV was investigated in the initial study. Data from three individual surveys was concatenated as a time-series vector and used as training data. Datasets from another mission is used to test the neural network on unseen data. The duration of the test trajectory is approximately 3 hours long. The mission, illustrated in figure 6, was conducted in shallow waters were the on-board Link Quest Micro DVL was able to get a *bottom-lock*, although some samples were out of reach for the operating altitude of the DVL sensor. Outliners in the DVL data was removed and further filtered with Gaussian smoothing.

Fig. 6. Test trajectory in Monterey Bay, California

The test trajectories consist of undulating saw-tooth motions with non-zero angle of attack α as showed in figure 8. Note that periodic GPS fixes was not accounted for in the results presented in figure 8 and 7. Two RNN networks was developed to isolate relative surge and sway predictions. The following table presents the training parameters used for the Tethys AUV.

TABLE III
ANN Training parameters - Tethys AUV

Backpropogation Optimizer	Scaled Conjugate Gradient (SCG)
MSE Surge Network	0.0347
MSE Sway Network	0.00588
Early Stopping Data Division	Randomly
Early Stopping index	Training 70 %, Val. 15%, Test 15%
Hidden layers	3
Hidden neurons per layer	40
Regressors per context layer	5

The results are presented in figure 7 and 8. The blue dotted line represents the predicted position based on estimated surge and sway velocities from the RNN network. The orange line is the estimated position based on measured DVL velocities.

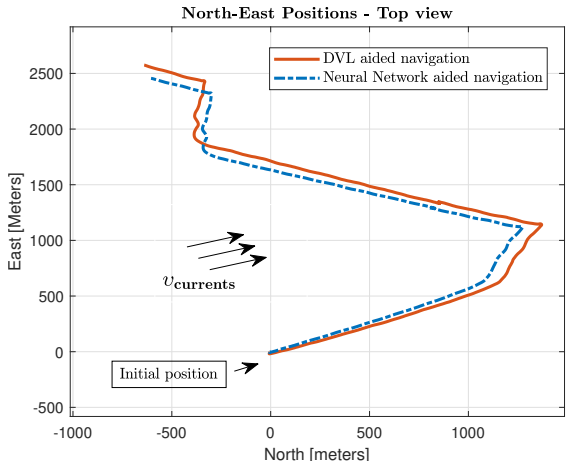

Fig. 7. Neural network aided navigation - Top view

A 3D view of the same trajectory is presented in figure 8 where depth measurements from the pressure sensor is used for the vertical z-axis.

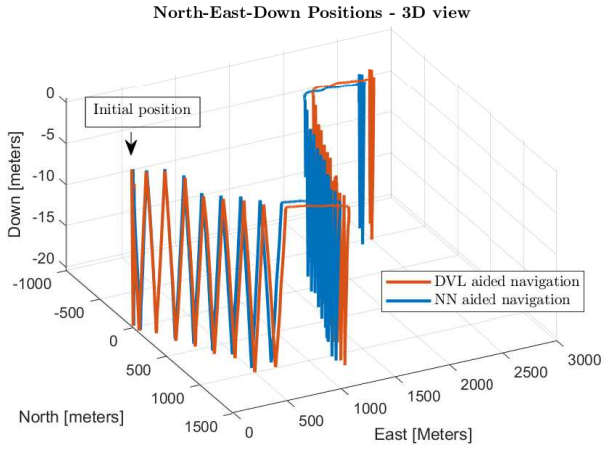

Fig. 8. Neural network aided navigation - 3D view

The positioning error between the predicted and DVL-aided horizontal positions was used to evaluate the performance. The positioning error is derived as

$$\begin{bmatrix} N_{error} \\ E_{error} \end{bmatrix} = \begin{bmatrix} || N_{est} - \hat{N} || \\ || E_{est} - \hat{E} || \end{bmatrix} \tag{13}$$

Where $\hat{N}$ and $\hat{E}$ are ground truth north and east positions respectively.

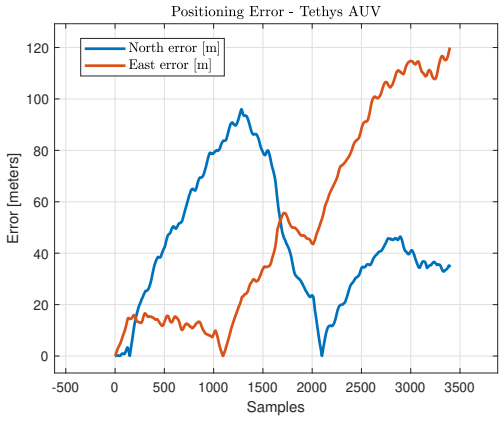

Fig. 9. Positioning Errors - Tethys AUV

The positioning error relates to an approximate displacement of 2500 meters north and 1500 meter displacement in the east direction. Note that the ground truth north and east positions estimated based on DVL velocities also have estimation errors with an 3-4 % navigational accuracy [2].

B. Case Study 2 - Underwater Glider

A second case study was conducted with the simulated autonomous underwater glider. Training and test datasets were generated by the Simulink simulation of the glider dynamics. A two-dimensional ocean current model was added in the dynamics to create a simulated environment that reflects real ocean conditions. Simulated ocean currents are assumed to be constant, but time-varying during glider rotations.

Due to decoupled attitude and heading controllers from the simulated trajectories, the interaction between the surge and sway dynamics is assumed to be neglectable. Thus, two isolated RNN networks was developed to predict the relative surge and sway velocities.

Table IV presents the neural network training parameters for the two RNN networks.

TABLE IV
ANN TRAINING PARAMETERS - GLIDER

Backpropogation Optimizer	Scaled Conjugate Gradient (SCG)
MSE Surge Network	0.000212
MSE Sway Network	0.00000459
Early Stopping Data Division	Randomly
Early Stopping index	Training 70 %, Val. 15%, Test 15%
Hidden layers	3
Hidden neurons per layer	50
Regressors per context layer	5

The test trajectory presented in figure 10 consists of two spiral motions and a wings-levelled movement. Three different ocean current scenarios was simulated with increasing magnitude, see figure 11. The plot illustrated in figure 10 shows the test dataset in presence of low currents - $u_c = -0.05\ m/s$ and $v_c = -0.002\ m/s$.

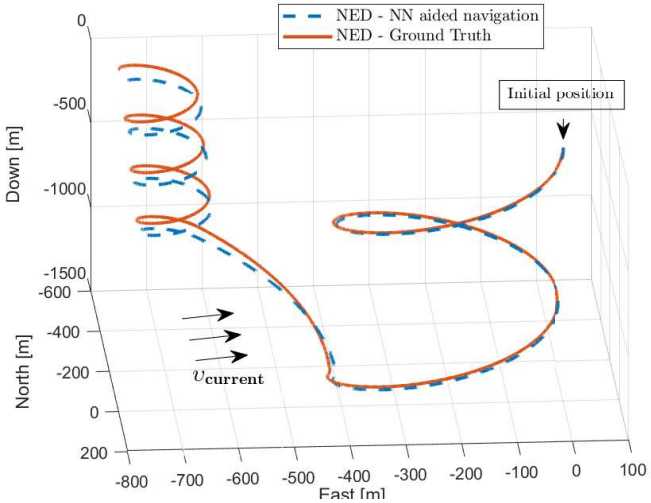

Fig. 10. Estimated NED position vs ground truth

RNN velocity predictions is presented by the blue dotted line in figure 10. The orange line represents ground truth simulated NED positions. The glider trajectory was simulated for 2.7 hours. The remaining simulations with increasing ocean currents are presented in figure 11 where the north and east positioning errors are compared by the three different scenarios. Note that the x-axis relates to total samples with a rate of 2 Hz. Accordingly, the real simulation time was 10 000 sec.

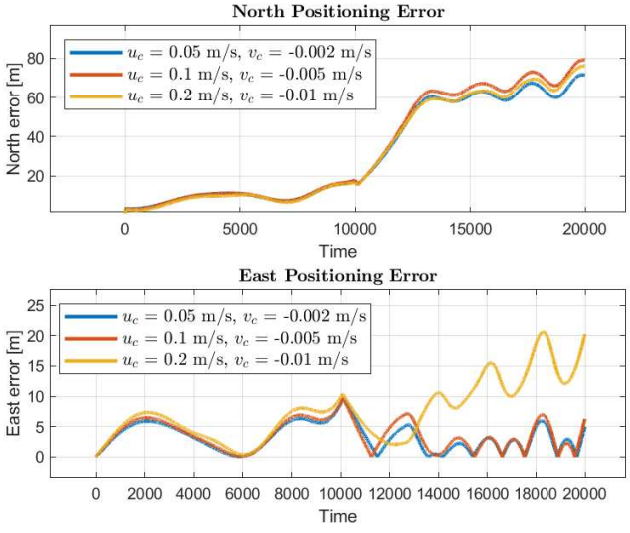

Fig. 11. Positioning error with increasing ocean currents

During the two first simulations with low and medium strong

currents the positioning error is slightly increased. The simulation with strongest ocean currents induced a larger divergence for the east positioning error, while a low increase in the north error.

VI. Conclusions And Further Work

A neural network approach to aid dead-reckoning navigation for AUVs with a limited sensor suite was proposed in this work. Experimental data from an IMU, a pressure sensor and control actions were gathered from sea-trials and simulations with correlating ground truth DVL and simulated velocities. The objective for the trained RNN networks is to complement AUV navigation in absence of acoustic navigational instruments. Results from the proposed method show promising potential considering a limited sensor payload. Improvements can be made by re-initializing the DR algorithm with GPS fixes when the AUVs are surfacing. The positioning error for the underwater glider grows slightly with increasing magnitude of ocean current disturbances as illustrated in figure 11. Glider positioning errors are significantly lower compared to DVL-less traditional navigation algorithms used in commercial gliders [31]. However, sensor noise and random walk errors were not present in the simulated IMU measurements. Further iterations of the simulated environment will focus on adding more realistic scenarios by introducing sensor errors, GPS fixes and vertical decomposition of the ocean currents.

Recommendations for further work include investigating alternative methods to obtaining experimental data. Vision based pose estimation is considered a promising candidate which avoids replacing the DVL or acoustic modem with a "dummy" sensor. Another interesting subject is to extend the deep learning approach to other underwater robots like remotely operated vehicles (ROVs). Compared to under-actuated AUVs, small/miniaturized ROVs are easy to deploy and does not require large displacements to excite the ROV dynamics, making the experimental procedures less time-consuming.

VII. Acknowledgments

We thank the Monterey Bay Research Institute (MBARI) for granting access to mission data from the Tethys AUV.
This work was supported by the OASYS project funded by the Research Council of Norway (RCN), the German Federal Ministry of Economic Affairs and Energy (BMWi) and the European Commission under the framework of the ERA-NET Cofund MarTERA.

References

[1] Fossen, T. I. (2011). Handbook of marine craft hydrodynamics and motion control. John Wiley & Sons.

[2] Hobson, B. W., Bellingham, J. G., Kieft, B., McEwen, R., Godin, M., & Zhang, Y. (2012, September). Tethys-class long range AUVs-extending the endurance of propeller-driven cruising AUVs from days to weeks. In 2012 IEEE/OES autonomous underwater vehicles (AUV) (pp. 1-8). IEEE.

[3] Zhang, S., Yu, J., Zhang, A., & Zhang, F. (2013). Spiraling motion of underwater gliders: Modeling, analysis, and experimental results. Ocean Engineering, 60, 1-13.

[4] Zhang, X., He, B., Li, G., Mu, X., Zhou, Y., & Mang, T. (2020). Navnet: AUV Navigation Through Deep Sequential Learning. IEEE Access, 8, 59845-59861.

[5] Mu, X., He, B., Zhang, X., Song, Y., Shen, Y., & Feng, C. (2019). End-to-end navigation for autonomous underwater vehicle with hybrid recurrent neural networks. Ocean Engineering, 194, 106602.

[6] Skulstad, R., Li, G., Fossen, T. I., Vik, B., & Zhang, H. (2019). Dead reckoning of dynamically positioned ships: Using an efficient recurrent neural network. IEEE Robotics & Automation Magazine, 26(3), 39-51.

[7] Buduma, N., & Locascio, N. (2017). Fundamentals of deep learning: Designing next-generation machine intelligence algorithms. " O'Reilly Media, Inc.".

[8] Wang, P., Singh, P. K., & Yi, J. (2013, May). Dynamic model-aided localization of underwater autonomous gliders. In 2013 IEEE International Conference on Robotics and Automation (pp. 5565-5570). IEEE.

[9] Snyder, W., Van Uffelen, L., & Renken, M. (2019, June). Effects of Incorporating Inertial Measurements on the Localization Accuracy of the Seaglider AUV. In OCEANS 2019-Marseille (pp. 1-6). IEEE.

[10] Penas, A. A. (2009). Positioning and navigation systems for robotic underwater vehicles. Doctor thesis, Instituto Superior Tcnico.

[11] Yu, J. C., Zhang, A. Q., Jin, W. M., Chen, Q., Tian, Y., & Liu, C. J. (2011). Development and experiments of the sea-wing underwater glider. China Ocean Engineering, 25(4), 721-736.

[12] Graver, J. G. (2005). Underwater gliders: Dynamics, control and design.

[13] Li, W., Chen, M., Zhang, C., Zhang, L., & Chen, R. (2020). A Novel Neural Network-Based SINS/DVL Integrated Navigation Approach to Deal with DVL Malfunction for Underwater Vehicles. Mathematical Problems in Engineering, 2020.

[14] Bellingham, J. G., Zhang, Y., Kerwin, J. E., Erikson, J., Hobson, B., Kieft, B., ... & Banka, A. (2010, September). Efficient propulsion for the Tethys long-range autonomous underwater vehicle. In 2010 IEEE/OES Autonomous Underwater Vehicles (pp. 1-7). IEEE.

[15] Alpaydin, E. (2020). Introduction to machine learning. MIT press.

[16] MBARI.com, 'MBARI Data Repository', 2014. [Online]. Available: https://www.mbari.org/products/data-repository/. [Accessed: 22- Jul- 2021].

[17] SNAME, T. (1950). Nomenclature for treating the motion of a submerged body through a fluid. The Society of Naval Architects and Marine Engineers, Technical and Research Bulletin, (1950), 1-5.

[18] Børhaug, E., Pivano, L., Pettersen, K. Y., & Johansen, T. A. (2007). A model-based ocean current observer for 6DOF underwater vehicles. IFAC Proceedings Volumes, 40(17), 169-174.

[19] Todd, R. E., Rudnick, D. L., Sherman, J. T., Owens, W. B., & George, L. (2017). Absolute velocity estimates from autonomous underwater gliders equipped with Doppler current profilers. Journal of Atmospheric and Oceanic Technology, 34(2), 309-333.

[20] May, R., Dandy, G., & Maier, H. (2011). Review of input variable selection methods for artificial neural networks. Artificial neural networks-methodological advances and biomedical applications, 10, 16004.

[21] Sabet, M. T., Daniali, H. M., Fathi, A., & Alizadeh, E. (2017). A low-cost dead reckoning navigation system for an AUV using a robust AHRS: Design and experimental analysis. IEEE Journal of Oceanic Engineering, 43(4), 927-939.

[22] Rypkema, N. R., Fischell, E. M., Forrest, A. L., Benjamin, M. R., & Schmidt, H. (2018, November). Implementation of a hydrodynamic model-based navigation system for a low-cost AUV fleet. In 2018 IEEE/OES Autonomous Underwater Vehicle Workshop (AUV) (pp. 1-6). IEEE.

[23] Møller, M. F. (1993). A scaled conjugate gradient algorithm for fast supervised learning. Neural networks, 6(4), 525-533.

[24] Johansson, E. M., Dowla, F. U., & Goodman, D. M. (1991). Backpropagation learning for multilayer feed-forward neural networks using the conjugate gradient method. International Journal of Neural Systems, 2(04), 291-301.

[25] Rumelhart, D. E., Hinton, G. E., & Williams, R. J. (1985). Learning internal representations by error propagation. California Univ San Diego La Jolla Inst for Cognitive Science.

[26] González-García, J., Gómez-Espinosa, A., Cuan-Urquizo, E., García-Valdovinos, L. G., Salgado-Jiménez, T., & Cabello, J. A. E. (2020). Autonomous underwater vehicles: localization, navigation, and communication for collaborative missions. Applied sciences, 10(4), 1256.

[27] Li, W., Zhang, L., Sun, F., Yang, L., Chen, M., & Li, Y. (2015). Alignment calibration of IMU and Doppler sensors for precision INS/DVL integrated navigation. Optik, 126(23), 3872-3876.
[28] Javanmard, E., Mansoorzadeh, S., Pishevar, A., & Mehr, J. A. (2020). Determination of drag and lift related coefficients of an auv using computational and experimental fluid dynamics methods. Transactions of the Royal Institution of Naval Architects Part A: International Journal of Maritime Engineering, 162(Part A2), A177-A191.
[29] Liu, S., Xu, H., Lin, Y., & Gao, L. (2019). Visual navigation for recovering an AUV by another AUV in shallow water. Sensors, 19(8), 1889.
[30] Li, Y., Jiang, Y., Cao, J., Wang, B., & Li, Y. (2015). AUV docking experiments based on vision positioning using two cameras. Ocean Engineering, 110, 163-173.
[31] Woithe, H. C., Boehm, D., & Kremer, U. (2011, September). Improving slocum glider dead reckoning using a doppler velocity log. In OCEANS'11 MTS/IEEE KONA (pp. 1-5). IEEE.
[32] Prechelt, L. (1998). Early stopping-but when?. In Neural Networks: Tricks of the trade (pp. 55-69). Springer, Berlin, Heidelberg.
[33] Rogne, R. H., Bryne, T. H., Fossen, T. I., & Johansen, T. A. (2020). On the usage of low-cost mems sensors, strapdown inertial navigation, and nonlinear estimation techniques in dynamic positioning. IEEE Journal of Oceanic Engineering, 46(1), 24-39.